Anisotropic magnetization and transport properties of $RAgSb_2$ (R = Y, La-Nd, Sm, Gd-Tm)

by

Kenneth Duane Myers

A dissertation submitted to the graduate faculty

in partial fulfillment of the requirements for the degree of

DOCTOR OF PHILOSOPHY

Major: Condensed Matter Physics

Major Professor: Paul C. Canfield

Iowa State University

Ames, Iowa

1999

Graduate College
Iowa State University

This is to certify that the Doctoral dissertation of

Kenneth Duane Myers

has met the dissertation requirements of Iowa State University

Committee Member

Committee Member

Committee Member

Committee Member

Major Professor

For the Major Program

For the Graduate College

INTRODUCTION

1.1. Introduction

Rich and complex behavior is observed in the magnetic and transport properties of the tetragonal $RAgSb_2$ (R= Y, La-Nd, Sm, Gd-Tm) series of compounds. The magnetization as functions of applied field and temperature is strongly anisotropic due to the crystalline electric field (CEF) splitting of the Hund's rule ground state multiplet. For most of the members of the series (R = Ce-Nd, Sm, Tb-Ho), the CEF anisotropy constrains the local magnetic moments to the basal plane. However, for R = Er, and Tm, the CEF splitting leads to moments aligned along the crystallographic c-axis.

All of the compounds, except for those containing Y, La, Ce, and Pr, order antiferromagnetically at temperatures ranging from approximately 1.8 K in $TmAgSb_2$ to 12.8 K in $GdAgSb_2$. $CeAgSb_2$, which manifests a temperature dependent resistivity typical of a Kondo lattice, is the only member of the series to exhibit ferromagnetic ordering with a Curie temperature of 9.6 K.

A particularly dramatic example of sharp metamagnetic transitions is observed in $DyAgSb_2$ at low temperatures. In this compound, the nature of the magnetic order changes abruptly with both the magnitude and the orientation of the applied field. The angular dependence of the transitions may be used to determine net distribution of the magnetic moments and to obtain an estimate of the coupling constants between the moments within the "4-position clock" model.

Resistivity measurements as a function of temperature are typical of other rare earth intermetallic compounds and manifest a loss of spin-disorder scattering below the magnetic transitions. However, the transverse magnetoresistance is abnormally large compared to other intermetallic compounds and possesses significant deviation from the predicted H^2 dependence on applied field. Furthermore, anomalous features in the magnetoresistance correspond to the field-induced magnetic transitions observed in the M(H) isotherms of many members of the series.

For R = Y, La, Pr, Nd, and Sm, de Haas-van Alphen and Shubnikov-de Haas oscillations are clearly observed at relatively low applied magnetic fields and exceptionally high temperatures. For example, de Haas van Alphen oscillations are readily apparent in the magnetization of $SmAgSb_2$ up to 25 K. Analysis of the observed frequencies of the quantum oscillations and their dependence on the direction of applied field, gives insight into the topology of the Fermi surface.

The outline of this work is as follows: This chapter will motivate the study of $RAgSb_2$ compounds and provide an overview of the crystal structure. Chapter 2 will discuss introduce crystal growth from high temperature solutions as it pertains to the synthesis of the rare earth silver antimonides and review measurement techniques. Chapter 3 will provide the foundation of the physics studied in rare earth intermetallic compounds, including magnetization and magnetic ordering, resistivity and magnetoresistance, and quantum oscillations. A thorough compound-by-compound analysis of the basic magnetization and transport properties of the $RAgSb_2$ series is presented in Chapter 4, along with a discussion of trends across the series. Details of the metamagnetic transitions and their angular dependence in $DyAgSb_2$ is the subject of Chapter 5. The electronic structure of the RAgSb2 is revealed in Chapter 6, via the analysis of de Haas-van Alphen and Shubnikov-de Haas oscillations. Finally, the results of this work and suggestions for future study will be the summarized in Chapter 7.

1.2. R-T-Sb compounds

1.2.1. Rare Earth Intermetallic Compounds

Generally, the investigation of rare earth intermetallic compounds is essential to the study of local moment magnetism in solids. Since the 4f-electrons are strongly localized, the rare earth elements, Y, La-Lu are chemically very similar. Therefore, whole series of compounds may often be synthesized with the same crystal structure, differing only in rare earth atom. This ability to vary the magnetic properties of the compound, through the choice of rare earth element, allows the systematic study of magnetic interactions between local moments and the effect of the surrounding crystalline environment on the magnetic properties. Furthermore, differences in the electronic structure as the rare earth element is varied may be revealed through the comparison of the magnetic and transport properties across the isostructural series.

Specifically, the study of the $RAgSb_2$ series of compounds arose as part of a two-fold investigation of new low carrier density compounds containing antimony and compounds with the rare earth elements in positions with tetragonal point symmetry.

1.2.2. R-T-Sb Compounds

The study of new Sb-containing compounds is important for several reasons. First, the R-T-Sb compounds are a new family, of which the physics has not been well explored. Previous measurements have primarily consisted only of crystallographic structural determinations (Ferguson, 1997). Magnetic and transport measurements have only been performed on a few members of this family and have concentrated on polycrystalline samples with R = Ce (Lakshmi, 1996; Skolozdra, 1994, Pierre, 1994; Flandorfer, 1996; Muro, 1997; Houshiar, 1995). However, measurements of the magnetic properties of compounds with rare earth elements other than Ce have been on polycrystalline samples for T = Mn, Co, Au, Zn and Cd (Wollesen, 1996), T=Pt, Au, and Pd (Kasaya, 1993), and T = Ni, Pd, Cu, and Au (Sologub, 1994).

Previous reports on the physical properties of the $RAgSb_2$ series of compounds have concentrated on measurements of polycrystalline samples. Primarily, these samples were prepared by arc melting a nearly stoichiometric composition of starting materials However, due to the polycrystalline nature of the samples, no investigation of the anisotropy in either the magnetic or transport properties was possible. These previous reports verified the crystal structure and provided a brief overview of the magnetic properties (Sologub, 1995). All of the compounds, except the non-magnetic rare earth elements La and Y, were shown to order antiferromagnetically at temperatures between 3.1 and 14 K. In addition, a ferromagnetic component to the magnetization was observed in $CeAgSb_2$. To date, no measurements of either the transport properties such as the temperature or field dependence of the resistivity or investigations of the Fermi surface such as de Haas van Alphen measurements have been performed.

In addition, the study of compounds with low carrier densities, such as many of the intermetallics containing Sb or Bi, is instrumental in understanding the electronic structure of materials. Due to the small number of carriers, slight changes in the Fermi surface arising from magnetic ordering, spin or charge density waves, or variation of the rare earth atom, may become very apparent. Furthermore, the Fermi surface of these materials is typically smaller than in other compounds, which allows probes of the electronic structure, such as magnetoresistance, and de Haas-van Alphen oscillations, to be used at relatively low applied magnetic fields.

A final reason for choosing to study compounds containing Sb pertains to the feasibility of synthesizing the new compounds. To successfully grow single-grain crystals of rare earth intermetallic compounds two criteria should be met. First, it is advantageous to have as few compounds as possible containing the same elements as the desired compound. This reduces the possibility of growing unwanted phases and removes restrictions on the starting compositions of the growth. Secondly, the melting points of the ternary melt should be low enough to be accessible to available furnace and crucible technology. Both of these points will be discussed in detail in chapter 2. The transition metal-antimony phase diagrams clearly meet both of these criteria and suggest that the growth of rare earth transition metal antimonides is practical.

1.2.3. The Advantage of Tetragonal Point Symmetry

The study of compounds with the rare earth in tetragonal symmetry is advantageous due to the complexity and richness of the magnetic structures and the simplified analysis compared to orthorhombic or monoclinic point symmetries. In systems with tetragonal symmetry, strong anisotropy arising from a tetragonal crystal electric field (CEF) splitting of the Hund's rule ground state multiplet may constrain the local moments to align either parallel or perpendicular to the c-axis. For example, the well-studied compounds with the $ThCr_2Si_2$ structure (Pinto, 1982), such as $TbNi_2Ge_2$, typically order with the moments along the c-axis, leading to Ising-like behavior (Islam, 1998). A spectacular example of the complexity arising from the long range interaction between local moments and CEF anisotropy is the series of at least nine field-induced transitions observed in $TbNi_2Si_2$

(Shigeoka, 1992; Fuji, 1990). It has been suggested that for a three dimensional Ising system, an infinity of stable magnetic phases may exist (Bak, 1982), the so called "devil's staircase". Although the existence of such a complex system has not been confirmed $TbNi_2Si_2$ remains a potential candidate.

On the other hand, the tetragonal CEF splitting of the Ho^{3+} ions in $HoNi_2B_2C$ constrains the magnetic moments to the one of four symmetric direction within the basal plane. In this case, careful study of the magnetization as a function both the magnitude and direction of the applied field provides valuable information about the nature of the magnetic order. In order to study this type of anisotropy, it is preferable that the easy orientation for the magnetic moments is within the basal plane for members of the series containing R = Tb, Dy, Ho, since these compounds typically have a higher magnetic ordering temperature than for R = Er, Tm, Yb due to their larger de Gennes factor. Overall, materials meeting these criteria are rare, with only a few examples previously studied.

1.2.4. Initial Investigation of Single Crystal R-T-Sb Compounds

An initial foray into the growth and characterization of R-T-Sb compounds consisted of attempts at synthesizing compounds with T = Cr, Fe, Ni, Cu, Rh, Pd, Ag, and Au. The results of these preliminary attempts were mixed. Large crystals with morphologies suggesting tetragonal crystal structures were produced for T = Ni, Cu, and Ag. Attempts to synthesize crystals with Au produced large, dendritic crystals which were revealed to be the cubic $R_3Sb_4Au_3$ compounds using single crystal x-ray diffraction. Attempts with the other transition metals produced a remarkable amount of crystals with a cubic morphology, consistent with the rock salt structure of RSb compounds, but no tetragonal compounds.

Although the size and morphology of the R-Cu-Sb crystals were excellent, significant growth-to-growth variation in the magnetic and transport properties was observed. Single crystal x-ray diffraction revealed the composition of the compounds to actually be RCu_xSb_2 with x varying between 0.78 and 0.92 (Myers, unpublished). This variation in composition and physical properties makes the compounds unsuitable for detailed analysis. Other R-T-Sb compounds exhibiting similar variations in composition occur with R = Ni, Mn, and Fe (Wollesen, 1996); consequently no further studies were made of these compounds.

Early attempts to synthesize R-Ag-Sb compounds were remarkably successful. These first samples were plate-like crystals with well-formed facets which suggest a tetragonal crystal structure, sufficiently large, and of excellent quality with residual resistivity ratios near 100 for the light rare earths and near 30 for the heavy rare earths. Single crystal x-ray diffraction confirmed the composition of the samples to be tetragonal $RAgSb_2$ and revealed no site deficiencies. Furthermore, the crystal structure of $RAgSb_2$ is very similar to the orthorhombic RSb_2 series of compounds, which exhibits strong anisotropies, complex metamagnetism, and large near-linear magnetoresistance (Bud'ko, 1998). With these promising initial results, the synthesis of single crystals was expanded to include most of the $RAgSb_2$ series. Although compounds could not be grown with R= Eu, Yb, or Lu, the growth of the rest of the $RAgSb_2$ series with R=Y, La-Nd, Sm, Gd-Tm was successful.

1.3. Crystal Structure of $RAgSb_2$

1.3.1. Crystal Structure

The rare earth silver antimonides crystallize in a simple tetragonal structure (P4/nmm, #129) with two formula units per cell and the rare earth ions in a position with tetragonal point symmetry (4mm). The atomic positions are given in Table 1.1. As seen in Fig. 1.1, this structure consists of Sb – RSb – Ag – RSb – Sb layers. The lattice constants, presented in Table 1.2, reflect the lanthanide contraction and range from a = 4.253 Å and c = 10.39 Å in $TmAgSb_2$ to a= 4.390 Å and c = 10.84 Å in $LaAgSb_2$. Throughout the series, the c/a ratio is nearly a constant 2.44.

1.3.2. Comparison with RSb_2

The crystal structure of $RAgSb_2$ is very similar to the RSb_2 compounds, making it a logical candidate for further study. In contrast to the weakly orthorhombic structure of the rare earth diantimonides (Wang, 1967; Hulliger, 1979) ($a \approx 6.17$Å, $b \approx 6.05$ Å, $c \approx 17.89$ Å), the rare earth silver antimonides are tetragonal with the rare earth element in a site with

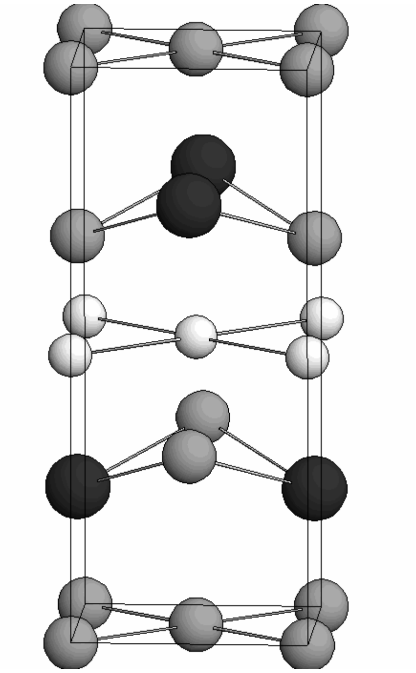

Fig. 1.1 The crystal structure of $RAgSb_2$. Dark circles indicate R, medium circles are Sb and light circles are Ag.

Table 1.1 Atomic positions of $RAgSb_2$ (Sologub, 1995)

Atom	P4/nmm	x	y	z
R	2c	¼	¼	0.2382
Ag	2b	¾	¼	½
Sb1	2a	¾	¼	0
Sb2	2c	¼	¼	0.6737

Table 1.2 Lattice parameters and cell volumes of the $RAgSb_2$ series of compounds. Note the contraction in parameters as the rare earth atoms become heavier and smaller. (Sologub, 1995)

Compound	a (Å)	c (Å)	c/a	V (Å^3)
$YAgSb_2$	4.276	10.48	2.452	191.8
$LaAgSb_2$	4.390	10.84	2.469	208.9
$CeAgSb_2$	4.364	10.69	2.452	203.7
$PrAgSb_2$	4.349	10.67	2.453	201.9
$NdAgSb_2$	4.335	10.63	2.452	199.8
$SmAgSb_2$	4.312	10.55	2.448	196.2
$GdAgSb_2$	4.295	10.50	2.446	193.8
$TbAgSb_2$	4.283	10.47	2.446	192.2
$DyAgSb_2$	4.274	10.44	2.443	190.8
$HoAgSb_2$	4.266	10.42	2.443	189.7
$ErAgSb_2$	4.257	10.39	2.441	188.3
$TmAgSb_2$	4.253	10.39	2.443	188.0

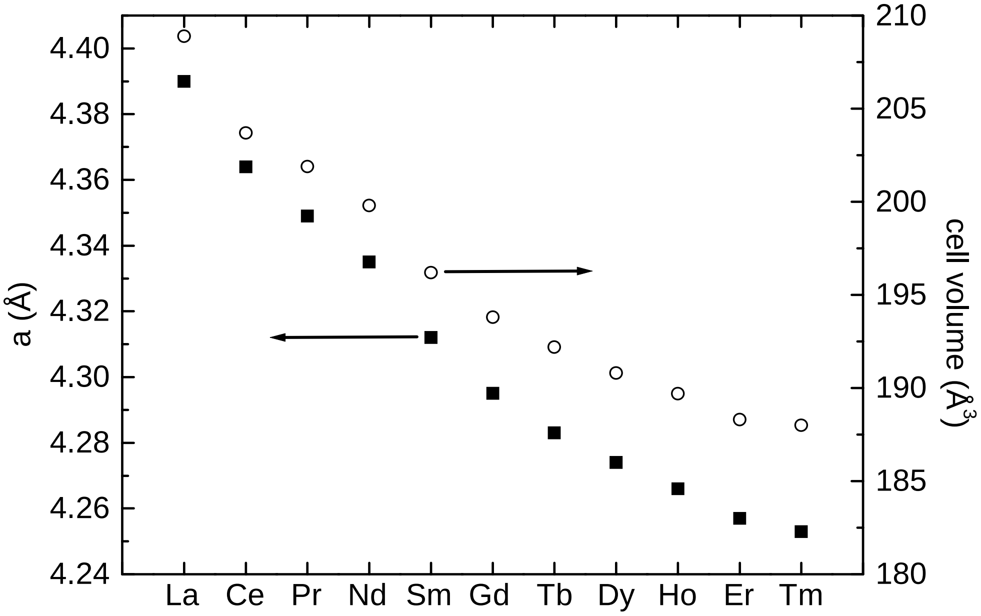

Fig 1.2 Lattice parameter (■, left axis) and cell volume (○, right axis) of $RAgSb_2$ as a function of rare earth element.

tetragonal point symmetry (Brylak, 1995; Flandorfer, 1996; Muro, 1997), simplifying a characterization of the magnetic and transport properties. Figure 1.3 shows that the $RAgSb_2$ structure may be obtained from the RSb_2 structure by equalizing the a and b axes, inserting two planes of Ag atoms, and horizontally shifting the central Sb plane of the RSb_2 structure.

In addition to the microscopic difference in the crystal structure, there is a related macroscopic difference between the $RAgSb_2$ and RSb_2 crystals. Whereas the RSb_2 crystals are malleable and composed of metallic sheets that can be peeled apart in a micatious fashion, the $RAgSb_2$ crystals are more three-dimensional in their mechanical properties, less malleable, and can be ground into a powder. Most likely, these mechanical differences are the result of the additional silver atoms increasing the bonding along the c-axis.

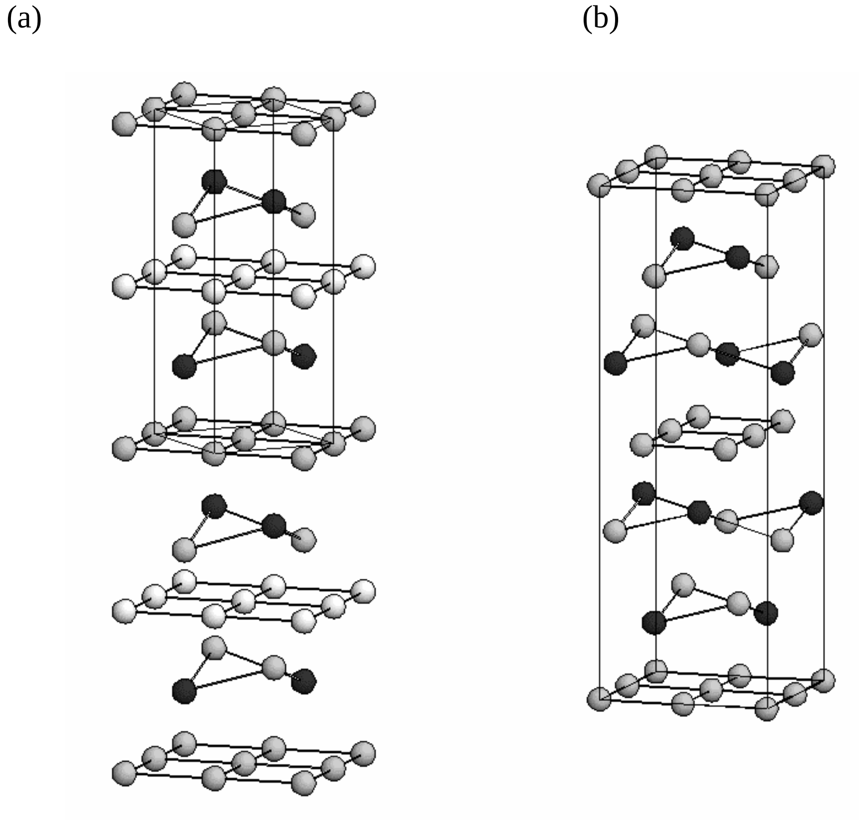

Fig. 1.3 Crystal Structure of (a) $RAgSb_2$ and (b) RSb_2. Note that the lines are guides to the eye and do not represent actual chemical bonds.

2. CRYSTAL GROWTH OF RARE-EARTH INTERMETALLIC COMPOUNDS AND EXPERIMENTAL METHODS

2.1. Introduction

Although polycrystalline samples may be used for preliminary measurements of the magnetic and transport properties of new materials, high-purity single crystals are essential for any detailed analysis. For example, compounds with rare earths in non-cubic point symmetry, such as the layered $ThCr_2Si_2$ structure, frequently possess strong anisotropies in the magnetic properties and electronic structure. In a polycrystalline material, the random orientation of the microscopic grains can average out any anisotropies in these properties. In addition, many measurements require large samples with long-range order, such as neutron or X-ray diffraction.

The quality of single crystals is generally superior to polycrystalline samples, since single crystals do not possess grain boundaries. Impurities, which are often present between the grains of polycrystalline materials, are substantially reduced, due the much smaller surface area to volume ratio of single grain crystals. Considerable stress and strain may also be present in polycrystalline samples, due to rapid cooling and crystallites growing against each other. Generally, lower impurity and defect concentrations lead to higher quality samples as manifest, for example, in higher residual resistivity ratios. The significantly lower impurity concentrations are essential to the observation of many phenomena, such a quantum oscillations, that depend strongly on the mean free path of the conduction electrons.

There are many techniques for the growth of single crystals. One of the most versatile methods is growth from high-temperature solutions, also know as flux growth. This introduction of crystal growth from high-temperature solutions will begin with the analysis of a binary phase diagram, which will be used to synthesize crystals from a binary melt. The discussion will proceed to the growth of binary compounds from third element fluxes and then to the synthesis of ternary compounds from a ternary melt. Finally, specific experimental techniques used in crystal growth from high-temperature solutions will discussed.

The final part of this chapter will focus on the experimental techniques and apparatus used for the measurement of the thermodynamic and transport properties of rare earth intermetallic compounds. This section will include details of the preparation of samples for measurements of the magnetization, specific heat, resistivity, and magnetoresistance.

2.2. Crystal Growth From High Temperature Solutions

2.2.1. Binary Phase Diagrams

The natural starting point for any discussion of crystal growth is to analyze a binary phase diagram. Figure 2.1 shows such a phase diagram for Nd and Sb. The left and right sides of the phase diagram correspond to pure Nd and Sb, respectively. The curved line separating the all-liquid region (L) from the regions containing liquid and solid (L+S) is the *liquidus* line. At low temperatures, there are four thermodynamically stable binary compounds, represented as vertical lines: Nd_5Sb_3, Nd_4Sb_3, NdSb, and $NdSb_2$. Except for NdSb, all of these compounds decompose before they melt. For example, $NdSb_2$ is stable up to 1650 ºC. At this temperature, called the peritectic, $NdSb_2$ decomposes into NdSb and liquid, as shown by the horizontal line. Compounds that decompose before they melt (the line denoting the compound does not meet the liquidus) are known as incongruently

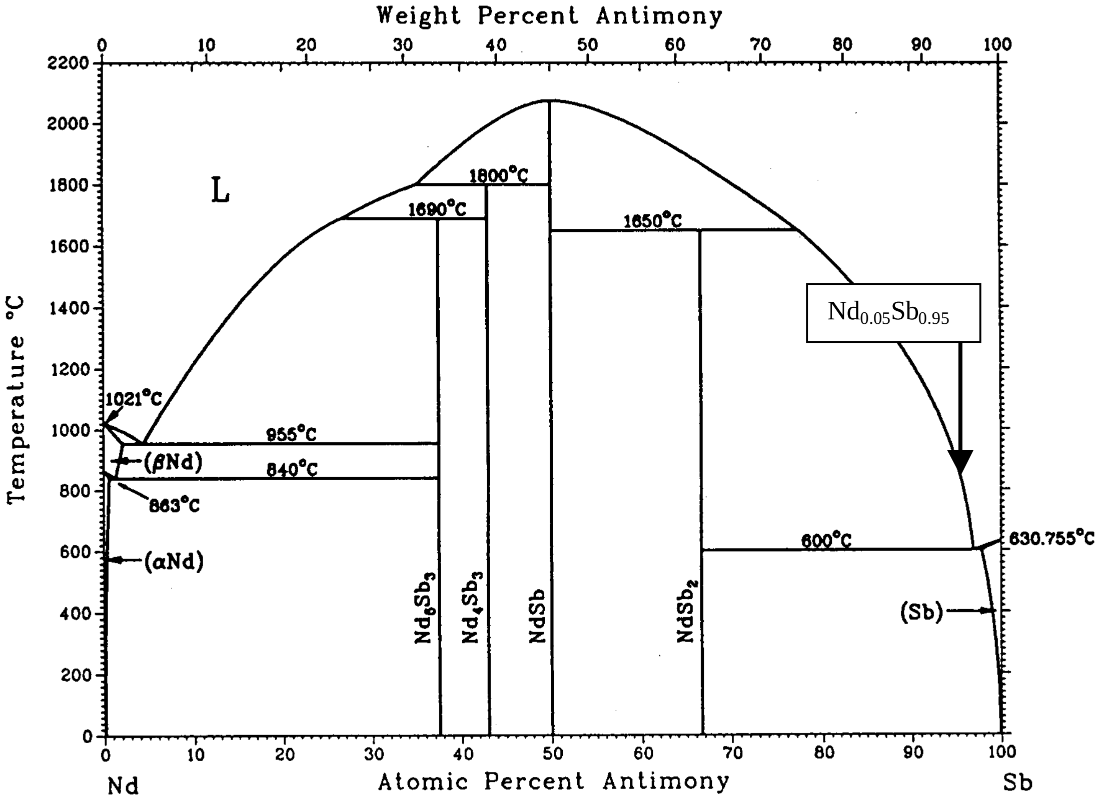

Fig 2.1 Binary phase diagram for Nd and Sb (after Massalski, 1992).

melting compounds. On the other hand, NdSb, which persists up to the liquidus, is an example of a congruently melting compound.

There is a vast assortment of techniques to synthesize single crystals and the utility of each varies widely. Thorough reviews of many of these methods may be found in Pamplin (1975) and the references therein. Examples of crystal growth methods include the Czochralski and zone refining methods which are essential to the semiconductor industry, since these methods can produce large, very high purity silicon, germanium and gallium arsenide single crystals.

Unfortunately, most of these methods require the composition of the melt to be equal to the desired product, constraining these methods to the synthesis of only congruently melting compounds. Furthermore, the starting components must be heated above the melting temperature of the target compound, which may easily be above the working range of available furnaces and crucibles. For example, consider the Nd-Sb phase diagram (Fig. 2.1). NdSb is the only compound which is congruent and may be grown using these methods. Since the melting temperature of NdSb is over 2000ºC, quartz and standard furnaces using SiC elements, may not be used. Finally, the vapor pressures of the constituent elements may become appreciable at these very high temperatures. For instance, the vapor pressures of some of the rare earth elements, such as samarium, europium and ytterbium, become large at temperatures above 900ºC, leading to chemical reactions with the crucibles as well as a loss of stoichometry.

2.2.2. Growth of Binary Compounds from a Self Flux

Many of the above problems may be avoided by growing the crystals out of a high temperature solution. An extensive overview of many of the methods of crystal growth from high-temperature solutions may be found in Elwell and Scheel (1975). The solvent in this high-temperature solution is frequently called a flux, since it produces lower melting temperatures than those of the starting components, much like the materials used for soldering and welding. At high temperatures, all of the constituent elements are dissolved in the flux. As the temperature of the melt decreases, the solubility of the target compound decreases, forcing the desired compound to precipitate out of the solution.

For a detailed example of the crystal growth of a specific rare earth intermetallic compound, it is useful to consider the growth of $NdSb_2$. From the aforementioned Nd-Sb binary phase diagram (Fig. 2.1), several relevant facts are apparent:

- $NdSb_2$ is in equilibrium with the melt for Sb-rich initial concentrations and temperatures below 1650ºC, above which the compound decomposes into NdSb and liquid.
- Up to 10 atomic percent Nd can be completely dissolved in Sb at 1200ºC, which is the maximum temperature quartz may be used to provide an inert atmosphere.
- The cooling of an Sb rich melt will result in the formation of either NdSb or $NdSb_2$, depending on the initial concentrations.
- The growth should end above 600ºC to prevent the solidification of the eutectic concentration of $Sb_{0.97}Ag_{0.3}$.

These points suggest that the ideal flux for the growth of $NdSb_2$ is excess Sb. In this case, the Sb (known as a "self flux") depresses the required temperature range of the growth. Although $NdSb_2$ may be grown from a starting concentration of $Nd_{0.1}Sb_{0.9}$, an even more dilute initial concentration is sometimes more desirable to control nucleation and allow enough physical space for free growth of individual crystals. Frequently a concentration that is too rich will yield small, poorly formed, intergrown crystals. Empirically, an initial concentration of $Nd_{0.05}Sb_{0.95}$ (represented by the arrow in Fig 2.1) was found to be ideal. The starting elements are heated to 1100ºC to allow the elements to melt and mix together. As this melt is slowly cooled, it will meet the liquidus-solidus line at about 840ºC. Further cooling decreases the solubility of $NdSb_2$ which will cause crystals of $NdSb_2$ to form. Since the Sb-rich eutectec temperature is 600ºC, it is desirable to end the growth process well above this temperature at 675ºC. At this temperature, the excess flux is decanted, revealing plate-like crystals of $NdSb_2$ (Canfield, 1992) (Bud'ko, 1998).

2.2.3. Third Element Fluxes

In principle, the above method may also be used to synthesize single crystals of NdSb. However, inspection of the Nd-Sb phase diagram (Fig. 2.1) reveals that if the melt is allowed to cool below 1650ºC, crystals of $NdSb_2$ will form instead of NdSb. Similarly, on the Nd-rich side of the phase diagram, Nd_4Sb_3 will be grown below 1800ºC. Since these temperatures are above the useful range of quartz and SiC furnaces, it is necessary to grow NdSb crystals using an alternate method. The temperatures required for the growth may be dramatically decreased by using a third element as a flux.

At this point, it is instructive to refer to two simple and more familiar examples of flux growth: rock salt and epsom salt crystals grown in water. Although the melting temperature of NaCl is 800ºC, well faceted cubic crystals can easily be grown in a household kitchen. NaCl is dissolved in hot water to the point of saturation. The water is then slowly allowed to evaporate from the container, which decreases the total amount of NaCl dissolved. This forces the NaCl out of solution through the formation of crystals. Another example of flux growth that may be performed near room temperature is the growth of Epsom salts ($MgSO_4$) from water (Fisher, 1998). Like the aforementioned example with NaCl, the Epsom salts are dissolved in hot water to form a saturated solution. In this case however, the solubility of $MgSO_4$ is very sensitive to the temperature of the water. Since $MgSO_4$ is less soluble at lower temperatures, crystals may be formed by allowing the solution to gradually cool. This is the technique used most often to grow crystals from third element fluxes.

Due to their relatively low melting points, some of the most common metallic flux elements are Al, Bi, Ga, In, Pb, Sb, and Sn, with the merits of each described in detail in Canfield and Fisk (1992). The choice of the appropriate third-element flux is critical to the successful growth of crystals, and several criteria must be addressed:

- The melting temperature of the flux must be low enough to allow a sufficient temperature range for the formation of the desired crystals.
- All of the solute materials must be soluble in the flux for the given temperature and concentrations.
- Ideally, there should be no nearby compounds containing the flux elements and any of the solute elements, which would introduce second phases and impurities.
- The flux elements should not substitute into any of the atomic sites of the target material.
- The flux should not be reactive with either the crucible or the quartz tubing.
- Finally, certain elements are undesirable due to their high toxicity, such as mercury or cadmium.

In the example case of NdSb, crystals were successfully grown using a Sn flux. Specifically, the compound can be formed from an initial concentration of 5 at. % NdSb in 95 at. % Sn which is cooled from 1150ºC to 750ºC.

2.2.4. Ternary Compounds From A Self Flux

The growth of ternary compounds is similar to the growth of binary compounds. As before, an adequate flux must be found and the initial melt composition must be chosen to avoid the formation of other phases. For the growth of the $RAgSb_2$ series of compounds, Sb is also the ideal flux, since this “self flux” melts at a relatively low temperature (630ºC), does not add any additional elements into the melt, and does not react with alumina or quartz.

However, the greatest problem with growing rare earth intermetallic crystals out of antimony is the stability of many of the R-Sb binary compounds, particularly RSb and RSb_2.

For ternary or quaternary compounds, it is difficult to predict beforehand the optimum concentrations and temperature profiles for a proposed growth. Although these factors may be determined from the appropriate ternary phase diagram, these diagrams exist only for very few systems. Therefore, the first growth attempt is typically based on an analysis of the binary phase diagrams of the constituent elements, with the concentrations and temperatures chosen to avoid unwanted phases. These initial attempts may also consist of three or more slightly different starting concentrations. From qualitative (crystal size, morphology, amount of flux on surface, facets) and quantitative (resistivity, magnetization, powder X-ray diffraction) analysis of the sample, the temperature profiles and initial concentrations may be optimized.

An initial estimate of the required concentrations of the three elements in the melt and temperature profile may be determined from the three binary phase diagrams (Figs 2.1 and 2.2):

- Ag-Sb: As long as the melt is Sb rich, no Ag-Sb binaries will be produced. If the rare earth concentration is small enough, its effects may be ignored, and the minimum ending temperature of the growth will range from 485 ºC to 630ºC, depending on Sb content.
- Ag-Nd: Since the flux is Sb, this phase diagram will have little impact in deciding the initial concentrations if any ternary compounds exist. However, it should be noted that if a Nd-rich, Ag bearing compound were desired, then the $Nd_{.8}Ag_{.2}$ eutectic with

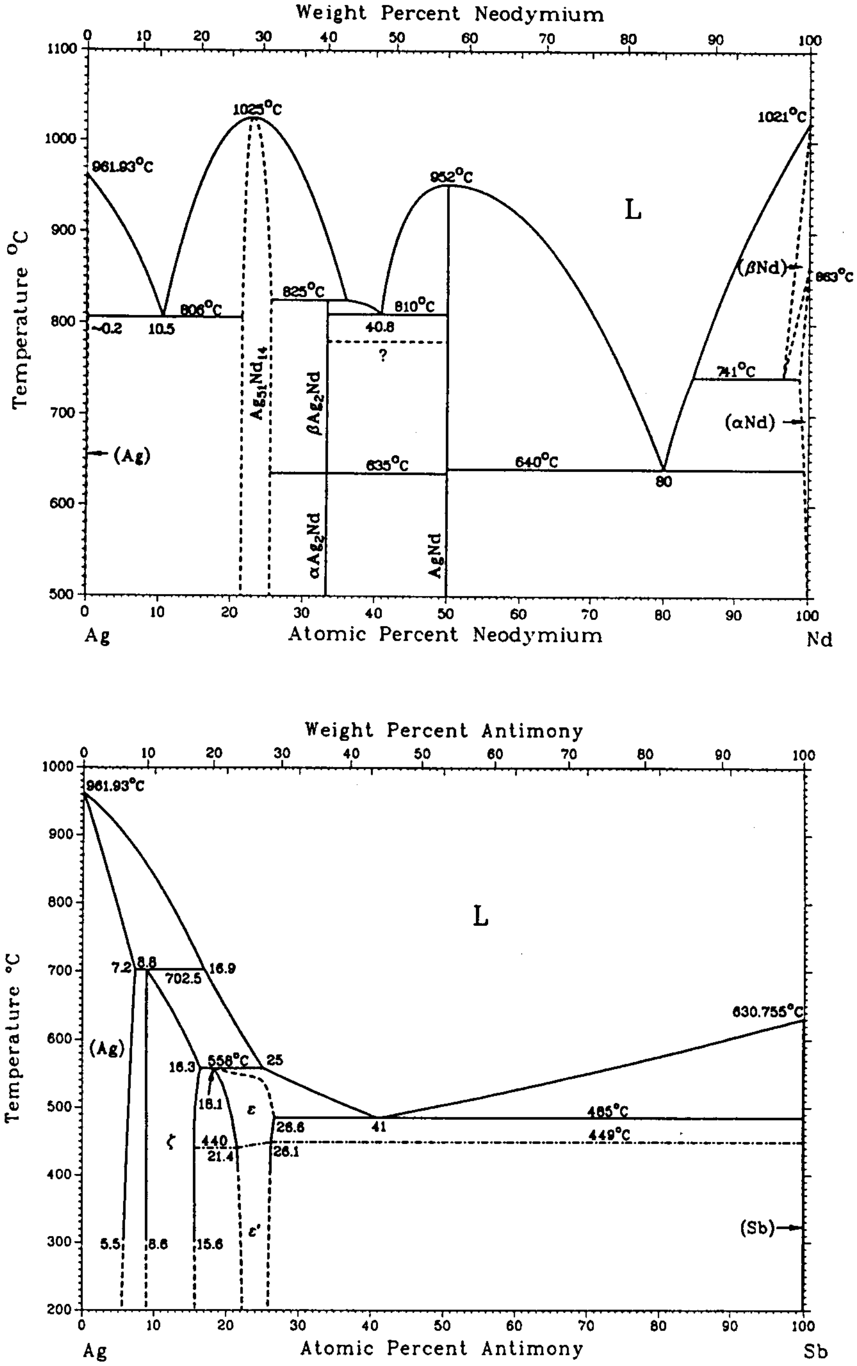

Fig. 2.2 Binary phase diagrams for (a) Nd-Ag, and (b) Ag-Sb. Note the low melting points and lack of binary compounds on the Sb-rich side of the the Ag-Sb diagram (after Massalski, 1992).

T_{Eu} ≈640ºC would be promising.

- Nd-Sb: There are four compounds in the Nd-Sb binary system. Of these, only two compounds are accessible for Sb rich starting concentrations, NdSb and $NdSb_2$. The former affects the starting concentrations little, since the liquidus-solidus surface is only exposed above 1650ºC. The latter, however is more troublesome. In order to preclude formation of $NdSb_2$ below 1200ºC, the concentration of Nd cannot exceed 10% relative to Sb. To allow sufficient temperature range for the growth of $NdAgSb_2$, a starting Nd concentration 5% relative to Sb will allow cooling down to about 900ºC (Fig. 2.3 (a), avoiding the formation of $NdSb_2$.

A ternary phase diagram (Fig. 2.3) shows a summary of the binary and ternary phases. RAgSb is the only ternary phase present besides the target compound. The relative emptiness of this phase diagram is clearly beneficial to the growth of the $RAgSb_2$ compounds, since there are fewer second phases to avoid. As mentioned previously, this dearth of R-T-Sb compounds was part of the motivation of this study.

2.2.5. Experimental Technique for Flux Growth

For standard growths, the starting materials were placed inside a 2 ml or 5 ml alumina crucible, called the "growth crucible" [Fig. 2.3 (b)]. Typically, the element with the lowest melting point (in this case Sb) is placed on the top of the other elements to help dissolve the other materials. Another crucible, called the "catch crucible," is filled two-thirds full of quartz wool and placed inverted on top of the growth crucible. To protect the growth from

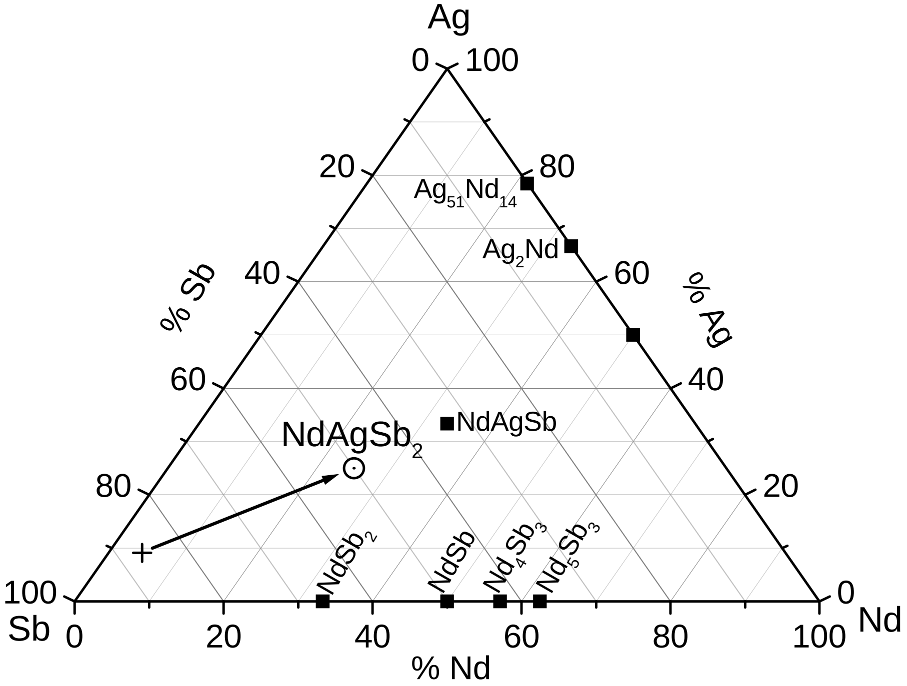

Fig. 2.3 Ternary phase diagram of the Nd-Ag-Sb system. The + indicates the initial melt composition for the growth of most of the $RAgSb_2$ compounds from a self flux.

oxidization, a protective atmosphere must be provided. For crystal growths in box furnaces, the simplest means of doing this is to seal the growth in quartz tubing under a partial pressure of argon. However, this limits the maximum temperature of the growth to around 1200ºC, the softening point of quartz.

Once the sample has slowly cooled to the desired temperature [Fig 2.3 (a)], the remaining flux must be decanted from the crucible. This is done effectively by removing the ampoule from the furnace and inserting it inverted into a centrifuge. During the spin, the quartz wool in the catch crucible acts as a strainer which allows the excess flux to flow to the bottom of the catch crucible and holds any crystals that may have detached from the growth crucible.

Overall, the sample yield using this growth technique is impressive. Large single grain crystals of $RAgSb_2$ were grown for almost the whole series of rare earth elements. The largest samples produced were of $LaAgSb_2$, with dimensions near 1 × 1 × 0.5 cm. In the $RAgSb_2$ series, the sample yield diminishes as the rare earth elements become heavier and smaller. To account for this, the initial concentration was adjusted to $R_{0.05}(Ag_{0.3}Sb_{0.7})_{0.95}$ for R = Er and Tm. Even with this change, the best samples of $TmAgSb_2$ were thin square plates approximately 1mm wide.

The quality of the samples also decreases along with the size, as evidenced by a decrease in residual resistivity ratio. This is discussed in detail in Chapter 4. Despite

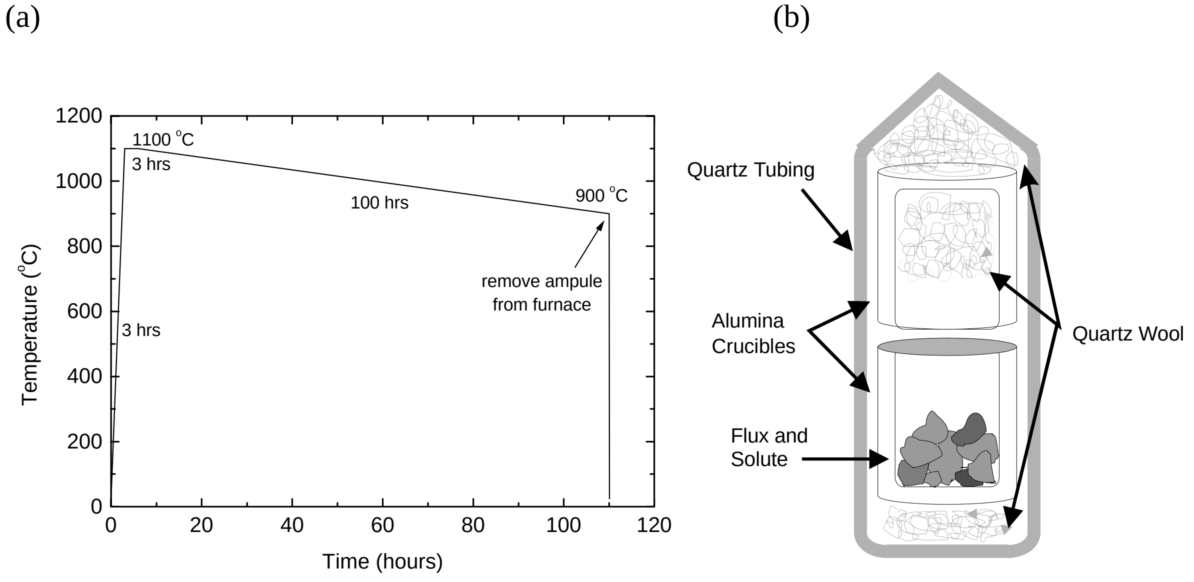

Fig 2.3 (a) Temperature profile for the growth of single crystals of $RAgSb_2$ from an Sb-rich flux. At about 110 hours, the ampoule is removed from the furnace and the remaining flux is decanted from the desired crystals. (b) diagram of the ampoule used for crystal growth (see text).

multiple attempts with varying temperatures and concentrations, no members of the $RAgSb_2$ series of compounds were grown with R = Eu, Yb, and Lu. For the R = Lu, this could be the result of the rare earth atoms becoming too small for optimal bonding (Brylak, 1995), whereas for R= Eu and Yb, valency may play a role. Finally, the vapor pressures of Eu and Yb become appreciable within the temperature range used for growth leading to a loss of stochiometry as the Eu or Yb evaporates from the melt.

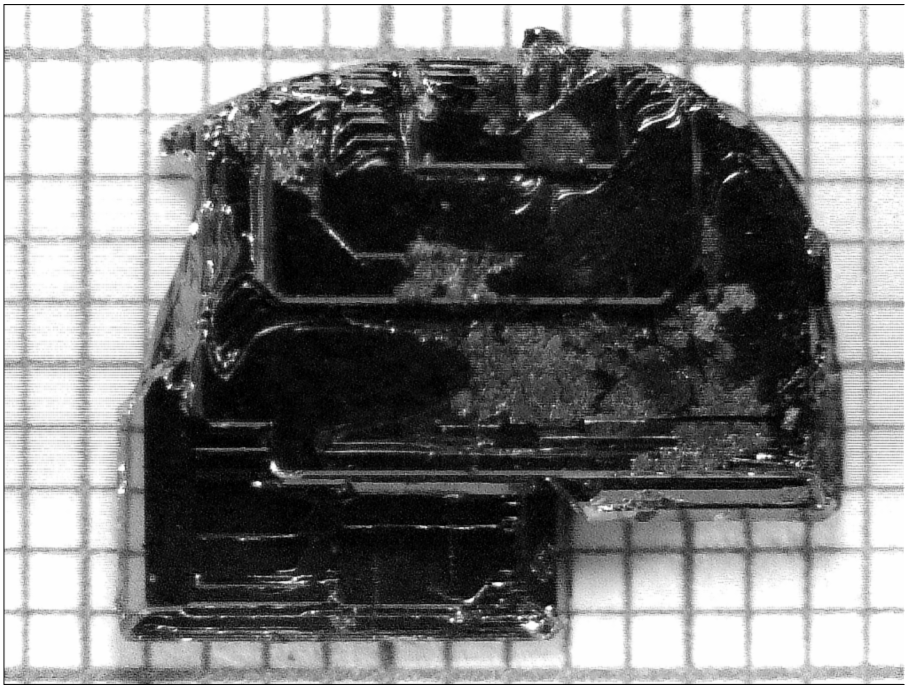

Fig. 2.3 Single crystal of $LaAgSb_2$ shown over a 1 mm scale. The c-axis is perpendicular to the plane of the paper.

2.3. X-ray Diffraction

2.3.1. Powder X-ray Diffraction

X-ray diffraction patterns were taken at room temperature on pulverized single crystals to detect the presence of any impurity phases in the samples and confirm the unit cell dimensions. A conventional tube source was used to obtain the patterns in flat plate geometry using CuKα (1.5406 Å) radiation. These patterns are consistent with the simple tetragonal $ZrCuSi_2$ structure (P4/nmm, #129) and previous measurements of polycrystalline samples (Brylak, 1995)(Flandorfer, 1996)(Muro, 1997). A typical pattern is shown in Fig. 2.4 of $LaAgSb_2$. All of the peaks may be indexed to a tetragonal lattice with a = 4.39Å and c = 10.82 Å, except for weak peaks at 40.1° and 86.6°, which correspond to a small amount of residual Sb (Swanson, 1954) flux on the surface.

2.3.2. Single Crystal X-ray Diffraction

In order to check for any partial occupancies in the $RAgSb_2$ series, which occur in the related $RTSb_2$ phases with T = Mn, Fe, Co, Ni, Cu, Zn, and Cd (Sologub, 1994; Wollesen, 1996; Leithe-Jasper, 1994; Albering, 1996; Cordier, 1985), a single crystal structure determination was performed on $GdAgSb_2$ using a Rigaku AFC6R diffractometer with graphite monochromated Mo Kα ($\lambda = 0.71069$ Å) radiation and a 12 kW rotating anode generator. The data were collected at room temperature using the ω-2θ scan technique to a maximum 2θ value of 60.2°. The lattice parameters of $GdAgSb_2$ were determined to be a = 4.292(2) Å and c = 10.494(4) Å, V = 193.3(2) $Å^3$, space group P4/nmm (No. 129). Table 1 lists the atomic positions and occupancy factors for $GdAgSb_2$. In contrast to the other previously mentioned $RTSb_2$ series, no partial occupancies were observed in the structure of

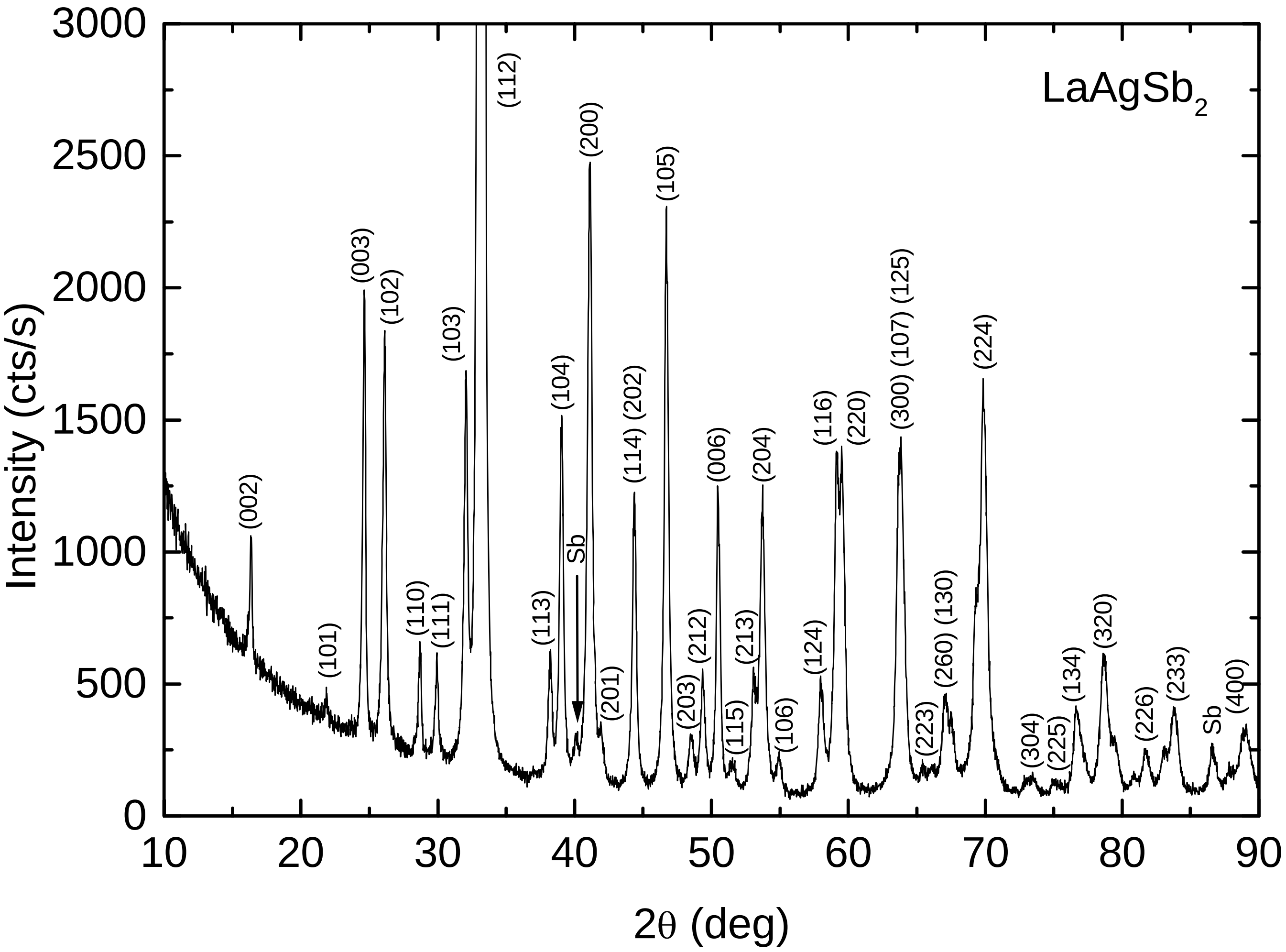

Fig. 2.4 Powder X-ray diffraction pattern for $LaAgSb_2$. Peaks are indexed to a tetragonal structure with a=4.39 Å and c=10.82 Å. Note: peaks near 40.1 º and 86.6º correspond to residual Sb.

Table 2.1. Positional parameters and occupancy of $GdAgSb_2$

Atom	x	y	z	occupancy
Sb(1)	¼	¼	0.6811(1)	1.00
Sb(2)	¾	¼	0	1.00
Gd	¾	¾	0.7641(1)	1.00
Ag	¾	¼	½	1.00

$GdAgSb_2$. It is concluded, that no site deficiencies are present in the $RAgSb_2$ series. As shown below, this is consistent with low residual resistivity values found for the $RAgSb_2$ compounds.

2.4. Measurement methods

2.4.1. Magnetization Measurements

The magnetic measurements of the materials were acquired in a Quantum Design Magnetic Property Measurement System (MPMS) Superconducting Quantum Interference Device (SQUID) magnetometer for temperatures between 1.8 and 350 K and applied fields up to 55 kOe. Samples were chosen based on their size and lack of residual flux. A typical sample mass was 10 mg for the magnetic compounds and up to 100 mg for the nonmagnetic compounds. These samples were generally mounted in clear plastic drinking straws with a plastic disk for support. These plastic disks were measured separately to allow a subtraction of their contribution to the total magnetization. However, the larger, non-magnetic samples were frequently mounted between two straws to minimize the background signal. Typically, the samples were aligned in the straw by hand, although for the detailed measurements of the angular dependence a specially modified Quantum Design sample rotor with an angular resolution of 0.1 ° was used.

Magnetic measurements were also performed in a Quantum Design Physical Property Measurement System (PPMS) with the torque magnetometer option in applied fields up to 90 kOe and temperatures between 1.8 and 300 K. The samples were mounted on specially constructed microfabricated silicon torque lever chips. Embedded on each chip are two piezoresistor grids. These grids change their resistance in response to mechanical stress. A resistance bridge senses the resistance change of the grids, and hence the torque on the sample chip.

2.4.2. Resistivity Measurements

Resistivity measurements were performed with the standard four-probe technique within the temperature and magnetic field environment of the Quantum Design MPMS. The samples were formed into a matchstick geometry with a wire saw using a 0.005 inch diameter wire with 600 grit silicon carbide powder suspended in a glycerol and water solution. In some cases, the samples were also polished using a Buehler Minimet polisher with a fine polishing pad and powdered alumina in water. Platinum wires with a 0.025 mm diameter were contacted to the sample with Epotek H20E silver epoxy. After curing the contacts for 30 minutes at 200 ºC, typical contact resistances were between 1 and 2 Ω. A typical resistivity bar with dimensions of 0.6 mm×0.4 mm×4 mm is shown in Figure 2.5. The distance between the voltage contacts is approximately 3.1 mm. Uncertainty in the measurement of the cross sectional area and distance between voltage contacts is the dominant source of uncertainty in the resistivity measurements, limiting the precision of the resistivity to about 10%. The resistance of the samples was measured with a Linear Research Inc. LR-400 AC bridge operating at a frequency of 15.9 Hz. The excitation current was either 3 mA or 0.3 mA, depending on the resistance of the sample. Typical current densities

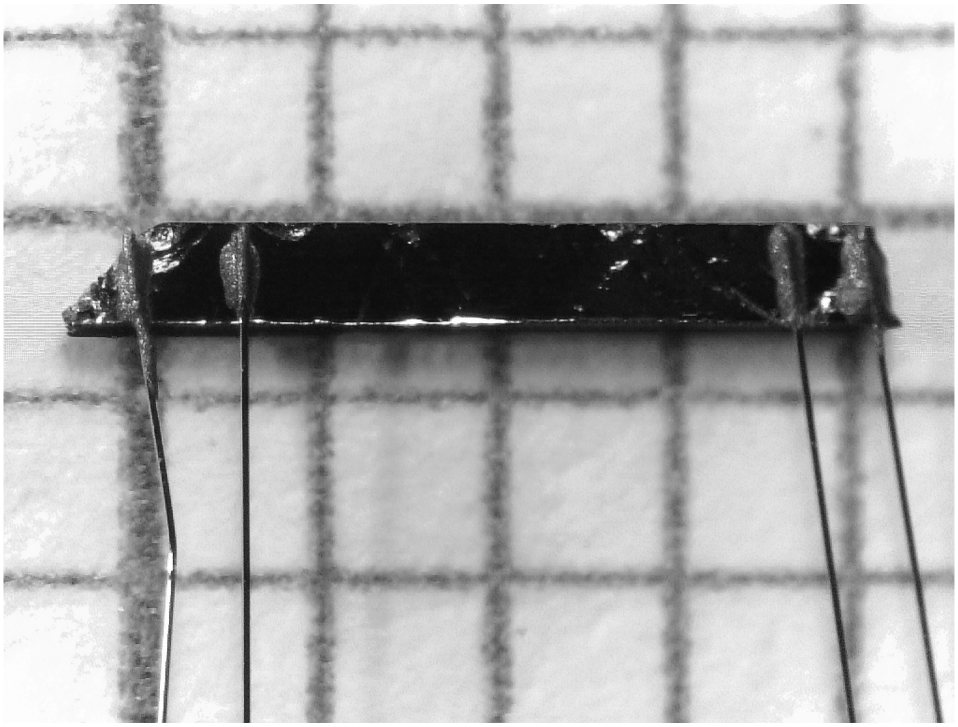

Fig. 2.5 Crystal of $LaAgSb_2$ prepared for resistivity measurements with platinum wires secured with silver epoxy, shown on a mm scale. The c-axis is out of the page.

ranged from 0.05 Acm^{-2} to 1 Acm^{-2}. The data were then acquired and saved via External Device Control (EDC), an extension to the MPMS operating system.

2.4.3. Specific Heat

Specific heat measurements were made using the heat capacity option of the Quantum Design PPMS. This instrument uses a relaxation technique, in which the sample is briefly heated and then allowed to cool. The thermal response of the sample is then fit over the entire temperature response using a model that accounts for the thermal relaxation of both the sample and the sample platform. The samples were attached to the heat capacity platform with either Apezion H or N grease. The thermal response of the platform and grease was measured separately to allow for the subtraction of this component from the final measurement. To achieve maximum accuracy within reasonable time constraints, the system was typically allowed to cool for two time constants. Thermal contact with the environment was minimized by evacuating the sample chamber to approximately 0.01 mTorr. For these measurements, samples were chosen on the merits of size, thinness, and flatness of one face. The flatness is important to insure good thermal contact between the sample holder and the sample.

THE PHYSICS OF RARE EARTH INTERMETALLIC COMPOUNDS

2.5. Introduction

Measurements of thermodynamic and transport properties are essential to understand the diverse physical properties of the rare earth intermetallic compounds. Detailed studies of the magnetization, as functions of applied magnetic field and temperature, elucidate the nature of the interactions between the magnetic moments as well as between the local moments and surrounding atoms. Resistivity measurements may be used to determine sample quality, analyze scattering mechanisms, and study the Kondo effect. Magnetoresistance and quantum oscillations, such as the de Haas-van Alphen effect, reveal details of electronic structure and the topology of the Fermi surface. Specific heat measurements, and subsequent determinations of the change in entropy, give insight into phase transitions, the crystalline electric field, and details of the electrons and phonons. For any new material, these are the baseline measurements needed to evaluate the physics of the low-temperature ground state.

This chapter will serve as an introduction to some of the physics of rare earth intermetallic compounds. First, an overview of the magnetic properties of rare earth intermetallic compounds will be presented. This discussion will start with the properties of non-interacting local moments and proceed to interactions between the moments. A discussion on the anisotropy of the magnetic properties arising from crystal electric fields will follow. After an overview of the zero-field resistivity, magnetoresistance will be introduced. Finally, the origin of quantum oscillations, such as the de Haas-van Alphen and

Shubnikov-de Haas effects and their usefulness in determining the topology of the Fermi surface, will be presented.

2.6. Magnetism

2.6.1. 4f Electrons and Local Moment Magnetism

The natural place to begin any discussion of the magnetic or transport properties of rare earth intermetallic compounds is the electronic configuration of the rare earth ions. Almost all of the rare earth ions are trivalent and of comparable size, causing their chemical properties to be closely similar. Therefore, a series of compounds can often be synthesized which differ only in the choice of lanthanide element. This valuable ability allows a systematic study of the physics of rare earth intermetallic compounds. By studying a whole series of compounds, the effects of the crystal electric field, interactions between ions, and other physical characteristics may be separated from each other. Finally, the analysis of trends across the series aids in the understanding of the physics of the individual members.

Figure 3.1 shows the radial densities of the electrons of Gd^{3+}. As seen in the figure, the 4f electrons are much more strongly localized than the 5s, 5p, and 6s electrons. Furthermore, these 4f electrons are shielded by the completely filled $5s^2$ and $5p^6$ shells. Therefore, the 4f electrons may be considered part of the electronic core, not directly interacting with the rest of the electronic system. Since a partially filled 4f shell will have a large magnetic moment, it is imperative to determine the electronic configuration of the 4f electrons.

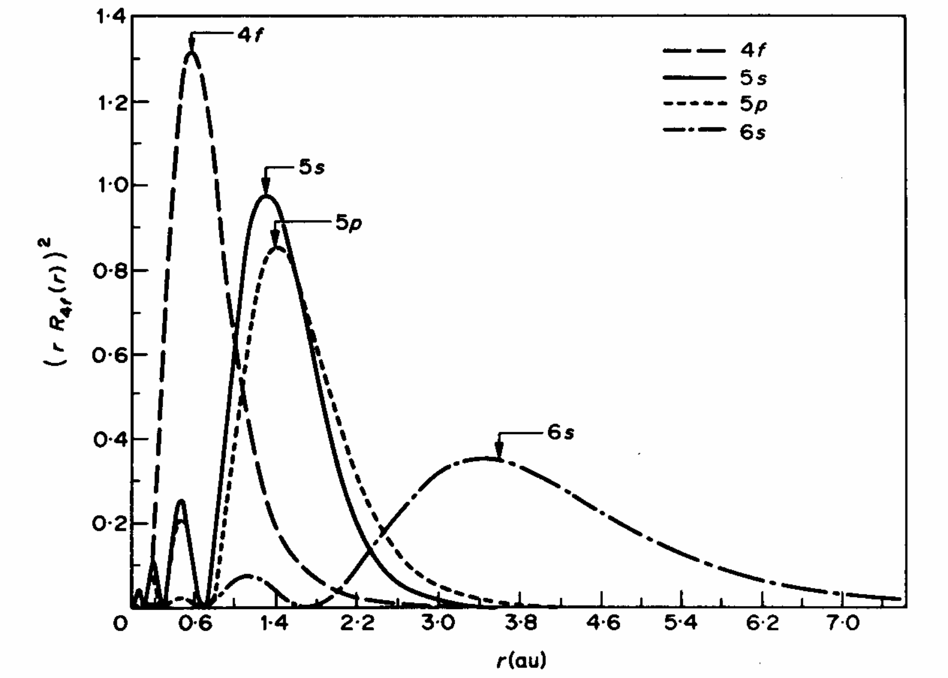

Fig. 3.1 Radial densities of the electrons of Gd^{3+} from Hartree-Fock calculations (after Taylor and Darby, 1972).

2.6.2. Hund's Rules

The magnetic properties of the rare earth elements are determined by the ground state configuration of the 4f electrons. The ground state is multiply degenerate with 2l+1 possible values of l_z and 2 possible values of S_z for a total of 2(2l+1) possible states. Fortunately, this degeneracy is removed by considering the Coulomb repulsion between the electrons and spin-orbit coupling (Mattis, 1981). The ground state configuration of a partially filled shell will then be governed by Hund's rules (Ashcroft and Mermin, 1976):

1. The ground state has the largest value of total spin **S** that is consistent with the exclusion principle.

2. The ground state has the largest value of total orbital angular momentum **L** that is consistent with the first rule and the exclusion principle.

3. For shells that are less than half-filled, the total angular momentum is given by **J** = |**L**-**S**|. For shells that are more than half-filled, **J** = |**L**+**S**|

These rules are useful in the study of rare earth magnetism, since knowledge of the number of f-electrons implies a knowledge of the quantum numbers of an atom, and hence, the magnetic properties. Table 3.1 shows the values of L, S, and J for the lanthanide ions. Now that the components of angular momenta are known for the local moments, it is possible to formulate many aspects of the theory of magnetism in rare earth intermetallic compounds.

2.6.3. The Curie-Weiss Law

In general, the contribution of a magnetic moment in an applied field to the total energy is simply the Zeeman term, $E = -\mu_B (\mathbf{L}+g_0\mathbf{S})\bullet\mathbf{H}$, where $\mu_B = e\hbar/2mc \approx 5.79\times10^{-8}$ eV/G is the Bohr magneton and $g_0 = 2[1+\alpha/2\pi+O(\alpha^2) + \ldots] \approx 2$ is the electronic g-factor. Since this energy is small, compared to the other energies of the system, the effect of the applied field may be taken as a perturbation. In second-order perturbation theory, the change in energy of state n is given by:

$$\Delta E_n(H) = \mu_B H \langle n | \vec{L} + 2\vec{S} | n \rangle + \sum_{n \neq m} \frac{\left| \langle n | \mu_B H \cdot \left(\vec{L} + 2\vec{S} \right) | m \rangle \right|^2}{E_n - E_m} . \tag{3.1}$$

The second term in the energy correction is the Van Vleck paramagnetic term (Ashcroft and Mermin, 1976). Typically, this contribution is small in rare earth elements with partially filled f-shells. If J is non-zero, the first term dominates the energy correction. This expression is simplified with the use of the Wigner-Eckart theorem:

$$\langle JLSJ_Z | \vec{L} + 2\vec{S} | JLSJ'_Z \rangle = g_J \langle JLSJ_Z | \vec{J} | JLSJ'_Z \rangle , \tag{3.2}$$

where g_J is the Lande’ factor defined as:

$$g_J = \frac{3}{2} + \frac{1}{2}\frac{S(S+1) - L(L+1)}{J(J+1)}. \tag{3.3}$$

This allows the saturation magnetization of the local moment in the absence of other contributions such as the crystal electric field, to be expressed simply as:

$$M_{Sat} = g_J \mu_B J \ . \tag{3.4}$$

This result, summarized in Table 3.1, is useful in the analysis of new rare-earth intermetallic compounds, since it allows the theoretical saturated moment to be compared to the measured value. Under certain circumstances, this comparison may then be used to determine the amount of rare earth element present in an unknown compound. In addition, knowledge of the theoretical saturated moment may also be used to identify easy and hard magnetic axes arising from the crystalline electric field, discussed below. Finally, this theoretical result may allow an estimate of the net distribution of moments in materials exhibiting metamagnetic transitions, which will be discussed in detail in Chapter 5.

To determine the temperature dependence of the magnetization it is instructive to analyze a system of N states, with energies E_n. The Helmholtz free energy of this system is given by:

$$F = -\frac{N}{\beta}\ln\sum_n e^{-\beta E_n(H)} \tag{3.5}$$

where $\beta = 1/k_BT$. The magnetization is the derivative of the free energy with respect to applied field given by:

$$M = -\frac{1}{V}\frac{\partial F}{\partial H}. \tag{3.6}$$

The temperature dependence of the leading term in the energy correction, and hence the magnetization, is given by:

$$M = -\frac{N}{V}\frac{\partial E_n(H)}{\partial H} = \frac{N}{V} g_J \mu_B J B_J \left(\beta g_J \mu_B JH\right), \tag{3.7}$$

where $\gamma = g_J\mu_B$ and B_J is the Brillouin function defined as:

$$B_J(x) = \frac{2J+1}{2J}\coth\left(\frac{2J+1}{2J}x\right) - \frac{1}{2J}\coth\left(\frac{1}{2J}x\right). \tag{3.8}$$

At high temperatures ($k_BT >> g_J\mu_BH$), the argument to the Brillouin function ($\beta g_J\mu_BJH$) is small, and the Brillouin function may be approximated as:

$$B_J \approx \frac{J+1}{3J}x + O(x^3). \tag{3.9}$$

Therefore, the molar susceptibility as a function of temperature at high temperatures is given by Curie's Law:

$$\chi = N_A \frac{(g_J\mu_B)^2}{3}\frac{J(J+1)}{k_BT} = \frac{C}{T}, \tag{3.10}$$

Table 3.1. Components of angular momentum L,S, J and calculated values of the Lande' g factor (g_J), saturated moment (M_{Sat}), effective moment ($p_{eff} = g_J\,[J(J+1)]^{1/2}$), and deGennes factor (dG) for the trivalent magnetic rare earth ions.

R	L	S	J	g_J	M_{Sat}	p_{eff}	dG
Ce	3	0.5	2.5	0.857	2.14	2.54	0.19
Pr	5	1	4	0.800	3.20	3.58	0.80
Nd	6	1.5	4.5	0.727	3.27	3.62	1.84
Pm	6	2	4	0.600	2.40	2.68	3.20
Sm	5	2.5	2.5	0.286	0.71	0.84	4.46
Eu	3	3	0	--	--	--	--
Gd	0	3.5	3.5	2.000	7.00	7.94	15.75
Tb	3	3	6	1.500	9.00	9.72	10.5
Dy	5	2.5	7.5	1.333	10.00	10.64	7.08
Ho	6	2	8	1.250	10.00	10.61	4.50
Er	6	1.5	7.5	1.200	9.00	9.58	2.55
Tm	5	1	6	1.167	7.00	7.56	1.17
Yb	3	0.5	3.5	1.142	4.00	4.54	0.32

where C is the Curie constant given by:

$$C = \frac{g_J^2 \mu_B^2 J(J+1)}{3k_B} = \frac{p_{eff}^2 \mu_B^2}{3k_B}. \tag{3.11}$$

Like the saturated moment, this result is extremely useful in the characterization of new rare earth intermetallic compounds, since at high temperatures, the slope of a plot of the inverse susceptibility ($1/\chi$) versus temperature is the Curie constant, C. From the determination of the Curie constant, the molar mass of the measured compound may be calculated if g_J and J are known from the choice of the rare earth element in the compound.

2.6.4. The RKKY Interaction

For systems with interacting local magnetic moments, the susceptibility may deviate from the Curie law due to exchange interactions between the local moments. As seen in Fig. 3.1, the overlap between f-electrons in neighboring rare earth ions will be extremely small which reduces the possibility of a direct exchange between the rare earth ions. Therefore, the primary interaction of the magnetic moments is indirect, via the polarization of the conduction electrons. Specifically, the localized spin of the 4f electrons interacts with the spin of the conduction electron, resulting in a polarization of the conduction electrons. This polarization then interacts with the spin of 4f electron localized on another rare earth ion. This is known as the RKKY interaction. Typically, this interaction is long-range and oscillatory, leading to a diverse assortment of magnetic structures. This section will be an overview of the details of the RKKY interaction, primarily following the derivation of Coqblin (1977).

The Hamiltonian of the interaction between localized 4f electrons and the conduction electrons may be expressed as:

$$H_{Int} = -\sum_n \Gamma(r - R_n)\vec{s}(r) \cdot \vec{S}_n \, , \tag{3.12}$$

where ***s*** is the spin of the conduction electrons, $\boldsymbol{S}_n$ is the spin of the 4f electrons, Γ is the interaction constant, r is the position of the conduction electron, and R_i is the position of the magnetic moment. This Hamiltonian may be expressed in second quantization as:

$$H_{Int} = \sum_{k,k',n} \Gamma\left(\vec{k}', \vec{k}\right) e^{i\left(\vec{k}-\vec{k}'\right)\vec{R}_n} \vec{S}_n \cdot \vec{s}_{k'k} \; . \tag{3.13}$$

Within this representation, the electronic states are taken to be Bloch waves with k and k' denoting the wavevectors of filled and unfilled states, respectively. Γ(k',k) is the interaction constant expanded in the basis of electronic wave functions. $\vec{S}_n$ is the spin of the nth local moment. The components of conduction electron spin $\vec{s}_{k'k}$ are given as:

$$\begin{aligned} s^z_{k'k} &= \tfrac{1}{2}\left(c^+_{k'+} c_{k+} - c^+_{k'-} c_{k'-}\right) \\ s^+_{k'k} &= c^+_{k'+} c_{k-} \\ s^-_{k'k} &= c^+_{k'-} c_{k+} \end{aligned} \tag{3.14}$$

with the operators $c^+{}_{k\sigma}$ and $c_{k\sigma}$, respectively, creating or annihilating an electron with wavevector *k* and spin σ equal to + or -. The Hamiltonian depends on both the filled (*k*) and unfilled (*k'*) electronic states. This is expected, since the electrons are fermions and the occupation of states is described by the Fermi-Dirac distribution. Therefore, any electronic excitation must be from an occupied to an unoccupied state.

Since the Hamiltonian is spin-dependent, the electrons with spin up will interact differently than those with spin down. This induces a polarization of the electron gas. This polarization is simply the difference in the spatial distribution of the perturbed wave functions for the spin up and spin down electrons. The perturbed wavefunction, $\phi_{k\sigma}$, is calculated using second order perturbation theory (Coqblin, 1977):

$$\phi_{k\sigma} = \phi^0_{k\sigma} + \sum_{k',\sigma'} \frac{\left\langle k^0\sigma \middle| H_{Int} \middle| k'^0\,\sigma' \right\rangle}{E_k - E_k'} \phi^0_{k'\sigma'} \,. \tag{3.15}$$

Performing the summation over the appropriate k-states and taking the difference between the spin up and spin down densities yields the polarization, P(r), of the conduction electrons.

$$P(r) = \frac{9\pi S_Z Z^2}{2\Omega^2 E_F} F(2k_F r)\,, \tag{3.16}$$

where Ω is the atomic volume, Z is the number of conduction electrons per atom, E_F is the Fermi energy and F(x), shown in Fig. 3.1, is given by:

$$F(x) = \frac{x\cos x - \sin x}{x^4}\,. \tag{3.17}$$

The exchange interaction between two rare earth atoms is indirect, via the polarization of the electron gas. The energy of this interaction may also be calculated within the framework of second-order perturbation theory:

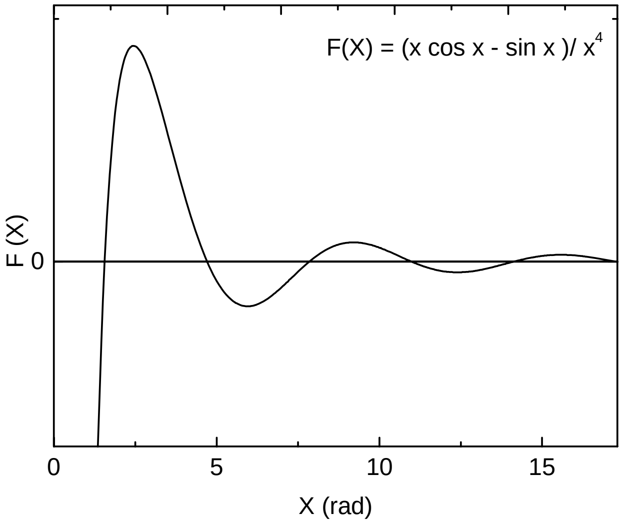

Figure 3.1 The polarization of the conduction electrons via the RKKY interaction.

$$E = \sum_{k,k',\sigma,\sigma'} \frac{\left\langle k^0\sigma \left| H_{Int} \right| k^{0'}\sigma' \right\rangle \left\langle k^{0'}\sigma' \left| H_{Int} \right| k^0\sigma \right\rangle f_k\left(1-f_{k'}\right)}{E_k - E_{k'}}. \tag{3.18}$$

In this expression, H_{int} is given by Eq. 3.13, f_k denotes the Fermi-Dirac distribution, and the summation is over the filled k states with spin σ and energy E_k, and unfilled k' states with spin σ' and energy $E_{k'}$. The summations in this expression may be simplified by only considering zero temperature. Therefore all states below E_F will be filled and all states above E_F will be empty. Substituting the Hamiltonian (Eq. 3.13) into (3.18) and performing the creation and annihilation operations yields:

$$E = \frac{m}{\hbar^2}\sum_{m,n}\vec{S}_n\cdot\vec{S}_m\sum_{k=0}^{k_F}\sum_{k'}\frac{e^{i\left(\vec{k}-\vec{k}'\right)\left(\vec{R}_n-\vec{R}_n\right)}}{\vec{k}^2-\vec{k}'^2}\left|\Gamma\left(\vec{k}-\vec{k}'\right)\right|^2 . \tag{3.19}$$

Finally, assuming Γ is not dependent on wavevector and performing the integration over the k-states yields the interaction energy:

$$E = \frac{9z^2\pi\Gamma^2}{2E_F}\sum_{n,m}\vec{S}_n\cdot\vec{S}_m F\left(2k_F\left|r_n-r_m\right|\right). \tag{3.20}$$

At low temperatures, k_BT is less than E, and the exchange interaction between the local moments will dominate, causing the magnetic sublattice to be ordered. Although the nature of this magnetic order depends upon on the electronic structure of the material through Γ and E_F, the strongest dependence arises through the oscillatory $F(2k_F|r_n-r_m|)$ term. Depending on the values of k_F and (r_n-r_m), the exchange between neighboring moments may be positive or negative, which will result in ferromagnetic or antiferromagnetic ordering, respectively. If interactions between more distant neighbors are considered, complicated magnetic structures may also arise, such as the helical, conical, or longitudinal wave structures present in pure rare earth metals (Jensen, 1991) or the various metamagnetic structures observed in applied fields in $HoNi_2B_2C$ (Canfield, 1997), $TbNi_2Ge_2$ (Islam, 1998), or $DyAgSb_2$ (Myers, 1999)

Within mean field theory, the magnetic field acting on each local moment (H_a) is the sum of the external applied field (H_0) and an effective field arising from the thermal average of the surrounding moments (H_{eff}), which will be proportional to the magnetization (M) of the local moments. Therefore, since the magnetization as a function of temperature follows Curie's law, the magnetization will be given by:

$$M = \frac{C}{T}\left(H_0 + H_{eff}\right) = \frac{C}{T}\left(H_0 + \alpha M\right), \tag{3.20}$$

where α is the proportionality constant in $H_{eff} = \alpha M$ and C is the Curie constant discussed previously. Therefore, the susceptibility (χ), which is M/H, yields the Curie-Weiss law:

$$\frac{M}{H_0} = \frac{C}{T - C\alpha}, \tag{3.21}$$

with $C\alpha$ equal to the Weiss paramagnetic temperature, θ_P. Since α is proportional to the exchange interaction, the paramagnetic temperature is:

$$k_B \Theta_p = -\frac{3\pi}{4} z^2 \frac{m^* \Gamma^2}{\hbar^2 k_F^2} S(S+1) \sum_{n \neq 0} F\left(2k_F \left|r_n - r_m\right|\right). \tag{3.22}$$

2.6.5. deGennes Scaling

It is frequently more convenient to express the Hamiltonian of the interaction between the local moments and the conduction electrons (Eq. 3.12) in terms of the total angular moment of the 4f electrons, **J**. Given that **L** + 2**S** =g_J**J** and **L** + **S** = **J**, the projection of **S** on **J** is (g_J-1)**J**, where g_J was previously defined. With Γ taken as a constant, the Hamiltonian (Eq. 3.12) then becomes:

$$H = -\sum_i \Gamma(g_J - 1)\vec{s} \cdot \vec{J}_i \; . \tag{3.23 }$$

The Weiss temperature will then be given by:

$$k_B \Theta_p = -\frac{3\pi}{2} z^2 \frac{m^* \Gamma^2}{\hbar^2 k_F^2} (g_J - 1)^2 J(J+1) \sum_{n \neq 0} F\left(2k_F |r_n - r_m|\right). \tag{3.24}$$

Within mean field theory, the ordering temperature would be expressed as:

$$T_M = \frac{9z^2 \pi \Gamma^2}{8E_F k_B} (g_J - 1)^2 J(J+1) \sum_{n,m} F\left(2k_F |r_n - r_m|\right). \tag{3.25}$$

Although the coupling between local moments is dependent on the electronic structure of the compound through k_F, E_f, m*, these parameters are approximately constant throughout a series as the trivalent rare earth is varied. Therefore, the most significant difference in the coupling will depend on the magnetic properties of the rare earth ion, through the de Gennes factor, $(g_J\text{-}1)^2J(J+1)$. Since the de Gennes factor is largest for Gd, compounds containing this element can be expected to have the highest ordering temperature. Likewise, compounds containing Pr, or Tm, typically order magnetically at much lower temperatures. It has been shown that for many compounds, T_N and θ_p, scale approximately linearly with the de Gennes factor (Canfield, 1998), confirming the assumptions of the electronic structure and the validity of the RKKY interaction.

2.7. Crystalline Electric Field

2.7.1. Overview of Crystal Electric Field

Although the exchange interaction may be anisotropic, the primary origin of anisotropies observed in the magnetic properties of rare earth intermetallic compounds is the crystalline electric field (CEF). In the absence of any perturbations, the electron levels of an ion are filled according to Hund's rules. If the ion is placed within a crystalline lattice, the electric field from the surrounding atoms may remove the degeneracy of the Hund's rule ground state multiplet. In transition metals with an unfilled 3d shell, this effect is quite large. However in the rare earth elements where the unfilled 4f shell is highly localized, the crystal field splitting is relatively small and may be treated as a perturbation of the ground state. This perturbation removes the degeneracy of the Hund's rule ground state, resulting in anisotropy in the magnetic properties of the rare earth ions. This introduction to the crystalline electric field primarily follows those found in Taylor and Darby (1972) and Elliot (1972).

If the surrounding atoms are treated as point charges at position R_i, the potential at the rare earth site is simply the sum of the potential from all of these point charges:

$$V(r_i) = \sum_i \frac{q_i}{\left|\vec{r} - \vec{R}_i\right|}. \tag{3.26}$$

This potential is a solution to Laplace's equation if the charge density from the surrounding ions does not overlap the rare earth ion, and may be expanded in spherical harmonics, $Y_l^m(\theta,\phi)$, as:

$$V(r) = \sum_l \sum_{m=-l}^{l} A_l^m r^l Y_l^m(\theta,\phi), \tag{3.27}$$

where

$$A_l^m = (-1)^m \frac{4\pi}{2l+1} \sum_j \frac{q_j}{R^{l+1}} Y_l^{-m}(\Theta_j, \Phi_j). \tag{3.28}$$

It is generally more convenient to express this result in tesseral harmonics Z_l^m defined by:

$$Z_l^{|m|} = 2^{-\frac{1}{2}}\left[Y_l^m + (-1)^m Y_l^{-m}\right] \tag{3.29}$$

$$Z_l^{|m|'} = 2^{-\frac{1}{2}}\left[Y_l^m - (-1)^m Y_l^{-m}\right].$$

Within this representation, the potential energy may then be expressed as:

$$V(r) = \sum_{l,|m|} r^l \left[B_l^{|m|} Z_l^{|m|} + B_l^{|m|'} Z_l^{|m|'}\right] \tag{3.30}$$

with,

$$B_l^{|m|} = \frac{4\pi}{2l+1} \sum_j \frac{q_j}{R_j^{l+1}} Z_l^{|m|} \,. \tag{3.31}$$

The number of terms in the CEF potential are restricted by the point symmetry at the rare earth ion, giving the following rules:

If the z-axis contains an m-fold rotation, then the potential contains terms with V_l^m.

If a center of inversion exists, then there will be no terms with odd *l*.

Finally, no elements of the potential will exist with *l* larger than 6. This arises from the calculation of the matrix elements of the potential with the 4f electrons. Since the angular part of the 4f wavefunctions are proportional to $Y_3^m(\theta,\phi)$, the angular integral in the matrix element given by

$$\int \left(V_3^{\mu}\right)^* V_l^m V_3^{\mu'} \sin\theta d\theta \,, \tag{3.32}$$

vanishes if *l* is greater than 6.

Since the effects of the CEF are small in rare earth ions compared to the spin-orbit splitting, the potential (Eq. 3.30) may be treated as a perturbation to the free-ion states. In principle, the eigenvalues of the CEF states may be found by diagonalizing the matrix elements of this potential.

2.7.2. Stevens Equivalent Operators

A much simpler method to calculate the effect of the CEF potential is to introduce the Stevens equivalent operators. It has been shown (Stevens, 1952) that the matrix elements of the crystal field Hamiltonian (Eq. 3.30) are proportional to a set of operators containing components of the total angular momentum, J. The Hamiltonian in this representation then becomes:

$$H_{CEF} = \sum_{n}\sum_{m=0}^{n}[A_n^m \langle r^n \rangle \theta_n]O_n^m = \sum_{n}\sum_{m=0}^{n} B_n^m O_n^m \qquad (3.33)$$

where O_n^m represents the expansion of the CEF potential shown in Table 3.2. The energy splitting of the Hund's rule multiplet may now be relatively easily calculated by applying the operators and diagonalizing the matrix elements. Examples of this process have been performed in detail for cubic symmetry in Talyor and Darby (1972) and Lea, Leask, and Wolf (1962). Finally, a method to numerically fit the crystal field parameters to experimental data is outlined in MacKeown and Newman (1987).

2.7.3. Determination of B_2^0 from Magnetic Susceptibility

If the point symmetry of the rare earth ion is tetragonal, the CEF Hamiltonian will consist of only five nonzero terms (Prather, 1961) (Wallace, 1973):

$$H_{CEF} = B_2^0 O_2^0 + B_4^0 O_4^0 + B_4^4 O_4^4 + B_6^0 O_6^0 + B_6^4 O_6^4 \qquad (3.34)$$

From an expansion of the magnetic susceptibility as a function of temperature, it has be shown (Boutron, 1973) (Wang, 1971) that the B_2^0 term of the Hamiltonian will be dominant at high temperatures, introducing an anisotropy in the Weiss paramagnetic temperatures:

Table 3.2 Operator equivalents and the standard notation for terms in the crystal electric field Hamiltonian.

Term in electrostatic potential	Operator equivalent	Standard notation
$\Sigma(3z^2-r^2)$	$\alpha_J\langle r^2\rangle[3J_z^2-J(J+1)]$	$\alpha_J\langle r^2\rangle O_2^0$
$\Sigma(35z^4-30r^2z^2+3r^4)$	$\beta_J\langle r^4\rangle[35Jz^4-30J(J+1)J_z^2+25J_z^2-6J(J+1)+3J^2(J+1)^2]$	$\beta_J\langle r^4\rangle O_4^0$
$\Sigma(x^4-6x^2y^2+y^4)$	$\beta_J\langle r^4\rangle[J_+^4+J_-^4]$	$\beta_J\langle r^4\rangle O_4^4$
$\Sigma(231z^6-315z^4r^2+105z^2r^4-5r^6)$	$\gamma_J\langle r^6\rangle[231J_z^6-315J(J+1)J_z^4+105J^2(J+1)^2J_z^2-525J(J+1)J_z^2+294J_z^2-5J^3(J+1)^3+40J^2(J+1)^2-60J(J+1)]$	$\gamma_J\langle r^6\rangle O_6^0$
$\Sigma(11z^2-r^2)(x^4-6x^2y^2+y^4)$	$\gamma_J\langle r^6\rangle(1/4)[(11J_z^2-J(J+1)-38)(J_+^4+J_-^4)+(J_+^4+J_-^4)(11J_z^2-\text{etc.})]$	$\gamma_J\langle r^6\rangle O_6^4$

Table 3.3 Crystal electric field parameters of rare earth ions. (Taylor and Darby, 1972) (Elliot, 1972)

Ion	α_J	β_J	γ_J	$\langle r^2\rangle$	$\langle r^3\rangle$	$\langle r^6\rangle$
Ce^{3+}	-5.71	63.5	0	1.200	3.455	21.226
Pr^{3+}	-2.10	-7.35	61.0	1.086	2.822	15.726
Nd^{3+}	-0.643	-2.91	-38.0	1.001	2.401	12.396
Pm^{3+}	0.771	4.08	60.8	0.935	2.130	10.4
Sm^{3+}	4.13	25.0	0	0.883	1.897	8.775
Tb^{3+}	-1.01	1.22	-1.12	0.758	1.44	5.8
Dy^{3+}	-0.635	-0.592	1.03	0.726	1.322	5.102
Ho^{3+}	-0.222	-0.333	-1.30	0.695	1.22	4.5
Er^{3+}	0.254	0.444	2.07	0.666	1.126	3.978
Tm^{3+}	1.01	1.63	-5.60	0.640	1.03	3.454
Yb^{3+}	3.17	-17.3	148.0	0.613	0.960	3.104

Furthermore, in uniaxial systems, such as tetragonal, $B_2^2 = 0$ (Wang, 1971). Therefore, the B_2^0 term in the CEF Hamiltonian may be determined from the difference in the Weiss paramagnetic temperatures:

$$B_2^0 = \frac{10}{3(2J-1)(2J+3)}(\theta_c - \theta_{ab})\,. \tag{3.36}$$

Since, within the point charge model, $B_2^0 = \alpha_J\langle r^2\rangle A_2^0$, the sign of B_2^0 will only depend on the sign of the Stevens multiplication factor, $\alpha_{J,}$ which only depends upon the rare earth ion. Note that a change of the sign of $\alpha_{J,}$ given in Table 3.3, is observed between Ho and Er. Therefore, if B_2^0 is the dominant term, and the moments align within the basal plane for $HoAgSb_2$, the moments of $ErAgSb_2$ will be along the c-axis. Finally, since A_2^0 is the expansion of the crystal field due to the surrounding ions, it should not vary significantly as different rare earth elements are used. A complete discussion of the experimentally determined values of B_2^0 is presented in Chapter 4.

2.7.4. Modification of Magnetic Ordering Temperatures Due to the CEF

Another effect of the anisotropy introduced by the crystal electric fields is the modification of the magnetic ordering temperatures, T_M. As discussed previously, if the RKKY interaction is the dominant interaction, T_M may be expected to scale with the deGennes factor, $(g_J-1)^2J(J+1)$. Noakes and Shenoy (1982) have proposed that the de Gennes scaling may be modified by the CEF anisotropy. Specifically, if the rare earth ion is in a position with tetragonal point symmetry and the CEF constrains the magnetic moments to be oriented along the c-axis, an enhancement in T_M will be observed. This effect has been experimentally observed in the RRh_4B_4 (Noakes and Shenoy, 1982) and RNi_2B_2C (Canfield, 1998) series of compounds.

2.8. Resistivity

Measurements of the transport properties of new materials frequently corroborate the findings of thermodynamic measurements and serve as valuable probes of the electronic structure. For example, the Curie temperature of ferromagnetic materials is generally difficult to determine directly from measurements of the temperature-dependent magnetization, since this feature is typically very broad. This is often not the case in measurements of the resistivity, where the resistivity sharply decreases below the Curie temperature, corresponding to a loss of disorder scattering from the magnetic moments. Transport measurements, such as electrical and thermal conductivity may also reveal properties that are not readily visible in the magnetization or specific heat, such as the appearence of gaps in the Fermi surface due the charge or spin density waves or superzone gaps arising from a periodicity in the magnetic order. Finally, the application of a magnetic field may drastically change the resistivity and provide a probe of the Fermi surface.

2.8.1. Matthiessen's Rule

The analysis of the zero-field resistivity is typically more difficult than that of thermodynamic properties such as magnetization and specific heat. Fortunately, much of this complexity may be removed through the use of Mathiessen's rule. Mathiessen's rule states that the total resistivity of a compound is the sum of the individual components of the resistivity (i.e.: $\rho(T) = \rho_{e\text{-}ph}(T) + \rho_{e\text{-}e}(T) + \rho_m(T) + \rho_i + \ldots$) (Ziman, 1967). If multiple scattering mechanisms exist, the total probability that an electron will be scattered is simply the sum of the probabilities of each scattering mechanism. Within the framework of Matthiessen's rule the individual contributions to the resistivity are additive and may be treated separately.

2.8.2. Impurity Scattering

At the lowest temperatures, scattering from impurities and imperfections is the dominant contribution to the resistivity. Due to the large variety of specific mechanisms contained within this term, no general expression adequately describes the magnitude of this contribution. However, the order of magnitude of these contributions is provided in previous studies (Ziman, 1967) on the effects of dislocations in Cu. In this specific case, the resistivity due to imperfections (ρ_i), increases as approximately 1.5 μΩ cm per atomic percent. It is important to note that the scattering due to nonmagnetic impurities and imperfections is independent of temperature. Therefore, at very low temperatures this is the only remaining contribution to the resistivity. The residual resistivity ratio (RRR) of a sample is generally defined as the ratio of the room-temperature resistance to the resistance extrapolated to 0 K [ρ(300 K)/ρ(0 K)], providing a measure of the degree of perfection of a sample.

2.8.3. Phonons

The dominant mechanism in the resistivity, at high temperatures, arises from electron-phonon scattering. At high temperatures, relative to the Debye temperature (θ_D), the number of phonons increases approximately linearly, since phonons follow Bose-Einstein statistics. This will cause the resistivity due to phonons ($\rho_{e\text{-}ph}$) to also increase approximately linearly with temperature. At low temperatures, the electronic distribution and the details of the electron-phonon interaction must also be included. Consideration of these factors leads to the Bloch T^5 law (Ziman, 1967):

$$\begin{aligned} &\rho_{e-ph} \propto T^5 \quad T \ll \Theta_D \\ &\rho_{e-ph} \propto T \quad\; T \gg \Theta_D \end{aligned} . \tag{3.37}$$

It should be noted that, at very high temperatures, the resistivity may saturate as the mean free path of the electrons becomes comparable to the interatomic spacing.

2.8.4. Spin-Disorder Scattering

In the paramagnetic state, the conduction electrons may scatter from the disordered local magnetic moments. Since this component of the resistivity depends upon the strength of the interaction between the conduction electrons and the local moments (Eqs. 3.13 and 3.23), it will scale with the de Gennes factor. Specifically, the magnitude of the magnetic component of the resistivity in the high temperature limit may be found using the Born approximation and the interaction Hamiltonian given by Eq. 3.13 (Coqblin, 1977):

$$\rho_m = \frac{\hbar k_F}{4\pi z}\left(\frac{m^*\Gamma}{e\hbar^2}\right)^2 (g_J - 1)^2 J(J+1). \tag{3.38}$$

In practice, measurement of this component of the resistivity is difficult since the sample geometry must be determined very precisely. Furthermore, the magnetic transition must be at a high enough temperature to allow a measurement of the residual resistivity without any contribution from the spin-disorder scattering. Although this may be possible in members of a series with R = Gd or Tb, the ordering temperature for R = Er or Tm is typically too small.

2.8.5. Electron-Electron Scattering

Finally, scattering may arise from electron-electron scattering. This contribution to the resistance is given by (Ashcroft and Mermin, 1976):

$$\rho_{e-e} = k_B T^2 \left(\frac{\pi^2\hbar^2}{mk_F}\right)^2 . \tag{3.39}$$

At room temperature this component to the resistivity is approximately 10^4 times smaller than the other mechanisms. Furthermore, at lower temperatures, the resistivity decreases as T^2 allowing this contribution to be neglected within the temperature regions of interest.

2.9. Magnetoresistance

2.9.1. The Hall Effect

Classically, an electron moving in a magnetic field is governed by the Lorentz force: **F**=-e**V**×**B**. This force bends the path of the electron into a helix with the axis parallel to the direction of the applied field. The angular velocity of the electron around this axis is simply the cyclotron frequency: $\omega_c = eB/m^*$. If the path is not bent sufficiently before the electron is scattered, no effect will be observed. In other words, $\omega_c\tau$ must be large for the observation of magnetoresistance, where τ is the relaxation time.

In general, the zero field resistivity of a material will be anisotropic, with principal axes corresponding to the crystal axes. The resistivity must now be expressed as the tensor, $\rho_{ij.}$ Ohm's law would then be given as: $E_i = \rho_{ij}J_j$ or $J_i = \sigma_{ij}E_j$. If a magnetic field is applied, the non-diagonal components of ρ_{ij} and σ_{ij} will not necessarily be zero. For example, if a magnetic field is applied along the z axis, and the current is along the x-axis, the components of the resulting electric field will be given by $E_x=\rho_{xx}J_x$ and $E_y=\rho_{xy}J_x$. The electric field induced perpendicular to the direction of the current (E_y) is the known as the Hall field. The magnitude of this field may be deduced by considering the equation of motion of an electron in a magnetic field:

$$\frac{d\vec{P}}{dt} = -ne\vec{E} + \vec{J} \times \vec{B} + \frac{m^*}{e\tau}\vec{J} = 0\,. \tag{3.40}$$

This equation may be solved to yield:

$$\begin{aligned} \sigma_0 E_x &= \omega_c \tau J_y + J_x \\ \sigma_0 E_y &= -\omega_c \tau J_x + J_y \end{aligned} \quad , \tag{3.41}$$

where $\sigma_0 = ne^2\tau/m^*$. Since the current is applied along the x-axis, $J_y = 0$ and $E_y = -\omega_c\tau/E_x$. Therefore, an electric field will be induced perpendicular to both the current density, J_x, and the applied magnetic field, H. For a single band of electrons, the Hall coefficient is given by $R_H = -1/ne$.

2.9.2. The Two Band Model

If the material contains only a single spherical electronic band, the Hall field will exactly cancel the deflection of the electrons due to the Lorentz force. In this case, the magnetoresistance will vanish. However, if multiple bands are present, the Hall field cannot completely cancel the Lorentz force for all of the charge carriers. The magnetoresistance for a metal with two spherical bands is given by (Ziman, 1967):

$$\frac{\Delta\rho}{\rho_0} = \frac{\sigma_1\sigma_2(\beta_1-\beta_2)^2 H^2}{(\sigma_1+\sigma_2)^2 + H^2(\beta_1\sigma_2+\beta_2\sigma_1)^2}, \qquad (3.42)$$

where $\beta_1 = e\tau_1/m_1c$, $\beta_2 = e\tau_2/m_2c$ and $\sigma_1 = n_1e^2\tau/m_1$ and $\sigma_2 = n_2e^2\tau/m_2$ are the zero field conductivities of bands 1 and 2, respectively. Several limiting cases of this expression should be analyzed. First, at low fields, the magnetoresistance is approximately proportional to H^2. Second, at high fields, the magnetoresistance saturates to the value:

$$\left(\frac{\Delta\rho}{\rho_0}\right)_{Sat} = \frac{\sigma_1\sigma_2(\beta_1-\beta_2)^2}{(\beta_1\sigma_2+\beta_2\sigma_1)^2}. \qquad (3.43)$$

Third, this saturation is not observed if $n_1 = n_2$ and the charge of the band 1 carriers is opposite to the band 2 carriers. In other words, if the metal is perfectly compensated with the number of holes equal to the number of electrons, no saturation will be observed in the transverse magnetoresistance. In practice, there are generally more than two electronic bands and these are seldom spherical. Calculation the magnetoresistance in these complicated cases is difficult and requires exact knowledge of the shape of the Fermi surface. Example calculations are given in Pippard (1989).

2.9.3. Fermi Surface Topology

Although the exact behavior of the magnetoresistance is complex to calculate, the overall response of the magnetoresistance is a function of the topology of the Fermi surface. The topology of a Fermi surface may be divided into two categories, closed and open orbits. In the case of a closed orbit, like a sphere, the transverse magnetoresistance will saturate at high fields regardless of the orientation of the current if the orbit is uncompensated. The magnetoresistance saturates because the electrons can execute complete orbits under the influence of an applied field, which essentially removes the ability of the electrons to contribute to the current.

Open orbits are more complex. In this case, the transverse magnetoresistance will saturate at all angles except when the applied magnetic field is parallel to the direction of the open orbit. In this case the electrons cannot complete a full orbit on the Fermi surface. Since the velocity of the electrons will always maintain a component in the direction of the current, the electrons will always contribute to the conductivity. Detailed studies of the angular dependence of the magnetoresistance may therefore be used to determine the direction of the open surface.

2.9.4. Kohler's Rule

Kohler's rule states that the change in resistance, $\Delta\rho$, due to the application of a magnetic field, H, is related to the zero-field resistivity ρ_0 by (Pippard, 1989):

$$\frac{\Delta\rho}{\rho_0} = F\left(\frac{H}{\rho_0}\right), \tag{3.44}$$

where F is a function depending on the electronic structure of the material. The important feature of this expression to note is that the zero-field resistivity, and hence the scattering rate, must be as small as possible to observe the largest change in resistivity due to the application of a magnetic field. Conceptually, this implies that for the observation of magnetoresistance, the electrons must be able to complete a significant portion of their orbit before being scattered by impurities or defects. A more formal justification of Kohler's rule is straightforward. Semiclassically, electrons will proceed in circular orbits with a circumference inversely proportional to the applied field. If the magnetic field and the scattering rate are increased by the same factor, the probability that an electron will complete an orbit will remain constant. Kohler's rule implies that it is advantageous to make magnetoresistance measurements on samples with the lowest possible zero-field resistivities. As mentioned previously, the dominant source of scattering at low temperature is due to impurities and lattice defects. However, a sudden increase in zero-field resistivity, such as the acquisition of magnetic scattering in the paramagnetic state, may also dramatically decrease the magnitude of the observed magnetoresistance. This effect is observed in $SmAgSb_2$ and will be discussed in Chapter 4.

2.10. The de Haas-van Alphen and Shubnikov-de Haas Effects

In addition to magnetoresistance, detailed analysis of the de Haas-van Alphen and Shunikov-de Haas effects can provide insight into the nature of the electronic structure of compounds. The effective masses of the orbits can be determined from the temperature dependence of the amplitudes of the oscillations. The angular dependence of the frequencies indicates the topology of parts of the Fermi surface. Although these quantum oscillations are typically measured only in extremely pure elements at the lowest obtainable temperatures and the highest possible fields, the oscillations are clearly observed in the RAgSb$_2$ series in modest fields and at remarkably high temperatures. This section will provide an overview of the origin of the quantum oscillations and the techniques used to obtain information concerning the electronic structure of the RAgSb$_2$ compounds. This section will principally follow the presentation of Shoenberg (1984).

2.10.1. The Origin of Quantum Oscillations

To determine the origin of quantum oscillations within solids, it is useful to first consider the free electron gas in the presence of a magnetic field. The solution of the energy levels of a electron in a 3-D infinite well with a magnetic field along the z-axis is given by:

$$\varepsilon_\nu(k_z) = \frac{\hbar^2 k_z^2}{2m} + \left(\nu + \tfrac{1}{2}\right)\hbar\omega_c \qquad (3.45)$$

where ω_c is the cyclotron frequency given by:

$$\omega_c = \frac{eH}{m^*}. \qquad (3.46)$$

Classically, this corresponds to the electrons moving in circular orbits normal to the z-axis. Since there is no component of the Lorentz force if the velocity is parallel to the z-axis, the angular and azimuthal quantum numbers, k_z and ν, are independent. Motion perpendicular to the z-axis is affected by the magnetic field, so the energy levels would be determined by ν. Since the orbital levels are quantized in the presence of a magnetic field, the electrons are constrained to have quantum numbers corresponding to cylinders in k-space. These cylinders, called Landau tubes, are shown in Fig. 3.3 for a spherical Fermi surface.

At very high quantum numbers, which is applicable to solids since only the electrons near the Fermi surface may contribute, the motion of the electrons may be treated semiclassically. Through the Bohr Correspondence principle, the difference in energy between two states is given by $\Delta E = 2\pi\hbar/T$ where T is the period of the oscillation. Semiclassically, this period may be expressed as:

$$T(E) = \frac{\hbar^2 c}{eH}\frac{\partial A(E)}{\partial E}, \tag{3.47}$$

where A is the area enclosed by the orbit. The area of the orbit will be a function of the applied field, given by the Onsager relation:

$$\Delta\left(\frac{1}{H}\right) = \frac{2\pi e\hbar}{c}\frac{1}{A_{ext}(E_F)}. \tag{3.48}$$

As the applied field increases, the Landau tubes move outward. When the cross sectional area of the Fermi suface is a maximum or a minimum, a sharp decrease in the

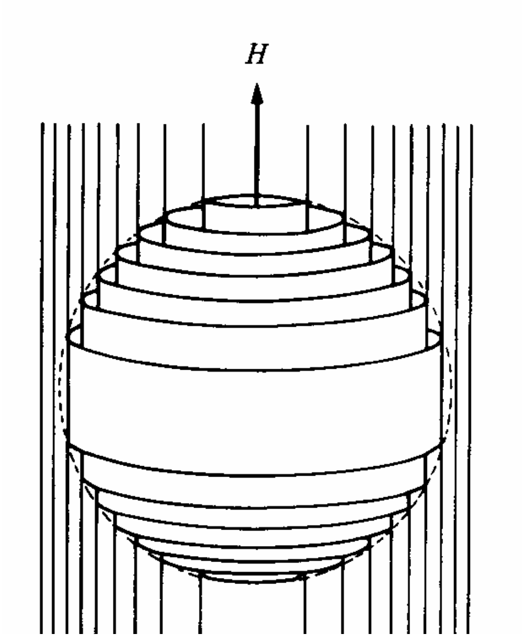

Fig. 3.3 Schematic diagram of Landau tubes for a spherical Fermi surface. The dotted line represents the Fermi surface in the absence of an applied field. (after Shoenberg, 1984).

density of states will result when the Landau tubes leave the Fermi surface. Therefore, a periodic variation of the density of states at the Fermi surface as a function of (1/H) will be observed. As seen in Fig. 3.2, this effect is greatest when the curvature of the Fermi surface in the direction parallel to the applied field is a minimum (as for a cylindrical surface). In this case, a large section of the Fermi surface will undergo the periodic variation as the field is varied. These quantum oscillations will be observed in any physical property that is dependent of the density of states at the Fermi surface, such as magnetism or resistivity.

Since the frequency of the observed oscillation is dependent on the minimal or maximal cross sectional areas in the plane perpendicular to the applied field, measurement of the frequency as a function of the angle of the applied field yields valuable information of the topology of the Fermi surface. For example, if a section of the Fermi surface is cylindrical, the frequency will be a minimum when H is parallel to the axis of the cylinder. As the applied field is rotated away from the axis, the cross sectional area, and hence the frequency will diverge as 1/cos(θ). Likewise, the angular dependence of the frequency of an ellipsoidal surface will follow:

$$F(\theta) \propto \frac{1}{\sqrt{\sin^2\theta + \left(\frac{c}{a}\right)^2 \cos^2\theta}}, \tag{3.49}$$

where θ is the angle away from the semi-major axis of the ellipsoid and c/a is the ratio of the semi-major to semi-minor axes.

2.10.2. Temperature Dependence and Determination of the Effective Mass.

So far, the discussion has been limited to zero temperature. Since the effect of temperature on the electronic structure in a metal is introduced through the Fermi-Dirac distribution, the Fermi surface becomes broader as the temperature increases. The result of this smearing is that each observed orbit on the Fermi surface at zero temperature will be replaced at finite temperature by a distribution of orbits, with subsequent distributions of frequencies and phases. The total contribution of this thermal distribution found by integrating the individual contributions, decreases the observed amplitude with increasing temperature. Detailed analysis (Shoenberg, 1984) shows that the functional form of the reduction of the amplitude of the pth harmonic of a given orbit as a function of temperature is given by:

$$R_T = \frac{\pi\lambda}{\sinh(\pi\lambda)}, \qquad (3.50)$$

where $\lambda = 2\pi pkT/\beta H$ and $\beta = e\hbar/m^*$. Note that at T =0 this term approaches 1, indicating no thermal broadening.

This result may be used to determine the effective mass of the observed orbit, since it is only dependent on temperature, applied field and effective mass. In practice, it is impossible to keep the field strictly constant as the temperature is varied, since oscillations must be observed as a function of 1/H. Therefore, the effective mass may be found by measuring the amplitude over large enough a field range for the accurate determination of the amplitude from the Fast Fourier Transform (FFT) of M(1/H). This is repeated at the same field ranges and data densities. Finally, the effective mass may be found by fitting Eq. 3.50 to the temperature dependent amplitude.

2.10.3. The Dingle Temperature

The addition of extra scattering mechanisms, through impurities or disorder, into the sample will attenuate the dHvA signal, by causing the electrons to be scattered out of their orbits. The electrons will now have a finite relaxation time (τ), which, through the uncertainty principle, results in a broadened Fermi energy. This smearing of the Fermi surface has a similar effect on the observed amplitude as an increase in temperature, and therefore may be characterized by a quantity known as the Dingle temperature. If the probability of scattering is represented by a Lorentzian distribution and is independent of the electronic structure, the corresponding reduction in amplitude will be given by:

$$R_D = e^{-\alpha p x / H}, \tag{3.51}$$

where x is the Dingle temperature and $\alpha = 1.469(m/m_0)\times10^5$ GK^{-1} (Shoenberg, 1984). Once the effective mass of the orbit is known, the Dingle temperature may readily be determined from the slope of a plot of $\ln[A_p H^n \sinh(\alpha pT/H)]$ as a function of 1/H, where n depends upon the measurement method (for measurements of the magnetization, n= ½).

2.10.4. The Lifshitz-Kosevich Equation

Now that the effects of finite temperature and impurity scattering have been described, it is possible to determine the magnitude of the quantum oscillations as a function of applied field, temperature, and the electronic structure of the material. This expression is known as the Lifshitz-Kosevich (LK) equation:

$$M = -\left(\frac{e}{c\hbar}\right)^{3/2} \frac{2FkTV}{\sqrt{2\pi H A''}} \sum_{p=1}^{\infty} \frac{\exp\left(-2\pi k x / \beta H\right)}{p^{3/2} \sinh\left(-2\pi k T / \beta H\right)} \sin\left[2\pi p\left(\frac{F}{H}\right) - \frac{1}{2} \pm \frac{\pi}{4}\right], \tag{3.52}$$

where A´´ is the second derivative of the cross sectional area of the Fermi surface along the direction of the applied field, and p is the number of the harmonic of the oscillation, x is the Dingle temperature, discussed previously. The importance of this expression resides in the assumption that neither the scattering mechanisms or the electronic structure vary as a function of applied field or temperature. In $SmAgSb_2$, as discussed in chapter 6, this expression appears to inadequately model the observed oscillations as the compound becomes magnetically ordered.

SYSTEMATIC STUDY OF ANISOTROPIC TRANSPORT AND MAGNETIC PROPERTIES OF RAgSb$_2$ (R= Y, La-Nd, Sm, Gd-Tm)

2.11. Introduction

Recent measurements (Bud'ko, 1998) on single crystals of the RSb$_2$ (R = La-Nd, Sm) series of orthorhombic compounds revealed a rich magnetic and electronic system with strong anisotropies, large, near-linear magnetoresistances [$\Delta\rho(55\text{kOe})/\rho(0)$ of SmSb$_2$ > 500], complex metamagnetic transitions, and de Haas-van Alphen oscillations accessible at relatively small fields. In addition, anomalous features in the temperature-dependent resistivities, possibly resulting from either charge or spin density waves are reported in PrSb$_2$ and NdSb$_2$.

This chapter will provide an overview of the anisotropic magnetization and transport properties of the RAgSb$_2$ series of compounds. Measurements of the magnetization along the c-axis and within the basal plane show strongly anisotropic behavior. In addition, the magnetization of some of the compounds is shown to be anisotropic within the plane. Resistivity measurements, as functions of temperature and applied magnetic field, highlight the excellent sample quality through large residual resistivity ratios and small residual resistivities. At low temperatures, the magnetoresistance of many of the compounds is extremely large, with $\Delta\rho/\rho$ approaching 60 for SmAgSb$_2$ in an applied field of 55 kOe.

2.12. Results and Analysis

2.12.1. $YAgSb_2$

$YAgSb_2$ has electronic and magnetic properties consistent with a non-magnetic, intermetallic conductor. The temperature-dependent resistivity of $YAgSb_2$ (Fig. 4.1) demonstrates metallic behavior, with a linear increase of resistivity with temperature and a residual resistivity ratio [ρ(300 K)/ρ(2 K)] of 17. Below 30 K, the impurity scattering becomes dominant with a residual resistivity at 1.8 K of 1.6 μΩcm. The magnetization as a function of temperature (Fig. 4.2) is approximately temperature independent with a mean value of about -2×10^{-4} emu/mol.

The transverse magnetoresistance of $YAgSb_2$ (lower inset, Fig. 4.1) is anisotropic, and linear for the field applied both parallel and perpendicular to the c-axis. The magnetoresistance for $H \parallel c$ is large, with $\Delta\rho(H=55\ \mathrm{kOe})/\rho(0) \approx 0.9$. The magnetoresistance is smaller $H \perp c$, with $\Delta\rho(H=55\ \mathrm{kOe})/\rho(0) \approx 0.26$.

2.12.2. $LaAgSb_2$

Overall, $LaAgSb_2$ is similar to $YAgSb_2$, except that a striking feature is observed in the resistivity [Fig. 4.3 (a)] of $LaAgSb_2$ near 212 K. Above 212 K, the resistivity increases linearly with increasing temperature. Below 212 K, there is a sharp change in $d\rho/dT$ with a weak local maximum in $\rho(T)$ just below 212 K, At even lower temperatures, the resistivity is resumes a linear temperature dependence. The lower inset of Fig. 4.3 (a) shows the effect of a magnetic field upon this transition where the application of 55 kOe causes the transition to shift upward in temperature by less than 1 K.

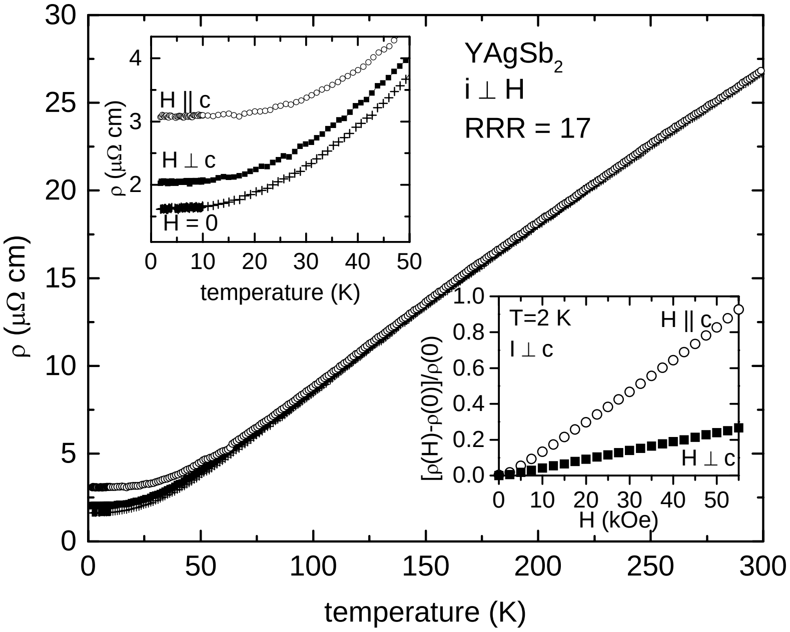

Fig. 4.1 Resistivity (ρ) versus temperature of YAgSb$_2$ for zero field (+)and 55 kOe for H || c (○) and H ⊥ c (■). Top inset: Expanded view of low temperature resistivity. Bottom inset: Transverse magnetoresistance, [ρ(H)-ρ(0)]/ρ(0) at 2 K for H || c (○) and H ⊥ c (■).

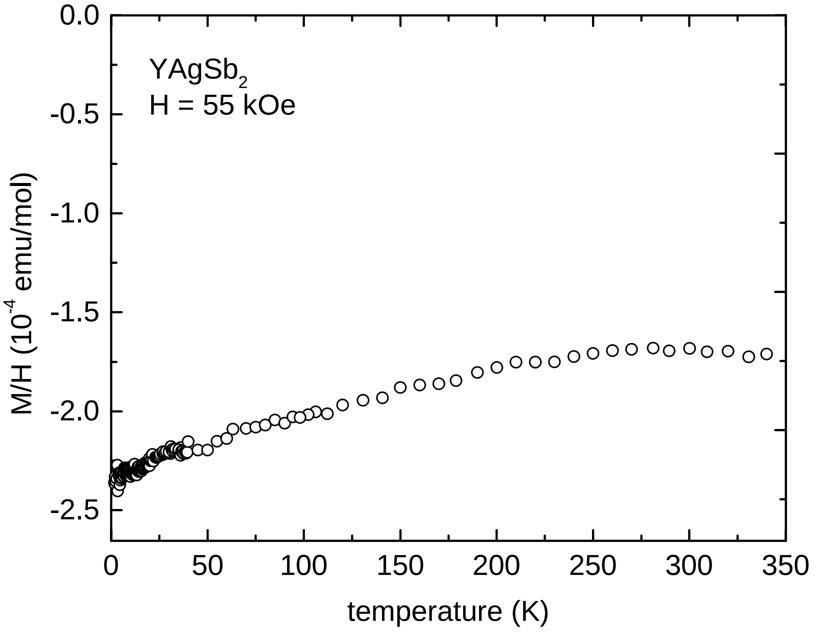

Fig. 4.2 Magnetization divided by a 55 kOe applied field (M/H) versus temperature for H || c (○) for YAgSb$_2$.

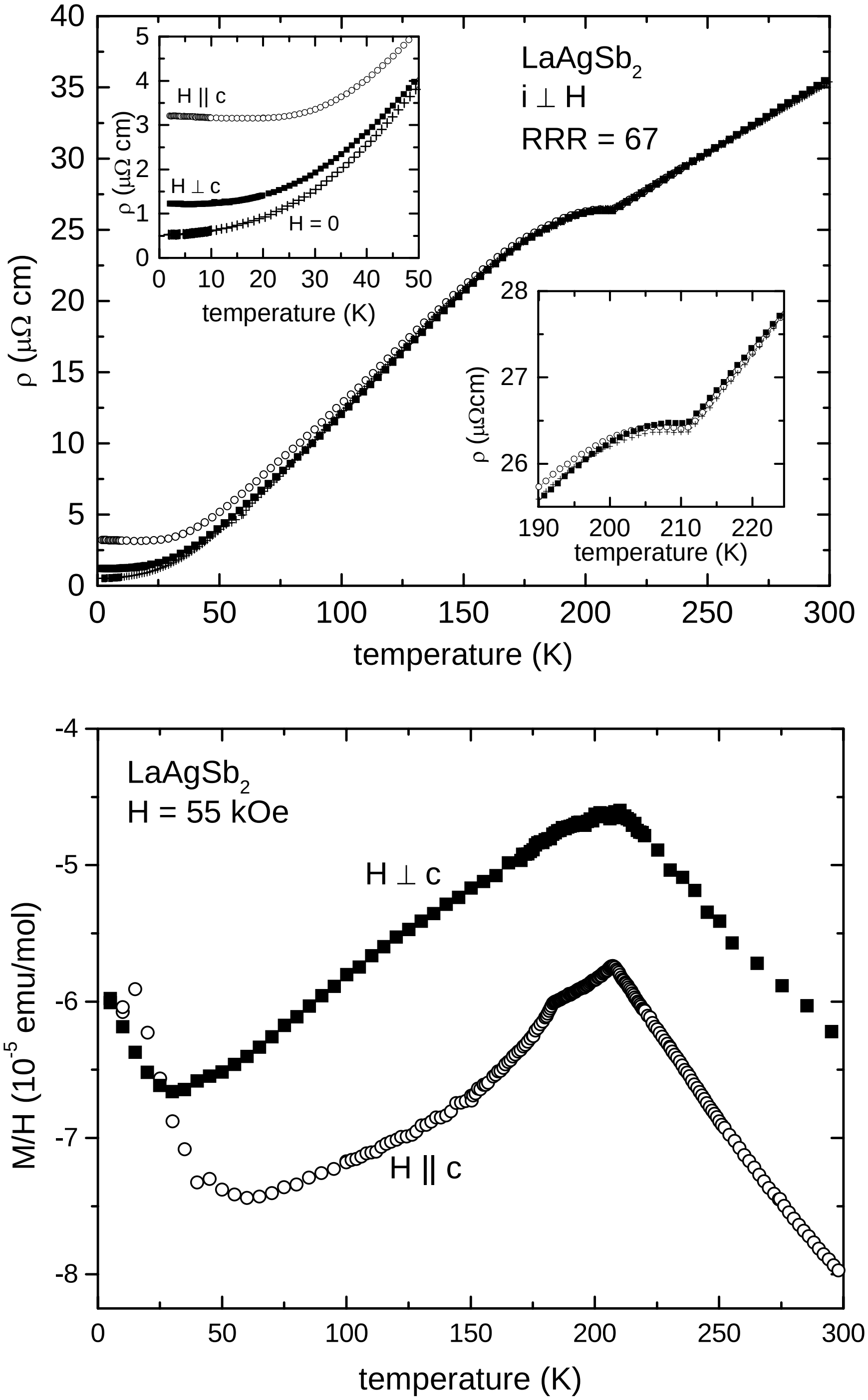

Fig. 4.3 (a) Resistivity (ρ) versus temperature of LaAgSb$_2$ for zero field (+) and 55 kOe for H || c (○) and H ⊥ c (■). Top inset: Expanded view of low temperature resistivity. Bottom inset: expanded view of the resistivity showing the anomalous behavior below 212 K. (b) Magnetization divided by a 55 kOe applied field (M/H) versus temperature for H || c (○) and H ⊥ c (■) for LaAgSb$_2$.

The magnetic susceptibility as a function of temperature of $LaAgSb_2$ is shown in Fig. 4.3(b). At low temperatures (<50 K) the susceptibility increases for both orientations, due to paramagnetic contributions from magnetic impurities. For H || c, peaks are observed at 184 K and 207 K. Although the 207 K maximum corresponds to the feature in the resistivity, no anomalies are present in the resistivity near 184 K. Applying the H $\perp$ c gives similar behavior, but only a broader 207 K peak is observed. This peak in the magnetic susceptibility, coupled with the resistive behavior, suggests the existence of either charge or spin density wave states creating a gap in the Fermi surface below 212 K.

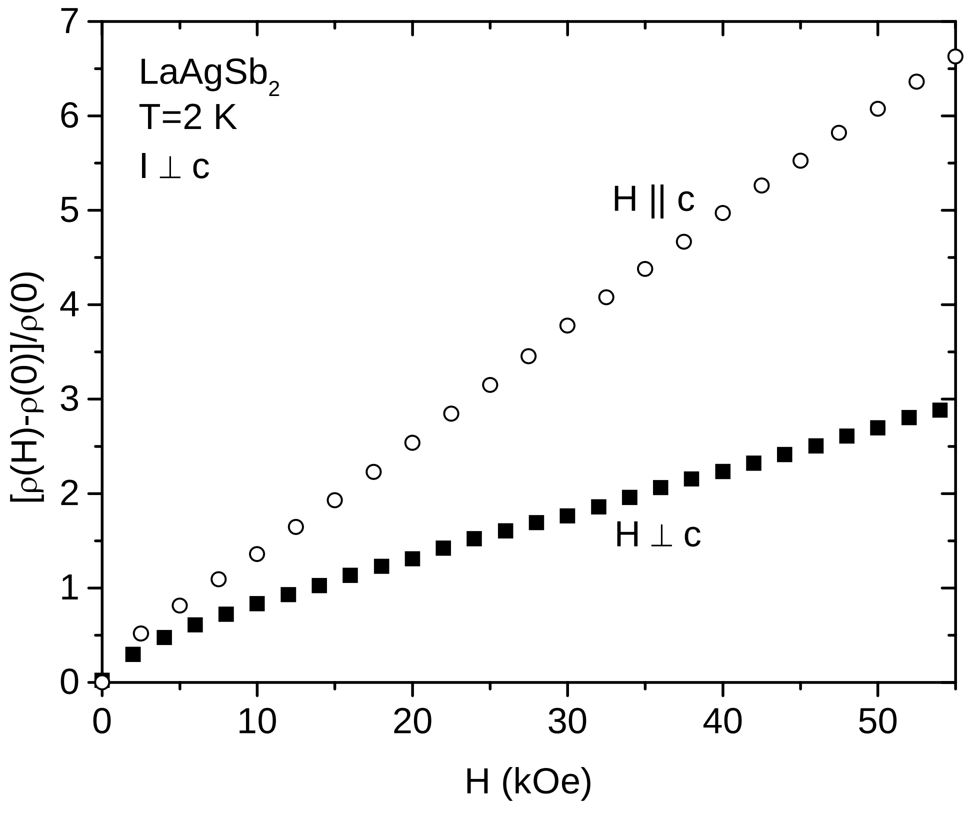

Fig. 4.4 Transverse magnetoresistance of $LaAgSb_2$ for both H || c (○) and H $\perp$ c (■) for T = 2 K.

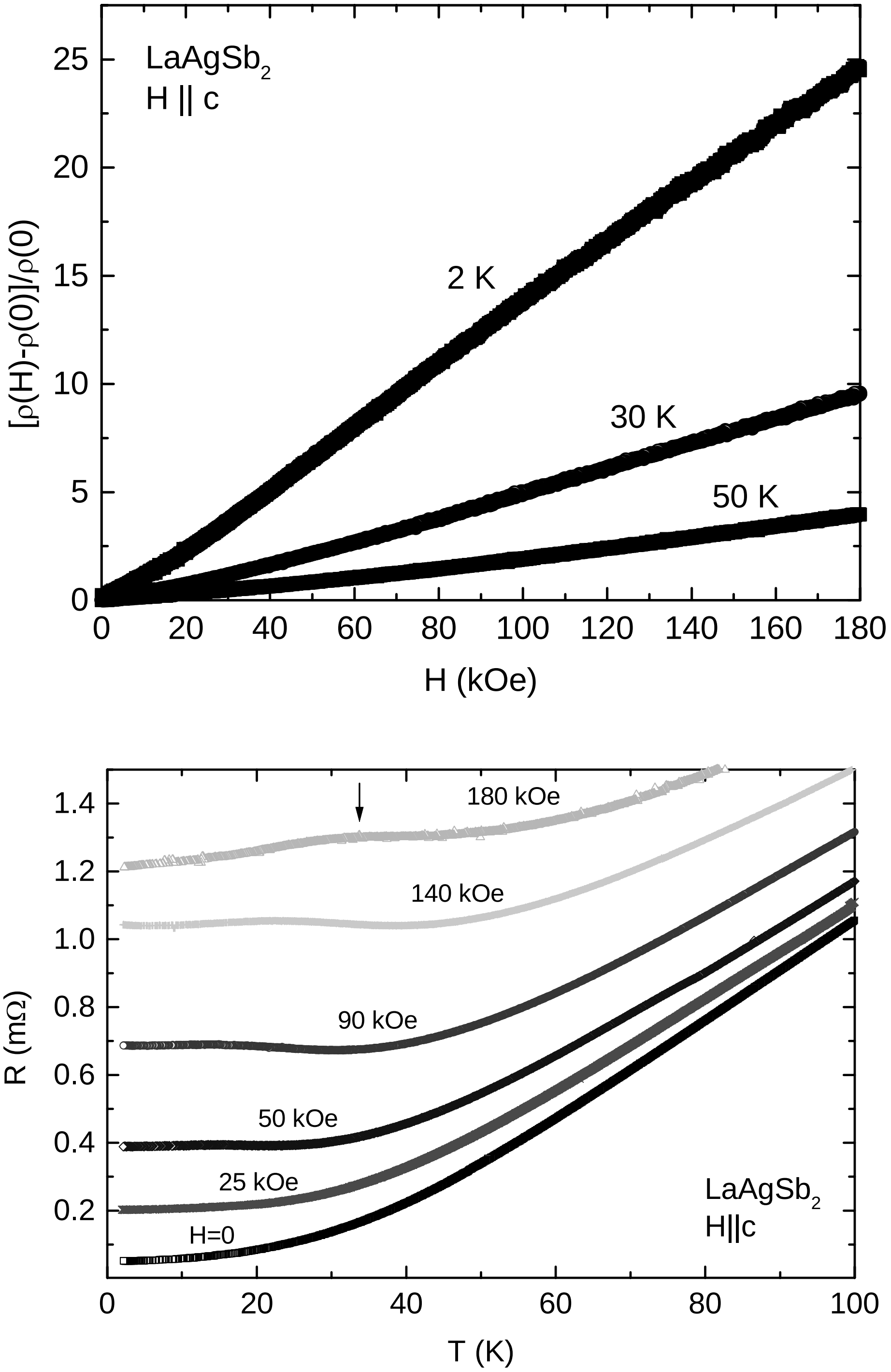

Fig. 4. 5 (a) High field transverse magnetoresistance isotherms of LaAgSb$_2$ for H || c at T = 2, 30 and 50 K. (b) magnetoresistance as a function of temperature for zero field, 25, 50, 90, 140, and 180 kOe. The arrow denotes the anomalous behavior appearing at high fields.

However, preliminary neutron diffraction measurements have failed to find any diffraction peaks below the transition arising from a spin density wave. From the change in the resistivity above and below this transition, the decrease in the number of carriers may be estimated to be about 5% of the total carrier density, assuming all the carriers have the same mobility.

The 2 K transverse magnetoresistance at low fields (Fig. 4.4) increases nearly linearly for both $H \parallel c$ and $H \perp c$, with maximum values obtained for $\Delta\rho(H=55\mathrm{kOe})/\rho(0)$ of 6.7 and 2.9, respectively. The magnetoresistance is still nearly linear with no saturation observed in high field transverse magnetoresistance isotherms up to 180 kOe [Fig. 4.5(a)], where for $H \parallel c$ $\Delta\rho(H=55\mathrm{kOe})/\rho(0) \approx 25$. As expected, the magnitude of the magnetoresistance decreases with increasing temperature, which is consistent with the increase of scattering in zero field at higher temperature and is a consequence of Kohler's rule. In addition, a weak local maximum appears at high fields in the temperature-dependent magnetoresistivity [Fig. 4.5(b)]. Although the origin of this anomaly is currently unknown, similar behavior is also present in the transverse magnetoresistance of $PrSb_2$ (Bud'ko, 1998) at high fields.

2.12.3. $CeAgSb_2$

$CeAgSb_2$ is a rare example of a Ce-based Kondo lattice system with low-temperature ferromagnetic ordering. At 2 K, the magnetization isotherms (Fig. 4.6) suggest that $CeAgSb_2$ is ferromagnetically ordered and at low fields has a net moment along the c-axis. Specifically, for $H \parallel c$, the magnetization rapidly rises to 0.37 μ_B/Ce (well below the expected full moment of 2.14 μ_B/Ce) below 400 Oe and remains constant for higher fields. This ferromagnetism is consistent with the hysteresis (inset, Fig. 4.6).

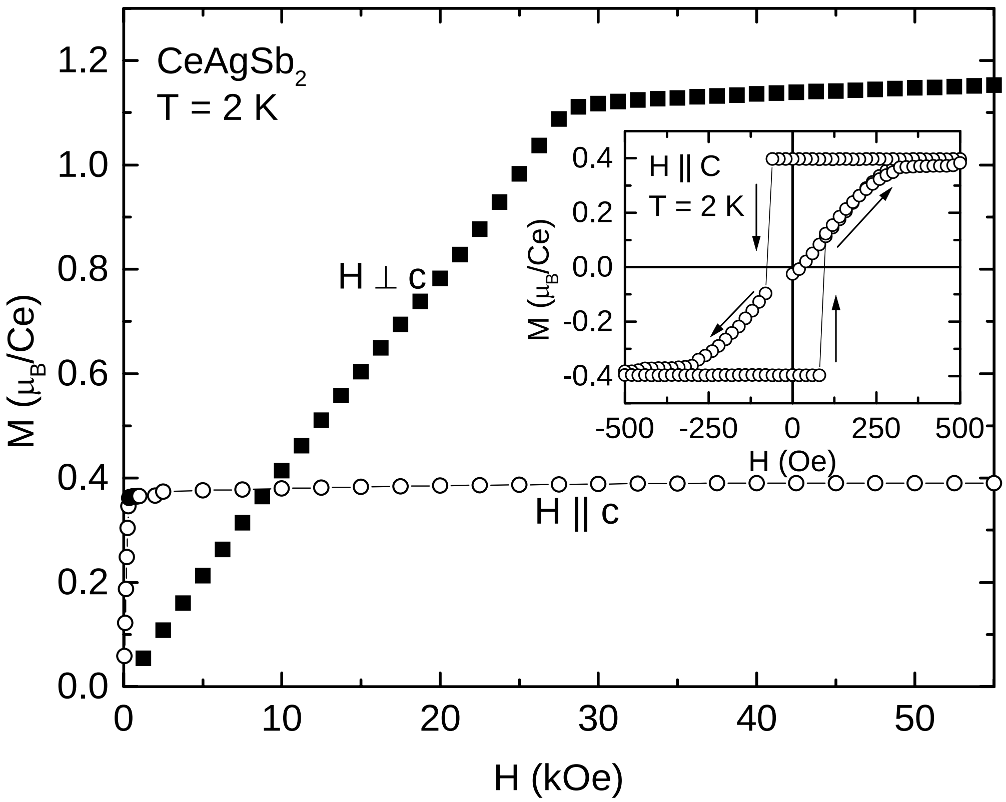

Fig. 4.6 Magnetization (M) versus applied field (H) of CeAgSb$_2$ for H || c (○) and H ⊥c (■) at 2 K. Inset: Hysteresis loop for H || c and T = 2 K. observed at 2 K.

The remnant magnetization is 0.37 μ_B/Ce with a field of –60 G required to decrease the magnetization from its saturated value. This unusual feature may be the result of a large energy required to nucleate an initial domain wall. On the other hand, for H ⊥ c, the magnetization increases nearly linearly to 1.1 μ_B/Ce below 30 kOe and then remains nearly constant for higher fields, possibly indicating the presence of a metamagnetic transition. These data are consistent with previous reports of M(H) of polycrystalline samples (Houshiar, 1995) (Sologub, 1994), and the existence of a complex (possibly conical) magnetic structure.

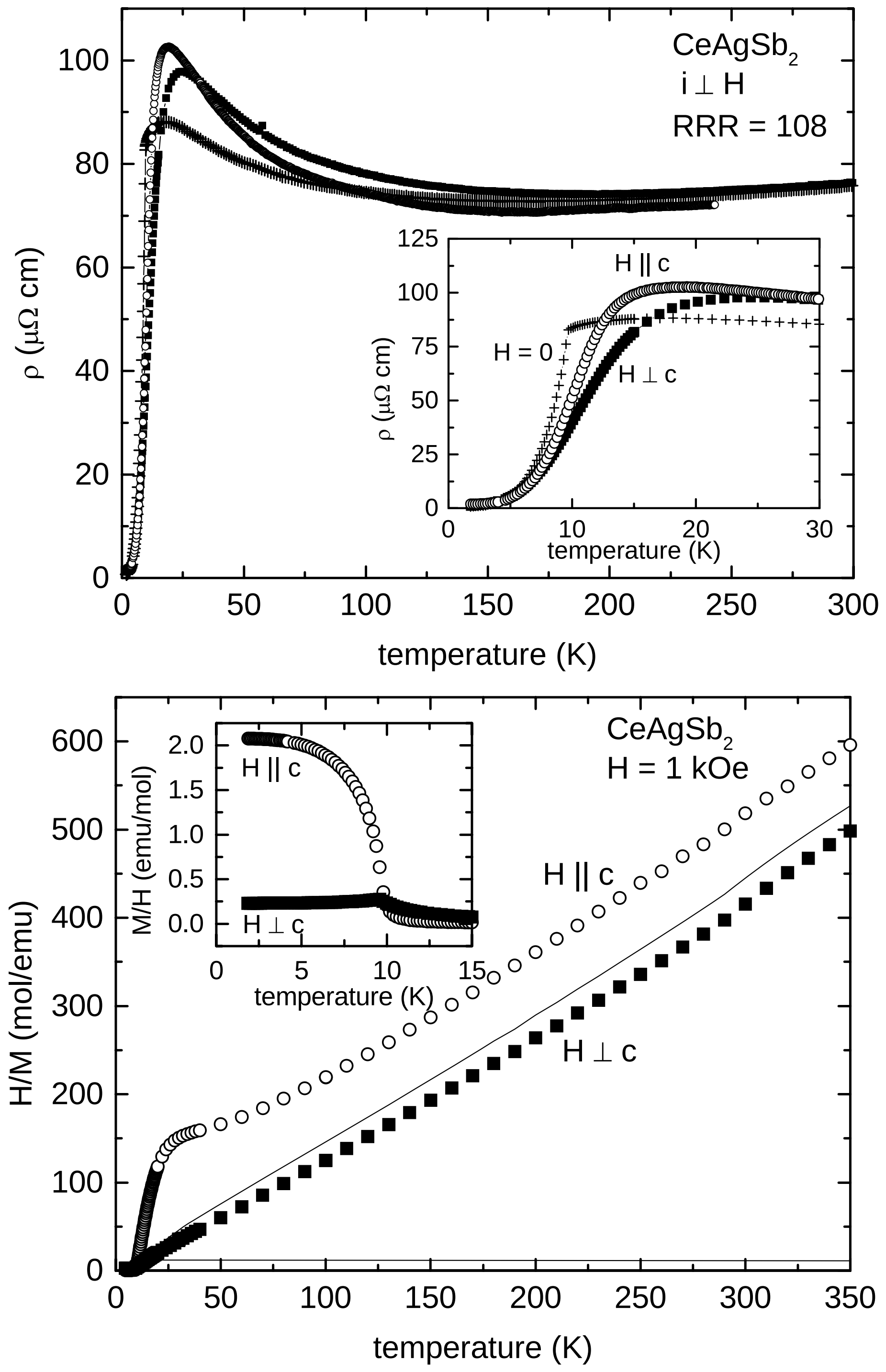

Fig. 4.7 (a) Temperature-dependent inverse susceptibility (M/H) of CeAgSb$_2$ in an applied field of 1 kOe for H || c (○), H ⊥ c (■), and the polycrystalline average (solid line). Inset: expanded view of M/H for low temperatures, showing the magnetic transition at 9.6 K. (b) Temperature-dependent resistivity of CeAgSb$_2$ in zero field (+), and in 55 kOe for H || c (○) and H ⊥ c (■). Inset: detail of resistivity below 30 K.

The temperature of the magnetic transition may be estimated from the temperature dependence of the magnetization [inset, Fig. 4.7(a)]. For H || c, the magnetization increases rapidly for T < 10 K, which is consistent with H along the easy axis of the ferromagnetically ordered state. On the other hand, for H ⊥ c, a peak at 9.6 K, indicates the magnetic transition. Above 200 K [Fig. 4.7(a)], the inverse susceptibility is linear, with a fit of the polycrystalline average, determined by $\chi_{poly}=(2\chi_{ab}+\chi_c)/3$, to the Curie-Weiss law giving an effective moment of 2.26 μ_B/Ce, somewhat smaller than the accepted theoretical value of 2.54 μ_B/Ce for trivalent Ce. The Weiss temperature of the polycrystalline average is 16.8 K, which is consistent with ferromagnetic interactions between the local moments. Finally, the anisotropic Weiss temperatures of –27.9 K for H || c and 34.6 K for H ⊥ c imply that the crystal electric field constrains the moments to the basal plane. This is in contrast to the low temperature and low field tendency for the moments to align axially, due to the anisotropic exchange interaction.

In zero field, the resistivity of $CeAgSb_2$ [Fig. 4.7 (b)] increases rapidly from 1.16 μΩ cm at 2 K to a maximum of 88.1 μΩcm at 18.2 K. At 9.7 K, a sharp change in the slope of the zero field resistivity is observed [inset Fig. 4.7(b)], consistent with a loss of spin-disorder scattering associated with the magnetic ordering as well as the possible suppression of the Ce hybridization due to the ferromagnetic ordering. At higher temperatures, the resistivity decreases to a broad local minimum near 150 K. The residual resistivity ratio [$\rho(300\text{ K})/\rho(1.8\text{ K}) \approx 66$] and the resistivity at 1.8 [$\rho(1.8\text{ K}) \approx 1.16$ μΩ cm] suggest good sample quality.

The temperature-dependent resistivity of $CeAgSb_2$ [Fig. 4.7 (b)] is typical of a Kondo lattice system. Preliminary inelastic neutron scattering measurements indicate a Kondo temperature (T_K) between 60 and 80 K (Thornton, 1998). This value of T_K is consistent with our initial measurements and analysis of specific heat of a variety of $Ce_xLa_{1-x}AgSb_2$ compounds ($\gamma \approx 200$ mJ/mol Ce K) (Bud'ko 1998). However, such a large T_K is inconsistent with the magnitude of the saturated moment in $CeAgSb_2$ at low temperatures, which for $H \perp c$ at 2 K is approximately 1.1 μ_B/Ce. Furthermore, measurements of the change in entropy up to T_C are almost Rln2/(mole Ce) in the $Ce_xLa_{1-x}AgSb_2$ compounds, which suggest that T_K is comparable to, or less than, T_C. Further analysis is currently the subject of ongoing research (Bud'ko, 1998).

The magnetoresistance of $CeAgSb_2$ [Fig. 4.7(b)] is either positive or negative, depending on the temperature and orientation of the applied field. This complexity is due to competing contributions from the Ce hybridization, magnetic ordering, and the electronic structure of the compound. To further resolve this behavior, magnetoresistance isotherms were acquired at 2, 5, 11 and 30 K (Fig. 4.8). At 2 K, The magnetoresistance is positive for both orientations up to at least 55 kOe. For $H \perp c$, an anomaly is present below 30 kOe, corresponding to the field-induced transition observed in the 2 K M(H) data (Fig. 4.6). At 5 K, the peak corresponding to the planar metamagnetic transition is still observed in the $H \perp c$ data, but the magnetoresistance becomes negative at high fields. The difference between the 2 K and 5 K data suggests that at low temperatures, the normal positive metallic magnetoresistance dominates. The larger response for $H \parallel c$ is consistent with the rest of the $RAgSb_2$ compounds. However, as the temperature increases, this contribution, which is

Fig. 4.8 Transverse magnetoresistance [$\Delta\rho(H)/\rho_0$] of $CeAgSb_2$ at 2, 5, 11, and 30 K for H || c (○) and H $\perp$ c (■). Note the different vertical scales for each temperature.

expected to follow Kohler's rule, diminishes due to increased scattering, which will be discussed later. This allows the negative magnetoresistance arising from the applied field polarizing the local moments and reducing the spin disorder scattering (Yamada, 1972) to dominate at higher temperatures.

Above T_C, $CeAgSb_2$ is a paramagnetic Kondo lattice. The magnetoresistance of a paramagnet is expected to be negative, since the local moments try to align parallel to the applied field, which essentially reduces the spin disorder scattering as the field is increased. Clearly, this effect will be more pronounced if the field is applied along the easy axes of the local moments. On the other hand, previous measurements (Flouquet, 1988) (Fierz, 1988), and theoretical models (Chen, 1993) (Kawakami, 1986) have indicated the possibility that at temperatures well below T_K, the magnetoresistance of a Kondo lattice may be positive and exhibit a maximum at an applied field determined by its electronic structure. Within these models, the magnitude of this maximum increases and moves to lower fields, eventually decreasing monotonically, as the temperature approaches T_K. The transverse magnetoresistance of $CeAgSb_2$ at temperatures above T_C (Fig. 4.8) is consistent with the presence of these two mechanisms. The 11 K magnetoresistance at low fields is positive for both $H \parallel c$ and $H \perp c$, consistent with the Kondo effect. At higher fields, the magnetoresistance becomes negative as the field saturates the paramagnetic ions. The magnitude of this decrease is larger for $H \perp c$, which is the single ion easy axis determined from the M(T) data [Fig. 4.7 (a)]. At 30 K, the negative paramagnetic contribution is suppressed by the much higher temperature. This allows the possible contribution from the Ce hybridization to be the dominant mechanism and leads to a positive transverse magnetoresistance. Further analysis of the details of magnetoresistance in Kondo compounds is outside the scope of this work and is currently the study of ongoing research (Bud'ko, 1998).

2.12.4. $PrAgSb_2$

At high temperatures, magnetization measurements demonstrate that $PrAgSb_2$ is a Curie-Weiss paramagnet. Fitting the polycrystalline average of the inverse susceptibility above 100 K to the Curie-Weiss law yields an effective moment of 3.63 μ_B per Pr and a Weiss temperature of –7.2 K [Fig. 4.9(a)]. Anisotropic Weiss temperatures of -48.5 K for H $\parallel$ c and 6.3 K for H $\perp$ c imply that the local moments tend to align within the basal plane. The resistivity at high temperatures [Fig. 4.9(b)] is similar to the rest of the $RAgSb_2$ series, manifesting typical metallic behavior. The RRR of $PrAgSb_2$ was 143, which suggests extremely small amounts of impurity and dislocation scattering.

Unlike the rest of the $RAgSb_2$ series with magnetic rare earth elements, no magnetic ordering is observed in $PrAgSb_2$ for T >1.8 K. Although a maximum in the H $\parallel$ c magnetization [inset, Fig. 4.9(a)] is observed at 3.1 K. No corresponding loss of spin-disorder scattering is present in the resistivity [inset Fig. 4.9 (b)]. Instead, the zero-field resistivity decreases smoothly below about 10 K from 3.5 $\mu\Omega$ cm to 0.23 $\mu\Omega$ cm.This behavior of both the magnetization and resistivity is typical of a material possessing a non-magnetic ground state.

The 2 K magnetic isotherms (Fig. 4.10), demonstrate a much larger magnetization for H $\perp$ c than for H $\parallel$ c. In addition, for H $\perp$ c the magnetization increases more rapidly than expected for a J = 4 Brillouin function and tends to saturate at higher fields. This is consistent with either the presence of a field induced magnetic transition. On the

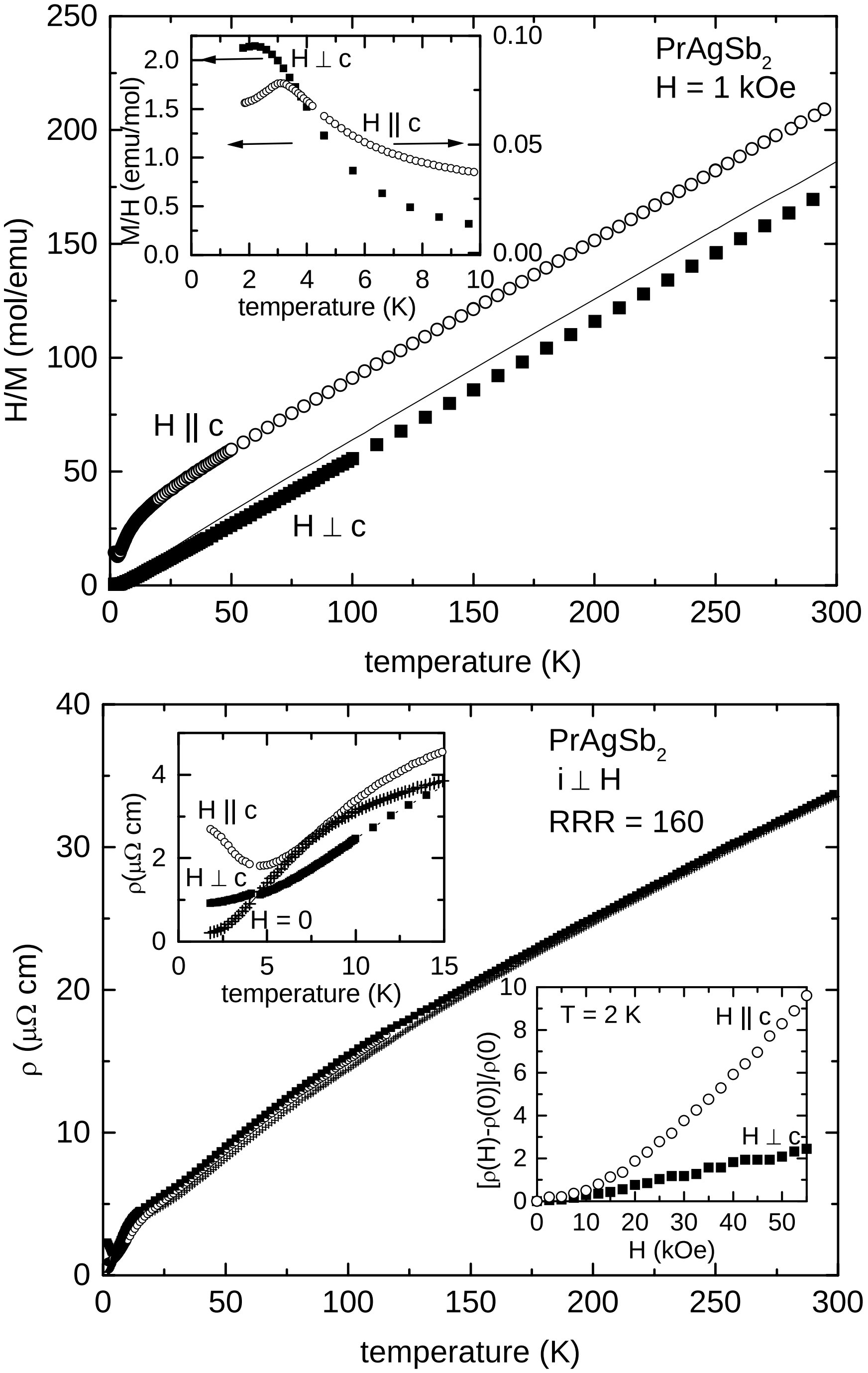

Fig. 4.9 (a) Temperature-dependent inverse susceptibility (M/H) of PrAgSb$_2$ in an applied field of 1 kOe for H || c (○), H ⊥ c (■), and the polycrystalline average (solid line). Inset: expanded view of M/H for low temperatures. (b) Temperature-dependent resistivity of PrAgSb$_2$ in zero field (+), and in 55 kOe for H || c (O) and H ⊥ c (■). Top inset: detail of resistivity below 10 K. Bottom inset: transverse magnetoresistance at 2 K for H || c (O) and H ⊥ c (■).

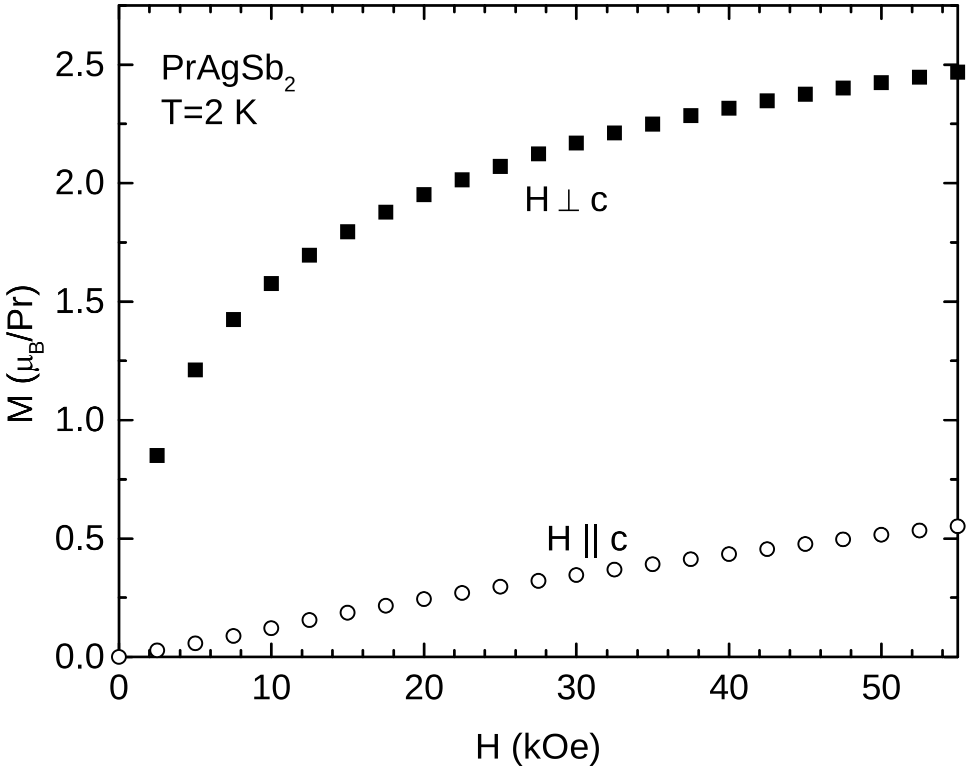

Fig. 4.10 Magnetization (M) versus applied field (H) of PrAgSb$_2$ for H || c (○) and H ⊥c (■) at 2 K.

other hand, M(H) is linear for H || c, and only reaches 0.5 μ_B/Pr at 55 kOe.

To clarify this low temperature behavior, the temperature-dependent specific heat was measured for PrAgSb$_2$ and LaAgSb$_2$, as shown in Figure 4.11. A broad maximum centered at 6.5 K may be associated with the Schottky effect arising from a CEF splitting of the Hund's rule ground state multiplet. The sum of the electron and phonon contributions to the specific heat of PrAgSb$_2$ may be approximated by the specific heat of LaAgSb$_2$, allowing a separation of the Schottky contribution [$\Delta C_p \approx C_p(\text{PrAgSb}_2) - C_p(\text{LaAgSb}_2)$] for a two level system given by:

$$C_{Sch} = R\left(\frac{\Delta}{T}\right)^2 \frac{g_0}{g_1} \frac{\exp\left(\frac{\Delta}{T}\right)}{\left[1+\left(\frac{g_0}{g_1}\right)\exp\left(\frac{\Delta}{T}\right)\right]^2},$$

where R is the universal gas constant, Δ is the energy separation in K, and g_0 and g_1 are the degeneracies of the two levels. Fitting this function (solid line in Fig. 4.11) to ΔC_p gives reasonable agreement with the experimental data with $\Delta \approx 18$ K and $g_0/g_1 \approx 0.35$. The change in entropy of the system up to 20 K, found by integrating $\Delta C_P/T$ with respect to T up to 20 K, is approximately Rln(3.8), consistent with a 4 state system. Although the change in entropy and parameters of the fit to C_{sch} suggest the existence of a singlet ground state and a triply

Fig. 4.11 Temperature dependence of the specific heat (C_p) for $PrAgSb_2$ (○), $LaAgSb_2$ (■), and their difference (ΔC_p, +). The solid line ($\Delta C_{p\ fit}$) is a fit to a two level Schottky system. The dashed line is the integrated change in entropy from 0 K.

degenerate excited state, the deviation of ΔC_p at higher temperatures may indicate a more complex set of levels.

The bottom inset to Fig. 4.9 (b) shows the transverse magnetoresistance in $PrAgSb_2$ at 2 K. For H || c the magnetoresistance is large, reaching a maximum of nearly 10 at 55 kOe. A power law fit shows that $\Delta\rho(H)/\rho(0) \propto H^{1.5}$. At 55 kOe, the H || c magnetoresistance decreases as the temperature is increased to 4 K. This is a consequence of Kohler's rule and will be discussed in detail in Section 4.3.6. For H ⊥ c, $\Delta\rho(H)/\rho(0)$ only reaches 2.2 but still significantly deviates from quadratic behavior with $\Delta\rho(H)/\rho(0) \propto H^{1.3}$. This component of the transverse magnetoresistance remains positive below 4.6 K, but becomes negative between 4.6 K and 15 K.

2.12.5. $NdAgSb_2$

Figure 4.12 (a) shows the inverse susceptibility of $NdAgSb_2$ in a 1.0 kOe field for H || c and H ⊥ c, with the inset showing an expanded view of the magnetization for low temperatures. Magnetic ordering is observed below 3.0 K, as determined by the maximum in $d(\chi T)/dT$, which is has a temperature dependence similar to the magnetic specific heat near an antiferromagnetic transition (Fisher, 1962). Above 100 K, the inverse susceptibility is linear for both orientations. Fitting the polycrystalline average to the Curie-Weiss law gives an effective moment of 3.6 μ_B/Nd and a Weiss temperature of –14.2 K. Anisotropic Weiss paramagnetic temperatures are θ_p^c = -45.3 K and θ_p^{ab} = -4.0 K, suggesting antiferromagnetic interactions with the moments constrained to the basal plane.

At low temperatures [inset, Fig. 4.12(b)], an abrupt decrease in the resistivity is consistent with the loss of spin disorder scattering near the magnetic ordering temperature, determined by the maximum in dρ/dt at 2.8 K. The large RRR of the sample studied [ρ(300 K)/ρ(1.8 K) ≈ 60] and low resistivity at 1.8 K, (0.51 μΩ cm) are consistent with very low impurity concentrations. At an applied field of 55 kOe, the resistivity for H || c, has a slight upturn below 3 K, the origin of which will be discussed later.

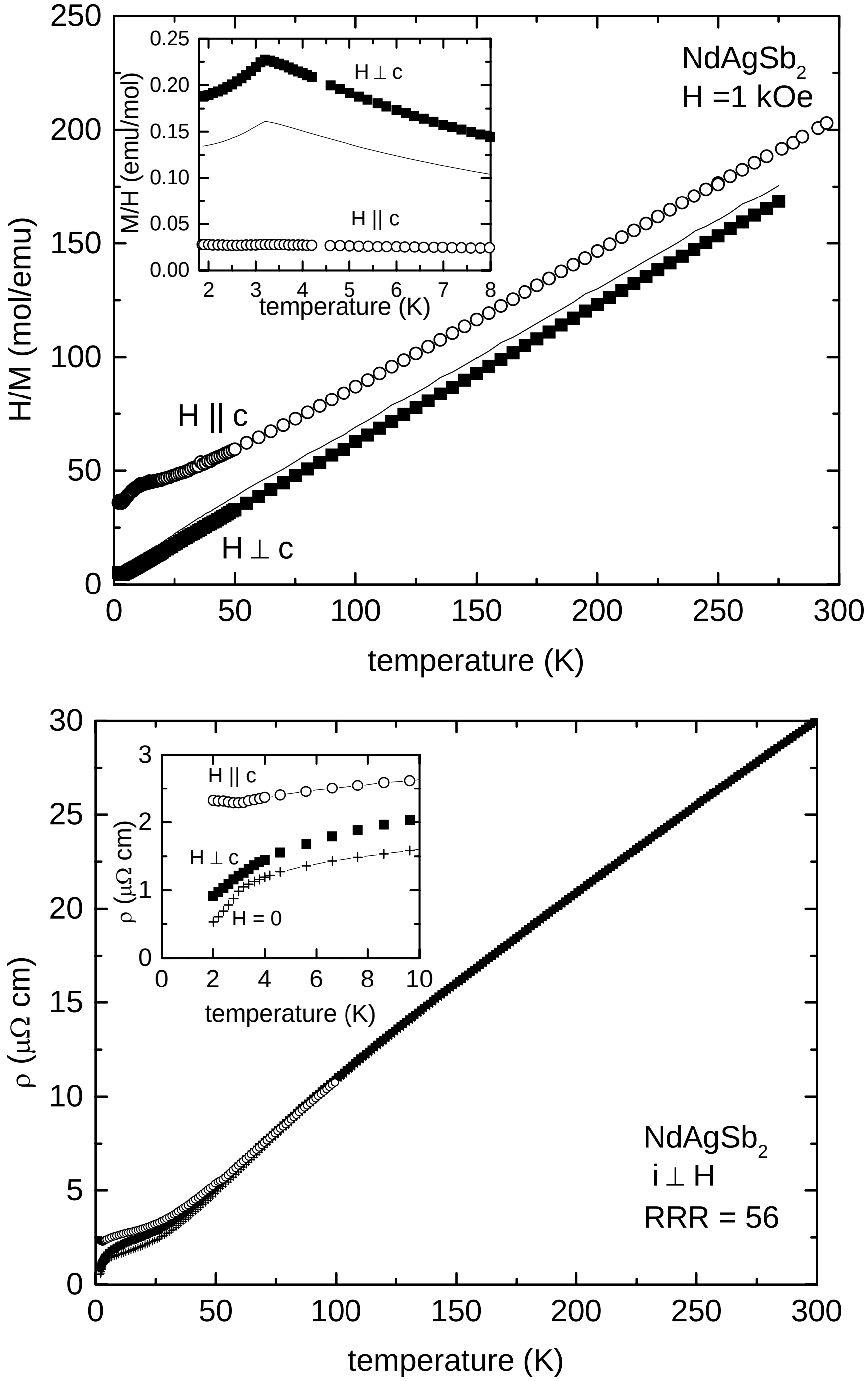

Fig. 4.12 (a) Temperature-dependent inverse susceptibility (M/H) of NdAgSb$_2$ in an applied field of 1 kOe for H || c (○), H ⊥ c (■), and the polycrystalline average (solid line). Inset: expanded view of M/H for low temperatures, showing the magnetic transition at 3.0 K. (b) Temperature-dependent resistivity of NdAgSb$_2$ in zero field (+), and in 55 kOe for H || c (○) and H ⊥ c (■). Inset: detail of resistivity below 10 K.

Magnetization isotherms at 2 K (Fig. 4.13), show that for H || c the magnetization is nearly linear, reaching only 0.2 μ_B/Nd at 55 kOe. However, for H ⊥ c, a weak positive curvature in M(H) between 20 and 30 kOe suggests the existence of a broadened metamagnetic transition. At 55 kOe, the planar magnetization is still only about 2.1 μ_B/Nd, well below the expected saturated magnetization of 3.27 μ_B for a free Nd^{3+} ion. It is possible that an additional metamagnetic transition may lie beyond the maximum field of our magnetometer. The transverse magnetoresistance of $NdAgSb_2$ at 2 K (Fig. 4.13) is large [$\Delta\rho(55\ kOe)/\rho(0) \approx 3.4$], positive and nearly linear for H || c. For H ⊥ c, the magnetoresistance rises to a broad maximum near 32 kOe, and then decreases for higher applied fields, consistent with the metamagnetic transition as inferred from the M(H) data discussed above.

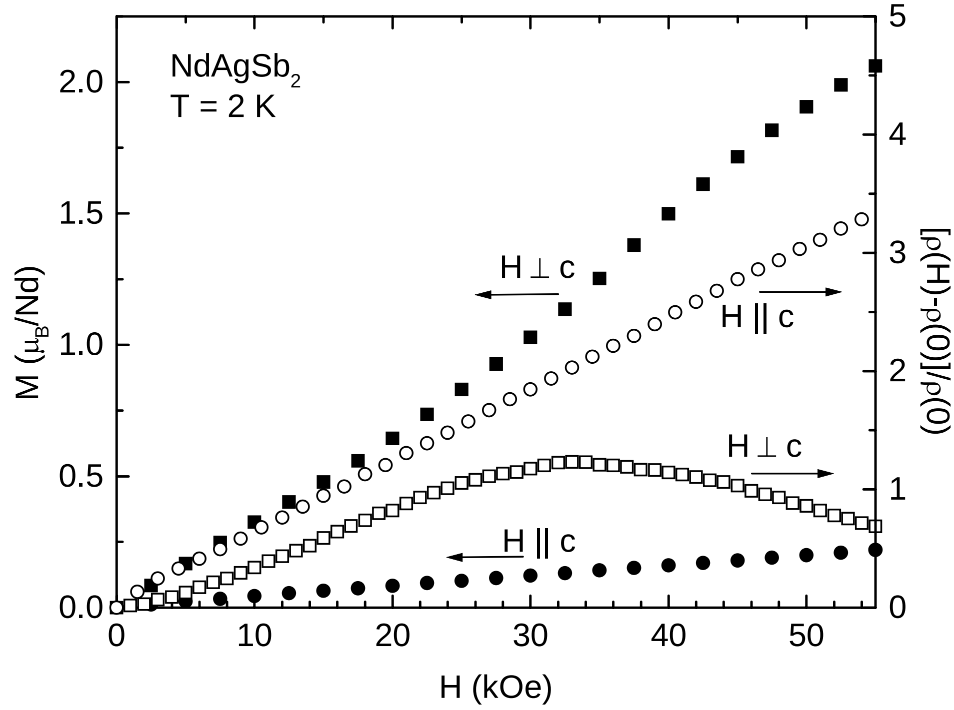

Fig. 4.13 Applied field dependent magnetization (M, left axis) for H || c (●) and H ⊥ c (■) and transverse magnetoresistance ([ρ(H)-ρ(0)]/ρ(0), right axis) for H || c (○) and H ⊥ c (□) of $HoAgSb_2$ at 2 K.

2.12.6. $SmAgSb_2$

Magnetic ordering in $SmAgSb_2$ is observed below 8.6 K [inset, Fig. 4.14(a)], as determined by the local maximum in $d(\chi T)/dT$. Below this temperature, the magnetization decreases for $H \parallel c$, but for $H \perp c$, the magnetization increases below a local minimum 7.5 K. A maximum observed in $d\rho/dt$ at 8.8 K is consistent with T_N determined from M(T). Below T_N, the zero field resistivity decreases sharply by about 0.65 μΩ cm to 0.13 μΩ cm at 2 K [top inset, Fig. 4.14(b)], consistent with a loss of spin-disorder scattering. In a field of 55 kOe perpendicular to the c-axis, the planar resistivity decreases from 1.87 to 1.52 μΩ cm. When a 55 kOe field is applied parallel to the c-axis, the resistivity increases below the magnetic ordering temperature from 3.0 μΩ cm to 8.7 μΩ cm, which will be discussed in detail in Section 4.3.6.

At higher temperatures, the inverse susceptibility of $SmAgSb_2$ [Fig. 4.14 (a)] is non-linear for both $H \parallel c$ and $H \perp c$ and tends to become temperature independent at high temperatures. This behavior is typical in Sm containing compounds, since the first excited state of the Hund's rule multiplet ($J = 7/2$) is very close to the ground state ($J = 5/2$). The high temperature resistivity [Fig. 4.14(b)] is typical of intermetallic compounds. The unusually large RRR $\approx$ 200 and very small residual resistivity $\rho(H=0,T=1.8\ K) \approx 0.125$ μΩcm indicate very small impurity and dislocation densities.

There are two major features to note in the magnetization as a function of applied field at 2 K (Fig. 4.15). First, M(H) is remarkably small even at high fields and is anisotropic with a much greater response for $H \perp c$ [$M(55\ kOe) \approx 0.015\ \mu_B/Sm$] relative to M(H) for $H \parallel c$. Second, de Haas-van Alphen oscillations are very clearly observed for $H \parallel c$. An initial

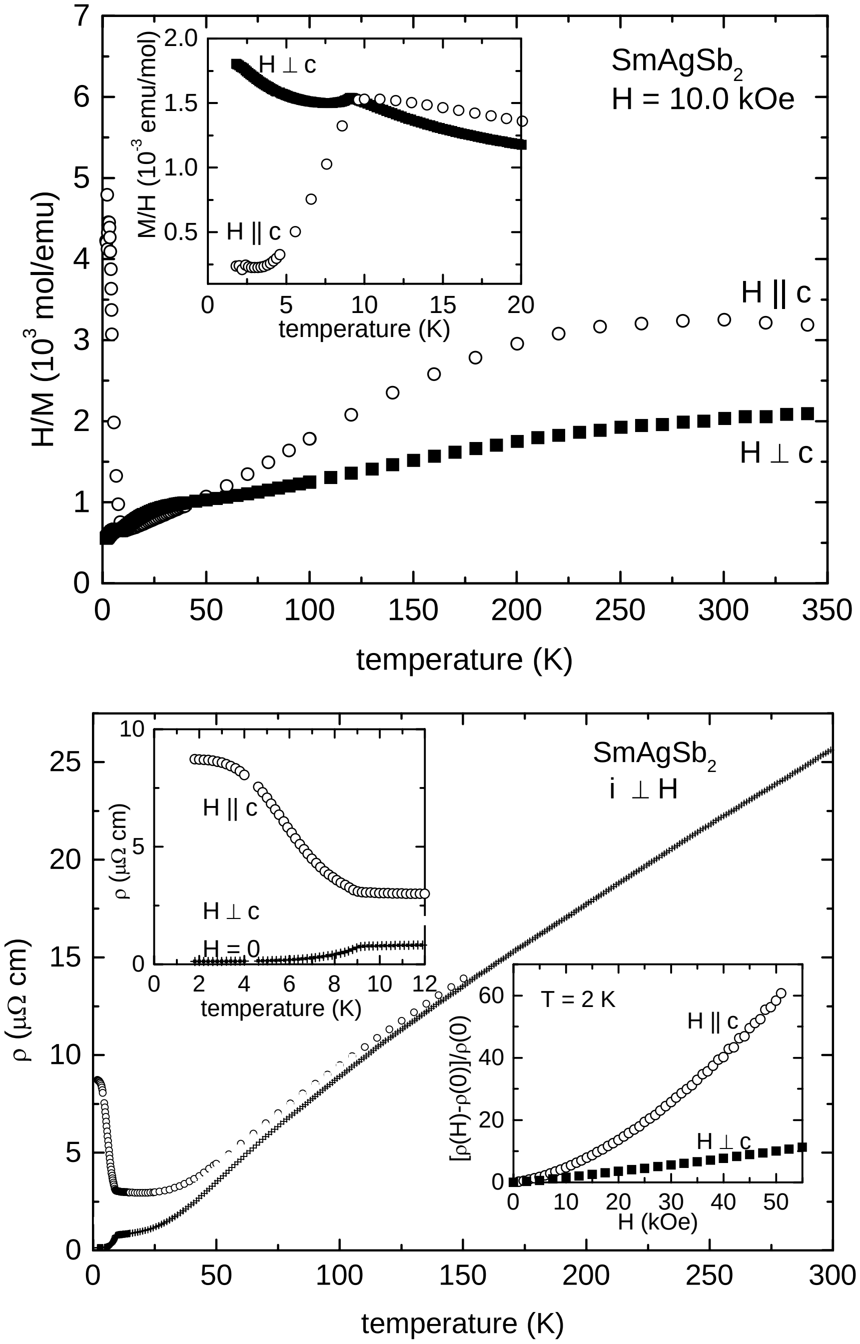

Fig. 4.14 (a) Temperature-dependent inverse susceptibility (M/H) of SmAgSb$_2$ in an applied field of 10 kOe for H || c (○), H ⊥ c (■), and the polycrystalline average (solid line). Inset: expanded view of M/H for low temperatures, showing the magnetic transition at 8.8 K. (b) Temperature-dependent resistivity of SmAgSb$_2$ in zero field (+), and in 55 kOe for H || c (○) and H ⊥ c (■). Top inset: detail of resistivity below 10 K. Bottom inset: transverse magnetoresistance at 2 K for H || c (○) and H ⊥ c (■).

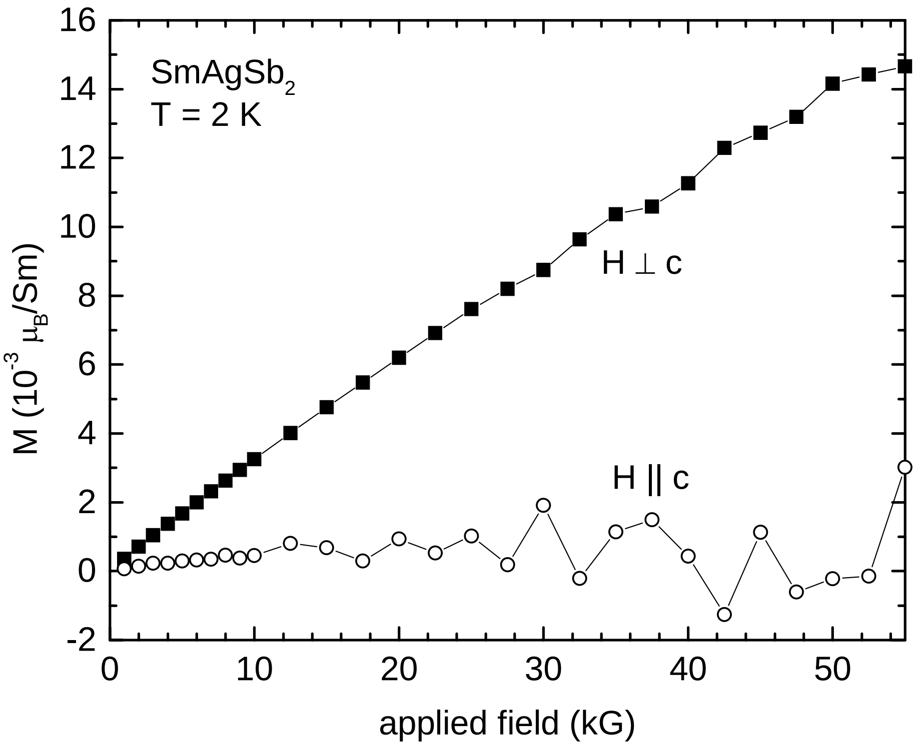

Fig. 4.15 Magnetization (M) versus applied field (H) of $SmAgSb_2$ for H || c (○) and H ⊥c (■) at 2 K. Note the de Haas-van Alphen oscillations present for H || c.

analysis of these oscillations yields frequencies of 0.52 MOe, 0.55 MOe, 0.84 MOe, and 0.89 MOe. A full review of the de Haas-van Alphen oscillations will be the subject of Chapter 6.

The anisotropic behavior in the transverse magnetoresistance at 2 K can be seen in the bottom inset of Fig. 4.14 (b). The magnetoresistance is positive and proportional to $H^{1.6}$ for H || c and $H^{1.1}$ for H ⊥ c. In both cases there are no signs of saturation at high fields. At the maximum obtainable field of 55 kOe, [ρ(H=55kOe)–ρ(0)]/ρ(0) is over 60 and 10 for H || c and H ⊥ c, respectively.

2.12.7. $GdAgSb_2$

Figure 4.16 (a) displays the inverse susceptibility of $GdAgSb_2$ in an applied field of 1.0 kOe, with the low temperature susceptibility expanded in the inset. For both the axial and planar orientations of the applied field, a sharp maximum in $d(\chi T)/dT$ corresponds to an ordering temperature of 12.8 K. Below this transition temperature, the susceptibility decreases for $H \perp c$ and remains nearly constant for $H \parallel c$, typical for antiferromagnetic ordering with no CEF anisotropy and the moments perpendicular to the c-axis. Above T_N, the inverse susceptibility of $GdAgSb_2$ is isotropic and linear, yielding an effective moment of 7.9 μ_B/Gd. The Weiss paramagnetic temperature is -32.0 K for both orientations of the field, consistent with no crystal field splitting of the isotropic Gd^{3+} ion and antiferromagnetic ordering.

The magnetic transition is also revealed in the resistivity as a function of temperature with a peak in $d\rho/dT$ at 12.8 K coinciding with the transition determined from M(T). Below T_N, a sharp decrease in the resistivity in zero field [inset Fig. 4.16(b)] is attributed to a loss of spin-disorder scattering associated with a paramagnetic-antiferromagnetic transition. Although an application of a 55 kOe field parallel to the c-axis apparently suppresses this low-temperature loss of resistivity, the transition is still observed at 12.8 K in M(T, H=55 kOe) data [lower inset, Fig. 4.16 (a)]. Most likely, this apparent suppression is the result of a large electronic contribution to the transverse magnetoresistance, offsetting the loss of spin disorder scattering, which will be discussed in Section 4.3.6. At higher temperatures, the

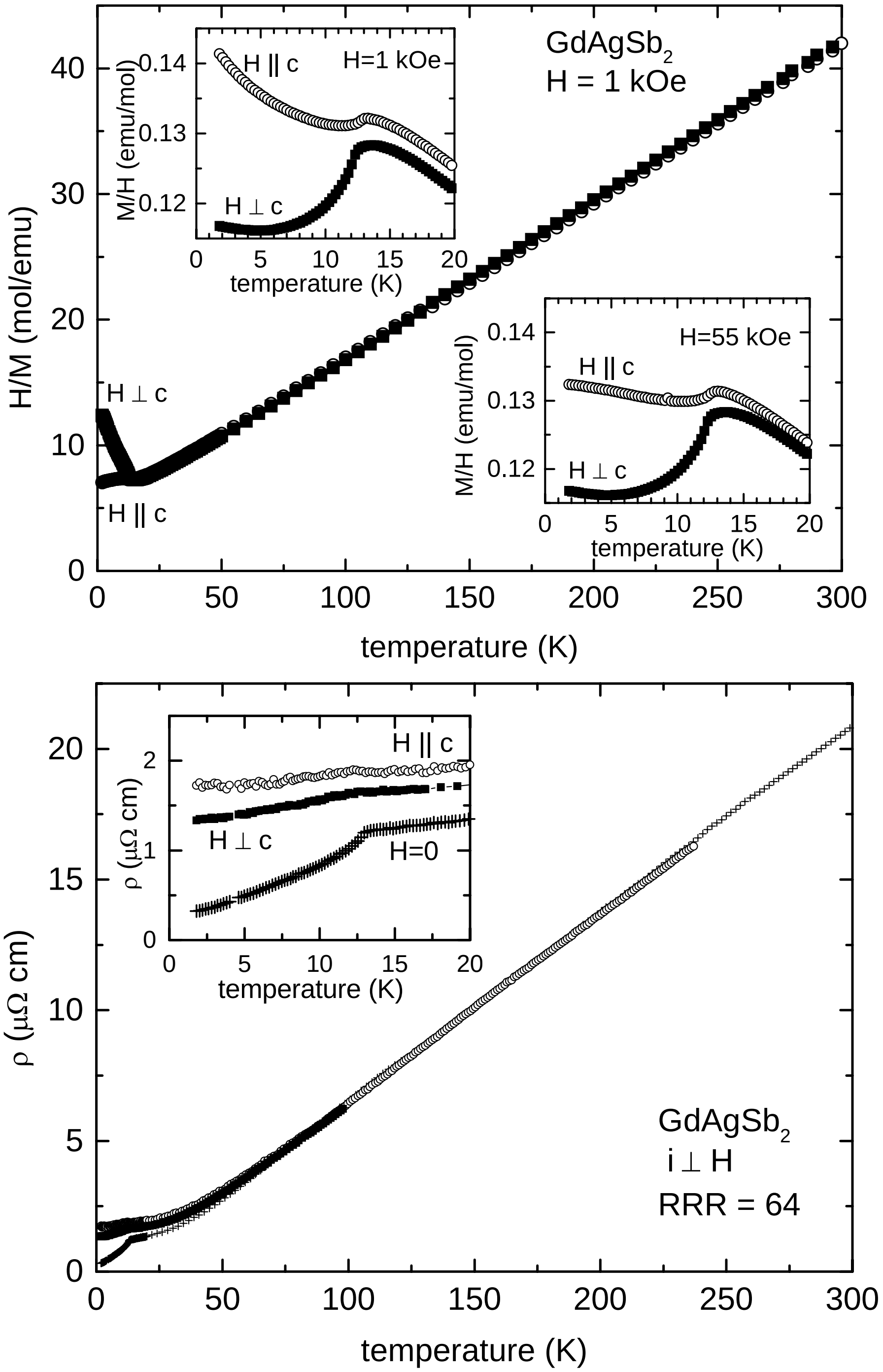

Fig. 4.16 (a) Temperature-dependent inverse susceptibility (M/H) of GdAgSb$_2$ in an applied field of 1 kOe for H || c (○), H ⊥ c (■), and the polycrystalline average (solid line). Inset: expanded view of M/H for low temperatures, showing the magnetic transition at 12.8 K. (b) Temperature-dependent resistivity of GdAgSb$_2$ in zero field (+), and in 55 kOe for H || c (○) and H ⊥ c (■). Inset: detail of resistivity below 20 K.

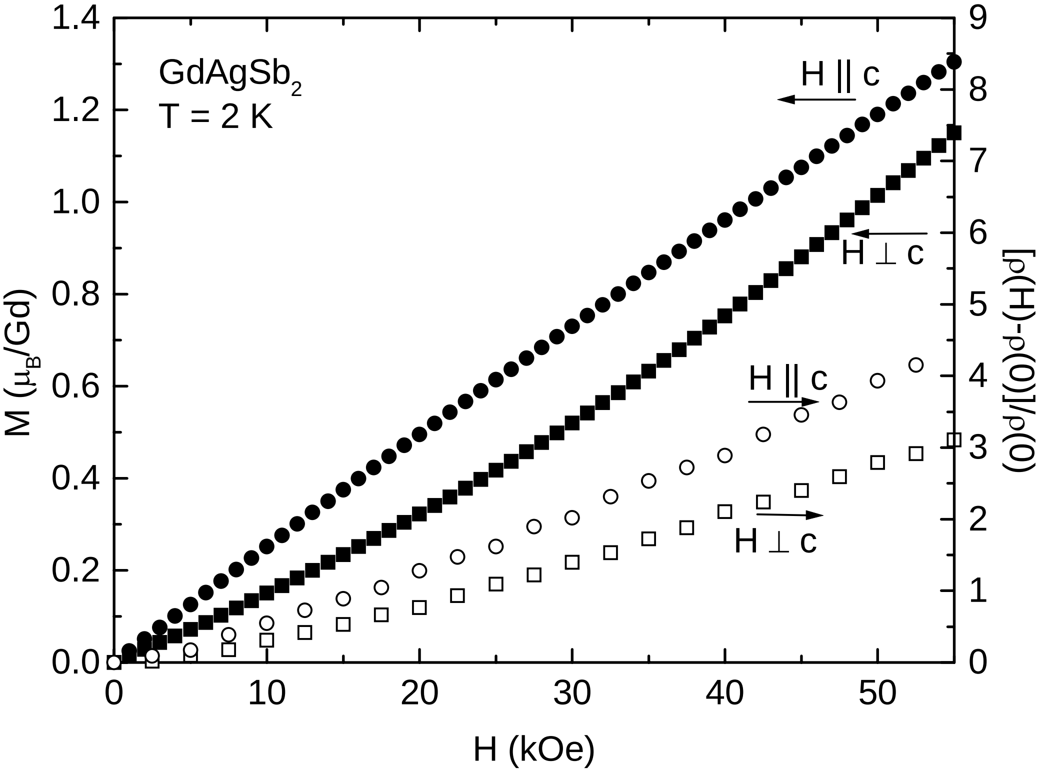

Fig. 4.17 Applied field dependent magnetization (M, left axis) for H || c (●) and H ⊥ c (■) and transverse magnetoresistance ([ρ(H)-ρ(0)]/ρ(0), right axis) for H || c (○) and H ⊥ c (□) of GdAgSb$_2$ at 2 K.

resistance is linear, common to the majority of the RAgSb$_2$ series. Likewise, low impurity concentrations are indicated by the large RRR of 65 and low residual resistance of 0.32 μΩ cm at 1.8 K.

At 2 K, the magnetization (Fig. 4.17) is linear and nearly isotropic up to applied fields of 55 kOe, reaching 1.4 μ_B /Gd, far below the theoretical saturated value of 7 μ_B /Gd for a free Gd^{3+} ion. No metamagnetic transitions are observed, which is consistent with the high-field M(T) data. The transverse magnetoresistance of GdAgSb$_2$ at 2 K is large and anisotropic (Fig. 4.17) with a maximum $\Delta\rho(H)/\rho(0)$ at 55 kOe of over 4 for H || c, and over 3 for H ⊥ c.

2.12.8. $TbAgSb_2$

The magnetic properties of $TbAgSb_2$ are strongly anisotropic, with the local Tb^{3+} moments constrained to the basal plane at low temperatures. This is particularly evident in the anisotropic Weiss temperatures, θ_c = -125 K and θ_{ab} = -19 K obtained from fitting the inverse susceptibilities [Fig. 4.18 (a)] to the Curie-Weiss law. The polycrystalline average of the inverse susceptibility gives an effective moment of 10.2 μ_B/Tb, larger than the expected effective moment of 9.72 μ_B for the free Tb^{3+}, and θ_{ave} = –41.4 K, consistent with antiferromagnetic exchange interactions. Below 11.0 K, as determined by the maximum in $d(\chi T)/dT$ [inset, Fig. 4.18 (a)], or 10.9 K from the maximum in $d\rho/dT$ [inset, Fig. 4.18 (b)], $TbAgSb_2$ orders magnetically. For $H \perp c$, the magnetization decreases with decreasing temperature below $T_{N.}$ Although no feature corresponding to the ordering is observed in the low-field magnetization for $H \parallel c$, a broad peak in the magnetization is centered at 70 K, consistent with a strongly anisotropic CEF.

The resistivity as a function of temperature [Fig. 4.18 (b)] in zero field is typical of intermetallic compounds with low-temperature magnetic ordering. At high temperatures, the resistivity increases nearly linearly. The RRR is 53, indicative of very low impurity and dislocation concentrations. Below 10.9 K [inset Fig. 4.18(b)], there is a clear loss of spin-disorder scattering, corresponding to the paramagnetic-antiferromagnetic transition. However, for H = 55 kOe perpendicular to the c-axis, this transition appears to move down to 9.5 K. For $H \parallel c$, the transverse magnetoresistance increases with decreasing temperature as in many of the other members of the $RAgSb_2$ series.

The magnetization as a function of applied field (Fig. 4.19) is strongly anisotropic at 1.8 K. For $H \parallel c$, the magnetization increases nearly linearly, reaching a maximum of only

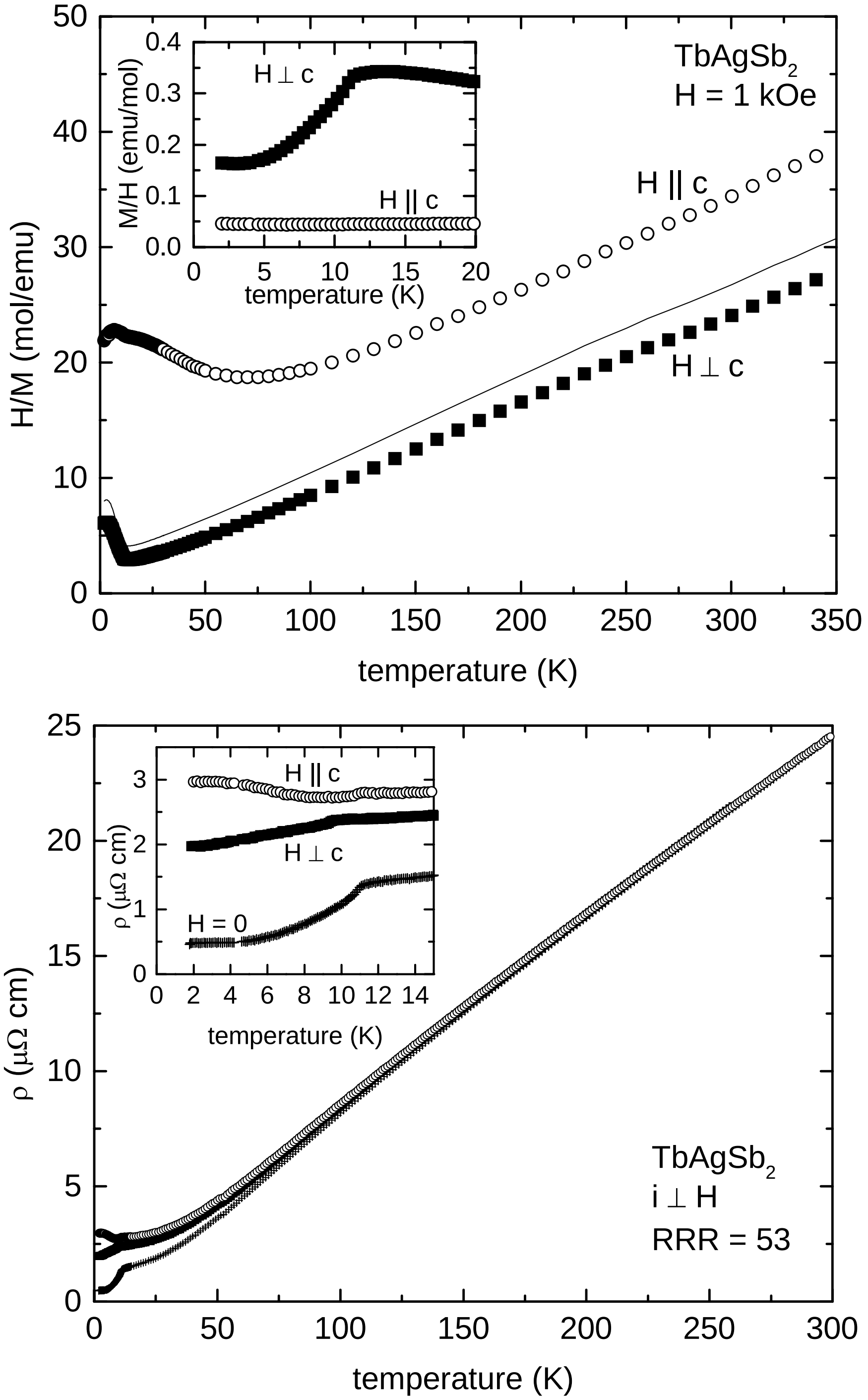

Fig. 4.18 (a) Temperature-dependent inverse susceptibility (M/H) of TbAgSb$_2$ in an applied field of 1 kOe for H || c (○), H ⊥ c (■), and the polycrystalline average (solid line). Inset: expanded view of M/H for low temperatures, showing the magnetic transition at 11.0 K. (b) Temperature-dependent resistivity of TbAgSb$_2$ in zero field (+), and in 55 kOe for H || c (○) and H ⊥ c (■). Inset: detail of resistivity below 20 K.

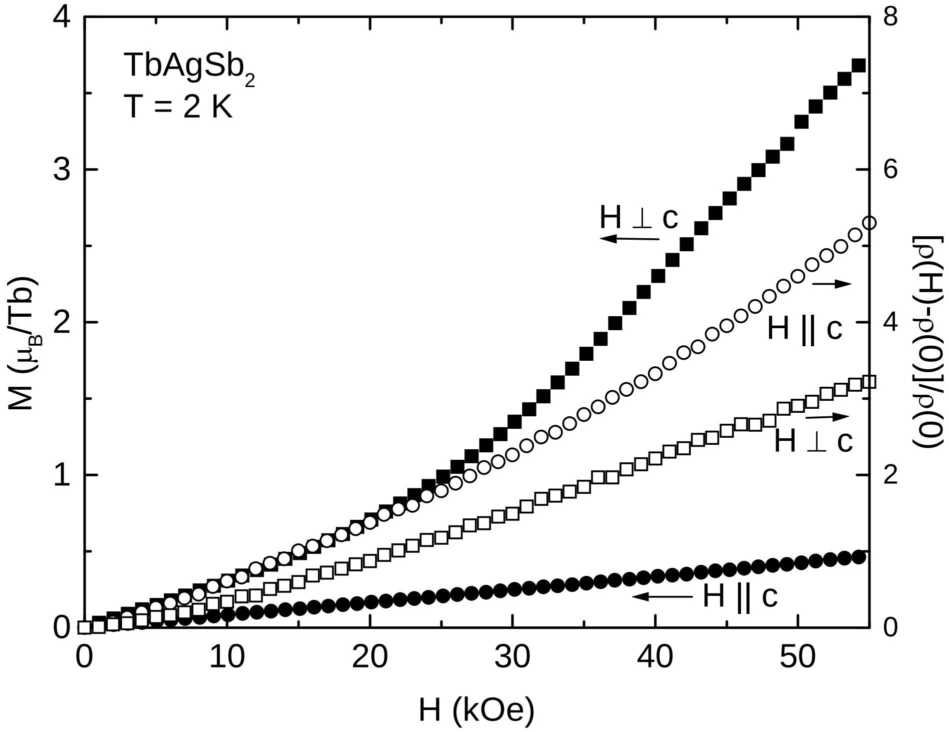

Fig. 4.19 Applied field dependent magnetization (M, left axis) for H || c (●) and H ⊥ c (■) and transverse magnetoresistance ([ρ(H)-ρ(0)]/ρ(0), right axis) for H || c (○) and H ⊥ c (□) of TbAgSb$_2$ at 2 K.

of only 0.5 μ_B/Tb at 55 kOe. However, for H ⊥ c, a much greater and non-linear response is observed, with an upward curvature in slope for H≈30 kOe, which suggests the existence of at least one high-field metamagnetic transition. At 55 kOe, the magnetization only reaches 3.7 μ_B/Tb, less than half the expected saturated moment of a free Tb^{3+} ion of 9 μ_B. The transverse magnetoresistance at 2 K (Fig. 4.19) is super-linear [$\Delta\rho(H)/\rho(0) \propto H^{1.3}$] for both H || c and H ⊥ c, with a larger response for the former case. At 55 kOe, $\Delta\rho(H)/\rho(0)$ reaches 5.4 for H || c and 3.2 for H ⊥ c. Finally, a weak inflection point is present in the magnetoresistance for H ⊥ c near 30 kOe, coinciding with the proposed metamagnetic transition observed in the 2 K magnetization isotherm.

2.12.9. DyAgSb$_2$

The temperature-dependent susceptibility of DyAgSb$_2$ is also strongly anisotropic, with the moments constrained to the basal plane, as shown by the inverse susceptibility [Fig. 4.20 (a)]. Above 100 K, the inverse susceptibilities are linear, with $\mu_{eff\,=}$ 10.3 μ_B /Dy and θ_{ave} = –10.1 K. The anisotropic Weiss temperatures are θ_c = –86.3 K and θ_{ab} = 7.1 K.

For a 1.0 kOe field applied perpendicular to the c-axis, magnetic ordering is observed below 9.4 K [inset Fig 4.20 (a)], determined from the a peak in $d(\chi T)/dT$. The zero-field resistivity confirms the ordering temperature with a local maximum in $d\rho/dt$ at 9.4 K. Below T_N [inset Fig. 4.20 (b)], a decrease in the resistivity corresponds to the loss of spin-disorder scattering as the Dy^{3+} moments become antiferromagnetically ordered. For H = 55 kOe parallel to the c-axis, a sharp decrease in magnetoresistance is observed below T_N. However, at even lower temperatures, the magnetoresistance increases similarly to that observed in the compounds with R = Nd, Sm, Gd, and Tb, which will be analyzed later. For H= 55 kOe, perpendicular to the c-axis, the decrease in the resistivity at low temperatures is smooth, which is typical of the Brillouin saturation in the saturated paramagnetic state. This data agrees with the previously published temperature-applied field phase diagrams (Myers, 1999). At higher temperatures, the resistivity [Fig. 4.20(b)] again shows the metallic behavior common to the rest of the series, with a large RRR [ρ(300 K]/ρ(1.8 K) ≈ 40], suggesting good sample quality. Exceptionally clear metamagnetism is evident in the 2 K M(H) and ρ(H) data, as seen in Figure 4.21 (a). For H $\parallel$ c, the magnetization increases linearly to 1.8 μ_B/Dy at 55 kOe. However, for H $\perp$c, a series of sharp steps occur, with both

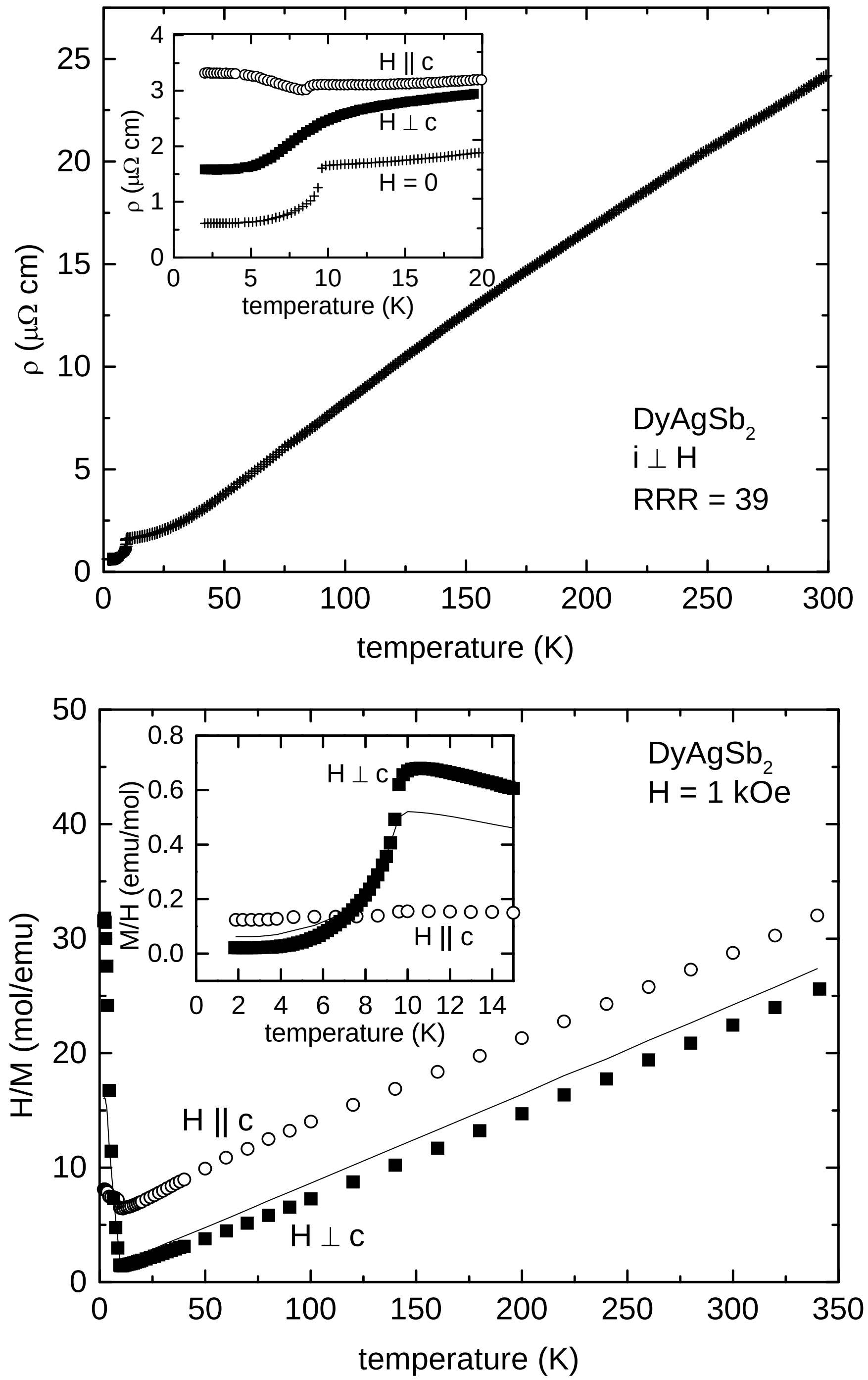

Fig. 4.20 (a) Temperature-dependent inverse susceptibility (M/H) of DyAgSb$_2$ in an applied field of 1 kOe for H || c (○), H ⊥ c (■), and the polycrystalline average (solid line). Inset: expanded view of M/H for low temperatures, showing the magnetic transition at 9.0 K. (b) Temperature-dependent resistivity of DyAgSb$_2$. Inset: detail of resistivity below 20 K for zero field (+), and for 55 kOe for H || c (○) and H ⊥ c (■)

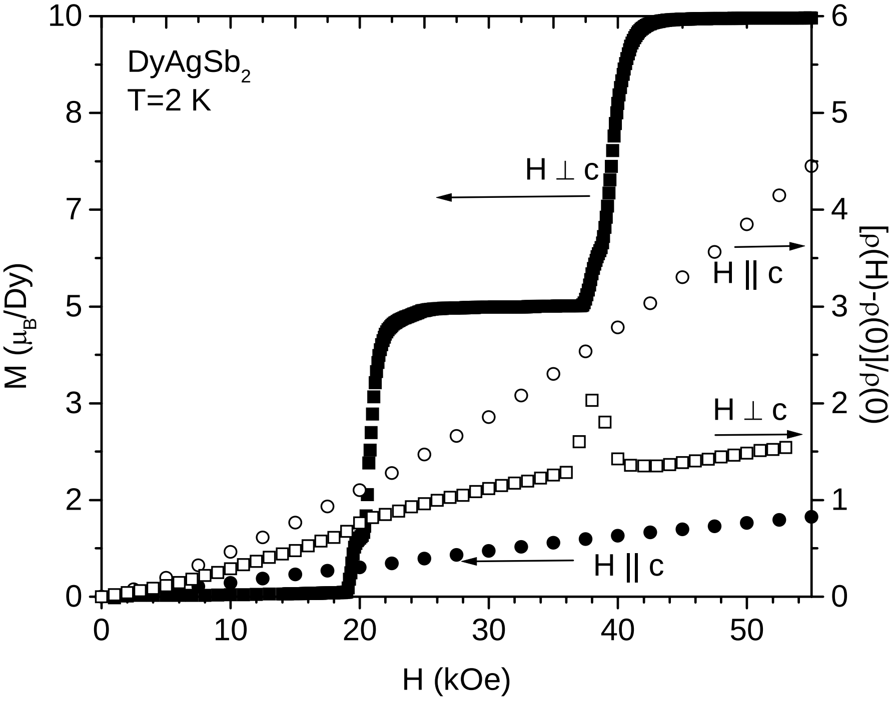

Fig. 4.21 Applied field dependent magnetization (M, left axis) for H || c (●) and H ⊥ c (■) and transverse magnetoresistance ([ρ(H)-ρ(0)]/ρ(0), right axis) for H || c (O) and H ⊥ c (☐) of DyAgSb$_2$ at 2 K. (b) Magnetization (M) as a function of applied field (H) for 5 different orientations within the basal plane of DyAgSb$_2$: 0° or [110] (■), 15° (O), 22° (*), 30° (D), and 45° or [100] (+). Angles are relative to the [110] axis.

the transition field and plateau magnetization dependent on the orientation of the magnetic field within the basal plane, as seen in Fig. 4.21(b). The maximum magnetization measured was 10.1 μ_B/Dy for $\theta = 0^o$ (along the [110] axis), which is consistent with the saturated moment of the free Dy^{3+} ion. However, for H parallel to the [100] axis, the maximum saturated magnetization is only about 7 μ_B/Dy at 55 kOe, suggesting the presence of strong CEF-induced anisotropy within the basal plane. A full analysis of the angular dependence of the planar metamagnetism in $DyAgSb_2$ is presented in Chapter 5.

At 2 K, the transverse magnetoresistance [Fig. 4.21(a)] is large and very anisotropic in the same manner as that seen in other members of the series. For $H \perp c$, the magnetoresistance is highly non-monotonic with a break in the slope at the lower metamagnetic transition and a sharp local maximum at the higher transition. Applying a field in the basal plane ($H \perp c$) yields a $\Delta\rho(H)/\rho(0)$ of 1.5 at 55 kOe, with anomalous behavior between 18 and 40 kOe, typical of metamagnetic transitions. With an axial orientation of the field ($H \parallel c$), $\Delta\rho(H)/\rho(0)$ increases to 4.5 at 55 kOe.

2.12.10. HoAgSb$_2$

Like the majority of the $RAgSb_2$ series, $HoAgSb_2$ is strongly anisotropic and antiferromagnetically ordered at low temperatures [inset Fig. 4.22(a)]. The temperature of the magnetic transition, determined from the maximum in $d(\chi T)/dT$ at 5.4 K, is in good agreement with the maximum in $d\rho/dt$ at 5.3 K [inset Fig. 4.22 (b)]. Throughout the whole temperature range, the axial susceptibility is diminished relative to the planar susceptibility, indicating a preference for the moments to align within the basal plane. The polycrystalline average of the inverse susceptibility may be fit to the Curie-Weiss law [Fig 4.22 (a)],

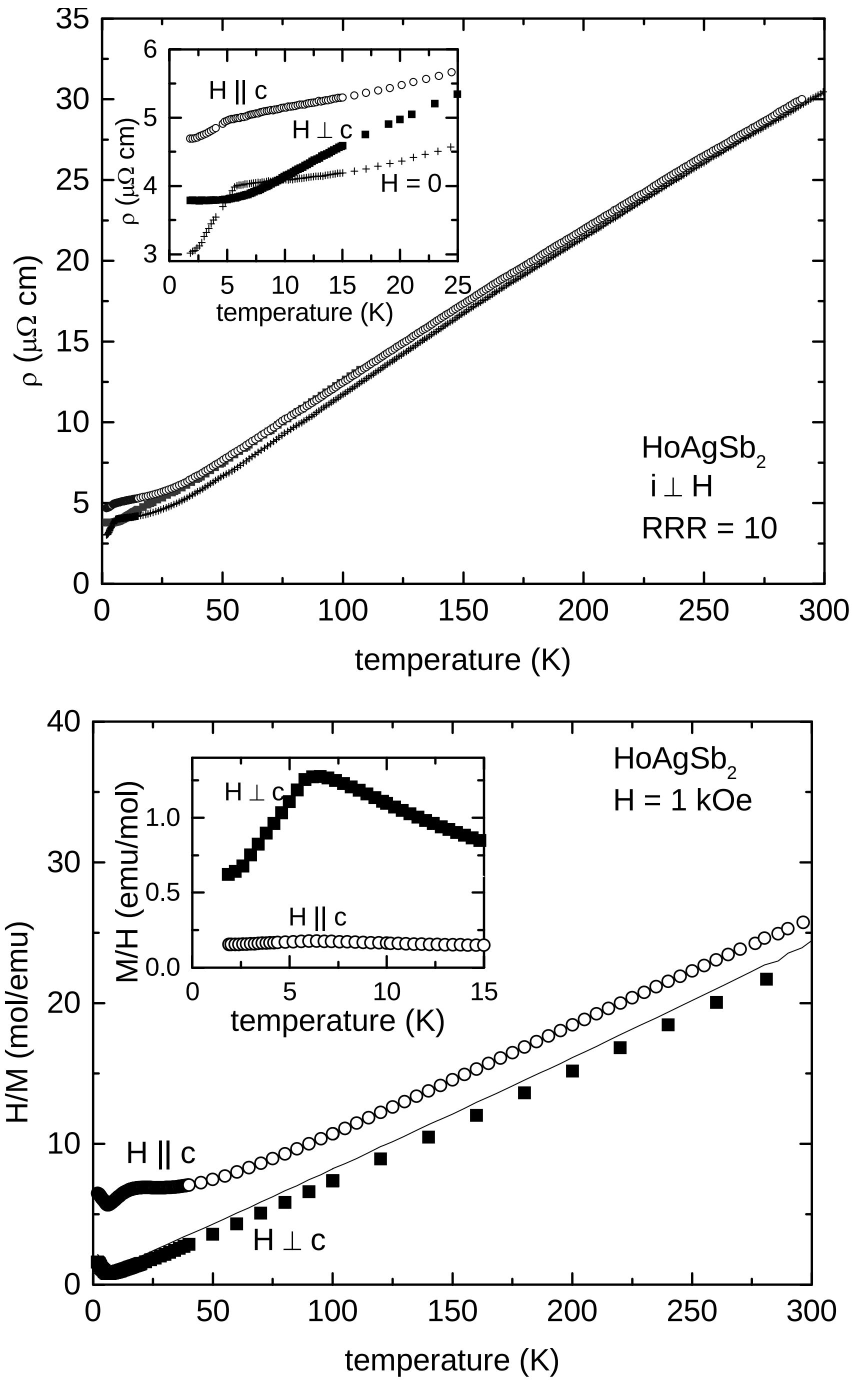

Fig. 4.22 (a) Temperature-dependent inverse susceptibility (M/H) of $HoAgSb_2$ in an applied field of 1 kOe for H || c (○), H ⊥ c (■), and the polycrystalline average (solid line). Inset: expanded view of M/H for low temperatures, showing the magnetic transition at 5.4 K. (b) Temperature-dependent resistivity of $HoAgSb_2$ in zero field (+), and in 55 kOe for H || c (○) and H ⊥ c (■). Inset: detail of resistivity below 25 K.

yielding μ_{eff} =10.1 μ_B/Ho and θ_{ave} = –1.7 K. Anisotropic Weiss temperatures are θ_c = –39.5 K and θ_{ab} = 9.2 K.

Overall, the resistivity of $HoAgSb_2$ [Fig. 4.22 (b)] suggests good sample quality with a RRR of about 10. The high temperature resistivity is typical of intermetallic compounds, increasing linearly up to 300 K, with no signs of saturation. At low temperatures, the zero-field resistivity as a function of temperature [inset Fig. 4.22(b)] shows a clear loss of spin disorder scattering below 5.3 K, with a decrease in the resistivity of about 1 $\mu\Omega$ cm from the paramagnetic state to the antiferromagnetic state. In 55 kOe for H $\perp$ c, the resistivity smoothly decreases, typical of a Brillouin saturation of magnetic moments and agrees with M(H,T = 2 K) for H $\perp$ c, which also suggests that at 55 kOe, $HoAgSb_2$ is a saturated paramagnet. Likewise, above T_N, the transverse magnetoresistance becomes negative, the result of decreased scattering due to the near saturation of the Ho^{3+} in the paramagnetic state. For H || c, the loss of spin disorder scattering is still observed, since the applied field is not as strongly coupling to the Ho^{3+} moments, which reside in the basal plane.

Although not as well defined as for $DyAgSb_2$, planar metamagnetism is observed in $HoAgSb_2$ at 2 K, as seen in Fig. 4.23. The magnetization of the compound increases linearly for H || c, only reaching about 2 μ_B/Ho at 55 kOe. Likewise, the transverse magnetoresistance (Fig. 4.23) for H || c is nearly linear. However, more complicated behavior is observed for H $\perp$ c, where the magnetization exhibits a positive curvature below 16 kOe and saturates to 8.7 μ_B/Ho above 20 kOe, short of the expected saturated moment of a free Ho^{3+} ion of 10 μ_B. A broad peak at 14 kOe in the 2 K transverse magnetoresistance coincides with the observed transition in M(H).

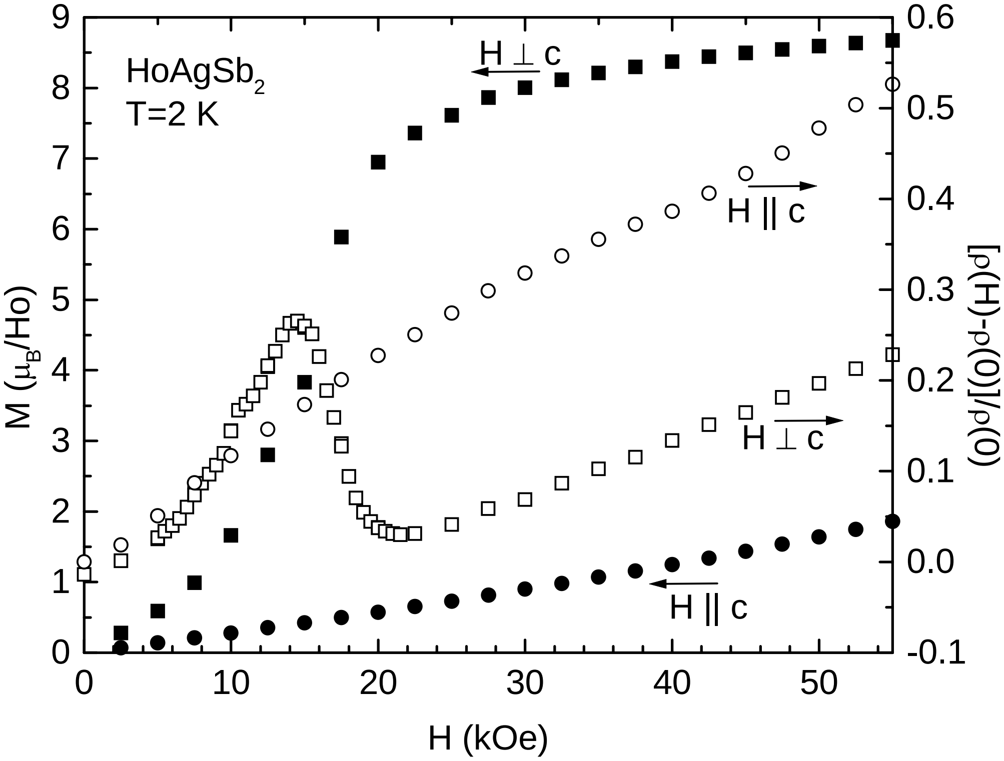

Fig. 4.23 Applied field dependent magnetization (M, left axis) for H || c (●) and H ⊥ c (■) and transverse magnetoresistance ([ρ(H)-ρ(0)]/ρ(0), right axis) for H || c (○) and H ⊥ c (□) of HoAgSb$_2$ at 2 K.

2.12.11. ErAgSb$_2$ and TmAgSb$_2$

As previously discussed, the flux growth of single crystals of the RAgSb$_2$ series of compounds becomes very difficult as the rare earth ions become heavier and smaller. Consequently, the uncertainty in the measured effective moments increases due to the small size of the crystals obtained for these compounds. Along with the smaller sample yield, the quality of the crystals decreases for the compounds. This is reflected in the residual resistivity of ErAgSb$_2$ (Fig. 4.24), which is much larger [ρ(1.8 K) = 3.86 μΩ cm] than the other members of the series [ρ(1.8 K) = 0.13 μΩ cm in SmAgSb$_2$), possibly due to increased impurity and defect scattering inherent in the samples. Likewise, the RRR [ρ(300 K)/ρ(1.8

K) ≈ 5] is smaller than the other samples measured. Finally, the small size of the $TmAgSb_2$ crystals precludes reliable measurements of resistivity.

Unlike the rest of the $RAgSb_2$ series of compounds, the CEF splittings of the Hund's rule ground state constrain the local rare earth moments to align parallel to the c-axis in $ErAgSb_2$ and $TmAgSb_2$. At high temperatures, $ErAgSb_2$ and $TmAgSb_2$ are Curie-Weiss paramagnets. In $ErAgSb_2$ [Fig. 4.25 (a)], the inverse of the polycrystalline average of the susceptibility gives $\mu_{eff} = 9.1\ \mu_B$/Er and $\theta_{ave} = -2.2$ K. Anisotropic inverse susceptibilities yield Weiss paramagnet temperatures of $\theta_c = 9.8$ K and $\theta_{ab} = -14.6$ K, consistent with antiferromagnetic interactions and an easy axis. The temperature dependent magnetization of $TmAgSb_2$ [Fig. 4.25 (b)] is similar to that of $ErAgSb_2$ with anisotropic Weiss temperatures of

Fig. 4.24 Temperature-dependent resistivity of $ErAgSb_2$ in zero field (+), and in 55 kOe for $H \parallel c$ (○) and $H \perp c$ (■). Inset: detail of resistivity below 8 K.

θ_c = 53 K and θ_{ab} = -44 K. The polycrystalline average of the M(T)data yields a Weiss temperature of θ_{ave} = 0.9 K, and an effective moment of 6.55 μ_B/Tm, considerably smaller than the expected theoretical value of the free Tm^{3+} moment of 7.56 μ_B.

Low-temperature magnetic ordering is observed or inferred in both compounds. Specifically, $ErAgSb_2$ is antiferromagnetic with T_N = 3.9 K, determined from the maximum in $d(\chi T)/dT$. A clear loss of spin disorder scattering is also observed in the resistivity of $ErAgSb_2$ [inset Fig. 4.24] below 4.1 K in zero applied field. A peak in $d\rho/dt$ at 3.8 K indicates magnetic ordering and is consistent with the M(T) data. However, no loss of spin disorder scattering is observed in the 55 kOe for either $H \parallel c$ or $H \perp c$ orientations of the field in $ErAgSb_2$. The ordering temperature of $TmAgSb_2$ is smaller than for $ErAgSb_2$. Although no peak is present in $d(\chi T)/dT$ of $TmAgSb_2$ down to 1.8 K, the M(T) data [inset, Fig. 4.25 (b)] suggest an ordering temperature near 1.8 K.

The nature of the magnetic order at low temperature may be seen in the magnetization isotherms at 1.8 K. The magnetization of both compounds increases linearly for $H \perp c$, reaching 1.7 μ_B/Er [Fig. 4.26(a)] and 1.1 μ_B/Tm [Fig. 4.26(b)] at 55 kOe. For $H \parallel c$, there is a well-defined step in the magnetization in each compound between 5 and 20 kOe. Above 20 kOe the magnetization appears to saturate to 7.8 μ_B/Er and 4.6 μ_B/Tm, below the expected magnetic moments for the accepted theoretical values for the free ions of 9 μ_B/Er and 7 μ_B/Tm. In both compounds, the saturated moment along the easy axis is considerably less than expected. Although this discrepancy could be the result of uncertainty in the mass due to small sample size, scaling the masses to match the accepted values of the Curie-Weiss

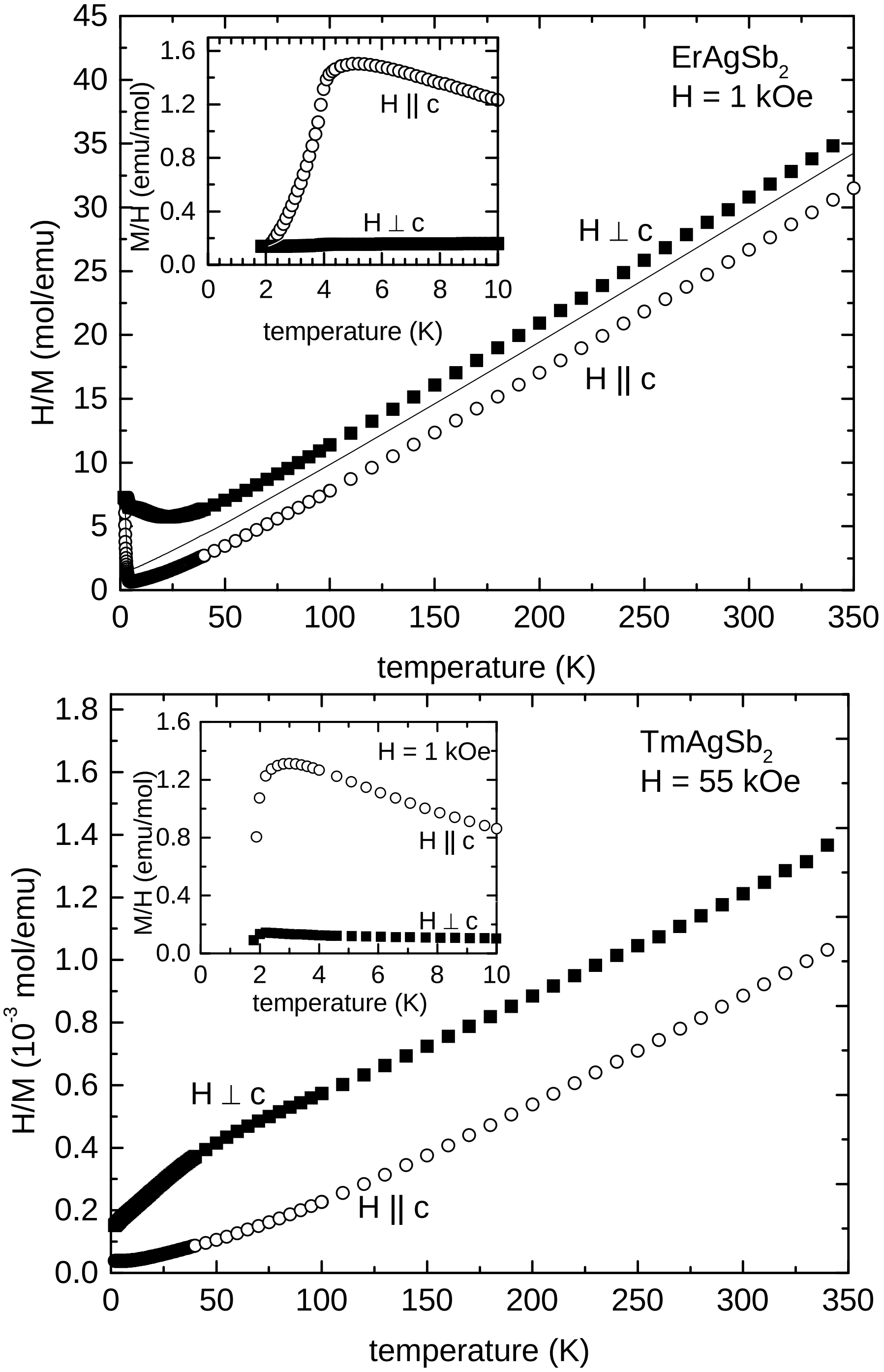

Fig. 4.25 Temperature-dependent inverse susceptibility (M/H) of (a) $ErAgSb_2$ in an applied field of 1 kOe and (b) $TmAgSb_2$ in an applied field of 55 kOe for H || c (○), H ⊥ c (■), and the polycrystalline average (solid line). Insets: expanded views of M/H for low temperatures, showing the magnetic transition at 3.8 K for $ErAgSb_2$ and magnetic ordering below approximately 2 K in $TmAgSb_2$ with H = 1 kOe.

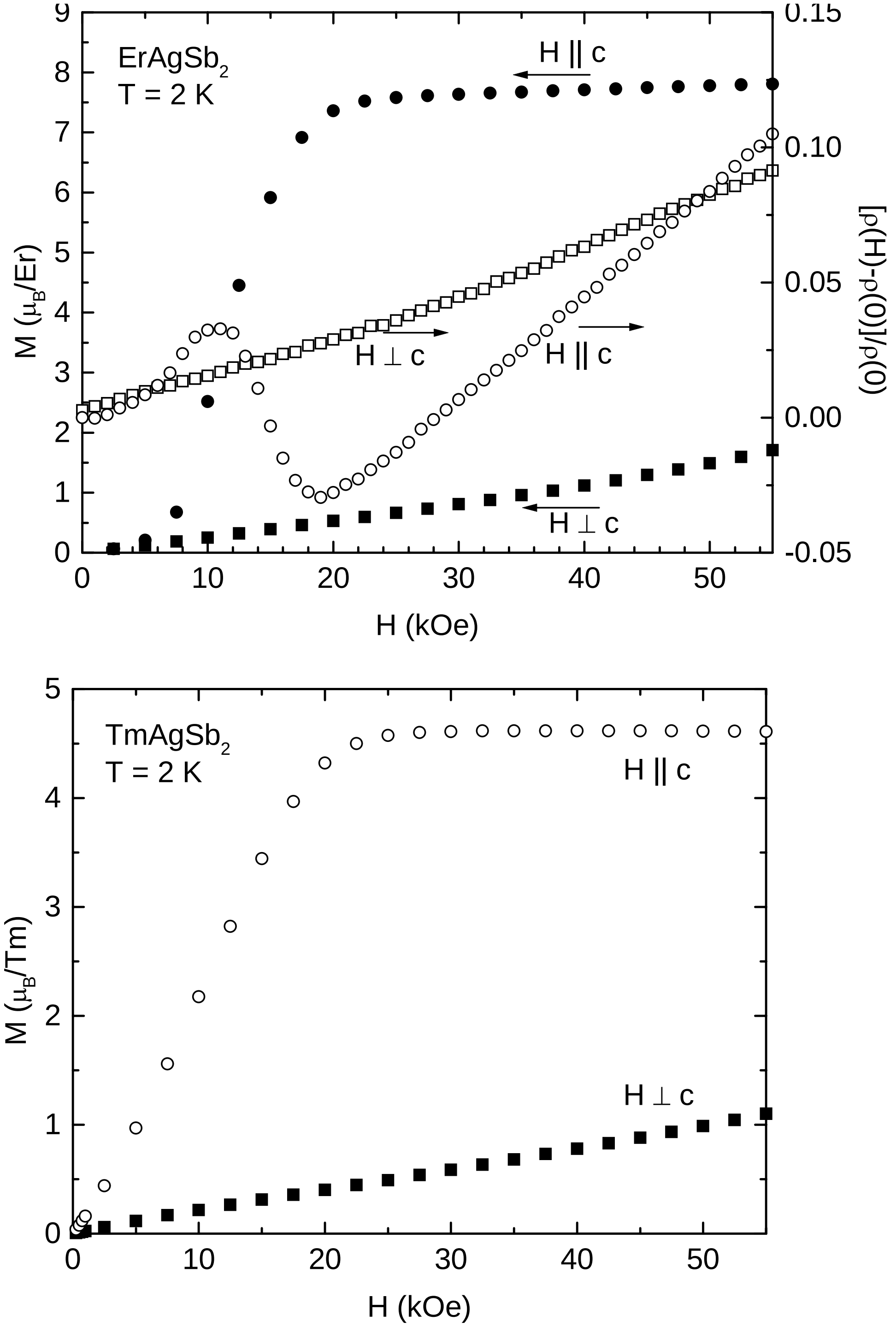

Fig. 4.26 (a) Applied field dependent magnetization (M, left axis) for H || c (●) and H ⊥ c (■) and transverse magnetoresistance ($[\rho(H)-\rho(0)]/\rho(0)$, right axis) for H || c (○) and H ⊥ c (□) of ErAgSb$_2$ at 2 K. (b) Magnetization (M) versus applied field (H) of TmAgSb$_2$ for H || c (○) and H ⊥c (■) at 2 K.

effective moment still produces saturated moments too small to fully account for the difference. It is therefore likely that either the local moments are not aligned perfectly along the c-axis in the ordered state, suggesting a possible conical structure, or a metamagnetic transition exists at higher fields.

The 2 K transverse magnetoresistance of $ErAgSb_2$ [Fig. 4.26(a)] demonstrates characteristic behavior of metamagnetism for H || c. In this case, $\Delta\rho(H)/\rho(0)$ increases to a peak at 11 kOe and then abruptly drops to a minimum at 19 kOe. Above 25 kOe, $\Delta\rho(H)/\rho(0)$ increases linearly up to above 0.10 at the maximum applied field of 55 kOe. The magnetoresistance perpendicular to the direction of the magnetic moments ($H \perp c$) increases monotonically to 0.09 at 55 kOe.

2.13. Discussion

2.13.1. Crystal Electric Field

Throughout the $RAgSb_2$ series of compounds, the magnetic and transport properties are strongly anisotropic due to the CEF splitting of the Hund's rule ground state multiplet. Specifically, for high temperatures, the easy axis for the magnetization in the compounds with R = Ce-Nd, Tb-Ho lies within the basal plane, with $\theta_P^{ab} > \theta_P^{c}$. For R = Er and Tm, this is reversed, with the moments aligning parallel to the c-axis and $\theta_P^{c} > \theta_P^{ab}$.

Analysis of this axial-planar anisotropy allows a determination of the leading term in the crystal field Hamiltonian, using the differences in the paramagnetic temperatures (θ_p^c-θ_p^{ab}). When the rare earth ion is in a location with tetragonal point symmetry, the CEF Hamiltonian may be written as:

$$H_{CEF} = B_2^0 O_2^0 + B_4^0 O_4^0 + B_4^4 O_4^4 + B_6^0 O_6^0 + B_6^4 O_6^4,$$

where the B_n^m are the Stevens coefficients and O_n^m are the Stevens equivalent operators. It has also been shown (Wang, 1971) (Boutron, 1973) that if coupling between the moments is ignored, at high temperatures only the B_2^0 term contributes to the Weiss temperatures giving:

$$\left(\theta_{a,b} - \theta_c\right) = \frac{3(2J-1)(2J+3)}{10} B_2^0$$

The point charge model may be used to predict the sign of B_2^0, where

$$B_2^0 = \left\langle r^2 \right\rangle A_2^0 \alpha_J \, .$$

and by definition, $<r^2>$ is always positive. In the point charge model, A_2^0 is a coefficient in the expansion of the solution of Laplace's equation in spherical harmonics for the electrostatic potential at the rare earth site due to the CEF. Since A_2^0 is purely geometrical, it should remain constant throughout the rare earth series, neglecting the rare earth contraction. The sign of B_2^0 will therefore only depend on the sign of α_J, a rare earth dependent coefficient given in Table 2. Subsequently, the sign of α_J is enough to predict whether the compound will have an easy plane or an easy axis. Table 2 shows the easy orientation is consistent with the point charge model, and lists experimental values of B_2^0 and A_2^0. Note the change in sign of α_J corresponds to the change from easy plane to easy axis between $HoAgSb_2$ and $ErAgSb_2$. Although A_2^0 should be approximately constant throughout the series, the calculated values vary by about 50%. This variation could be due to the simplicity of the point charge model, the result of anisotropy within the basal plane modifying the high temperature susceptibility, or the coupling between the local moments. To test the latter case, samples of $YAgSb_2$ were prepared with a small amount of Dy introduced into the melt. From the Curie-Weiss effective moment, and the saturation magnetization, the concentration

Table 4.1. Magnetic properties of the $RAgSb_2$ compounds. Uncertainties reflect experimental limits and in the case of T_M include any variation between magnetic susceptibility and resistivity data. Crystalline electric field parameters (α_J, $<r^2>$) are from Taylor (1972).

Compound	T_M (K) (±0.1 K)	μ_{eff} (μ_B) (±0.1 K)	θ_{ave} (K) (±0.2 K)	θ_c (K) (±0.2 K)	θ_{ab} (K) (±0.2 K)	B_2^0(K) (±0.3 K)	$<r^2>$ (a_0^2)	$\alpha_J\times10^2$	A_2^0 (±0.3)
$CeAgSb_2$	9.6	2.3	16.8	-27.9	34.6	6.5	1.200	-5.71	-1.0
$PrAgSb_2$	2.8	3.6	-7.2	-48.5	-6.3	1.8	1.086	-1.05	-1.6
$NdAgSb_2$	2.9	3.6	-14.2	-45.3	-4.0	1.4	1.001	-0.643	-2.2
$SmAgSb_2$	8.7	-	-	-	-	-	0.883	4.13	-
$GdAgSb_2$	12.8	7.9	-32.0	-32.0	-32.0	-	-	-	-
$TbAgSb_2$	11.0	10.2	-41.4	-125	-19.0	2.1	0.758	-1.01	-2.8
$DyAgSb_2$	9.4	10.3	-10.1	-86.3	7.1	1.2	0.726	-0.635	-2.7
$HoAgSb_2$	5.4	10.1	-1.7	-39.5	9.2	0.6	0.695	-0.222	-3.7
$ErAgSb_2$	3.8	9.1	-2.2	9.8	-14.6	-0.3	0.666	0.254	-1.9
$TmAgSb_2$	~1.8	6.6	0.9±0.5	53±0.5	-44±0.5	-1.9±0.7	0.640	1.01	-3.0±0.7

was found to be $Dy_{0.07}Y_{0.93}AgSb_2$. From the high-temperature inverse susceptibility (Fig. 4.27), the Weiss paramagnetic temperatures were found to be θ_p^c = -87.9 and θ_p^{ab} = 22.0 K, giving a value of B_2^0 for the dilute compound of 1.45 K, compared to the value found for $DyAgSb_2$ of 1.23 K, a difference of 18%. This suggests that the coupling between the local moments may significantly affect the magnetization at high temperatures and indicates that similar dilutions for each R are required for more accurate determinations of B_2^0 in the rest of the $RAgSb_2$ compounds.

2.13.2. Determination of Exchange Coupling

Once a value of B_2^0 is determined from the anisotropic inverse susceptibility of $Dy_{0.07}Y_{0.93}AgSb_2$, the coupling constants of the exchange interaction in $DyAgSb_2$ may be

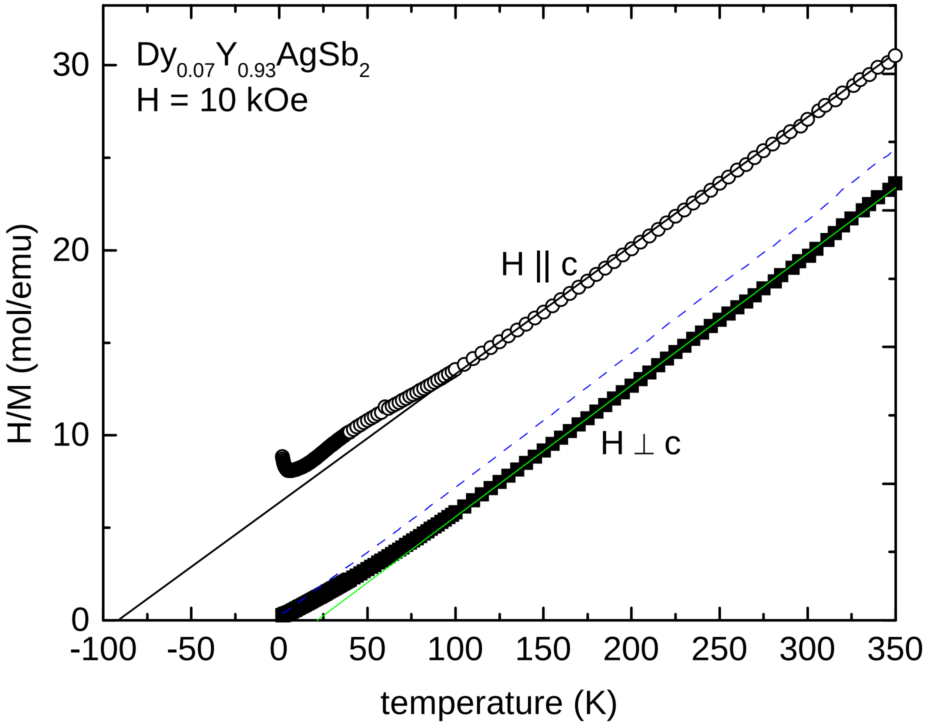

Fig. 4.27 Inverse susceptibility of $Dy_{0.07}Y_{0.93}AgSb_2$ in a 10 kOe field for H || c (○) and H ⊥ c (■). Solid lines represent linear fit to the H/M data. Dotted line is the inverse susceptibility of the polycrystalline average, as described in the text.

calculated from the paramagnetic Weiss temperatures using (Boutron, 1973) (Chevalier, 1985):

$$\theta_p^c = -\frac{J(J+1)}{3k_B} J_{ex}^c + \frac{(2J-1)(2J+3)}{5k_B} B_2^0$$
$$\theta_p^{ab} = -\frac{J(J+1)}{3k_B} J_{ex}^{ab} - \frac{(2J-1)(2J+3)}{10k_B} B_2^0 .$$

In $DyAgSb_2$ the anisotropic Weiss temperatures of θ_p^c = -86.3 and θ_p^{ab} = 7.1 K give exchange constants of J_{ex}^c = 0.62 K and J_{ex}^{ab} = 1.39 K. These values imply ferromagnetic interactions within the basal plane and between the planes, which is inconsistent with the observed antiferromagnetic ordering at low temperatures and zero field. However, since $DyAgSb_2$ manifests a rich metamagnetic structure, this discrepancy indicates the need to include higher order terms (Boutron, 1973). Examples of these higher order terms, which were calculated from detailed measurements of the angular dependence of the metamagnetic transitions may be found in Chapter 5.

2.13.3. Planar Metamagnetism

In addition to the axial-planar magnetic anisotropy, considerable anisotropy is observed within the basal plane. A dramatic example of this occurs in $DyAgSb_2$ (Fig. 4.22) where sharp step-like metamagnetic transitions shift both their critical fields and net magnetic moments as a function of the orientation of the applied field in the basal plane. Other field-dependent magnetic transitions are readily observed in the compounds containing Nd, Tb, and Ho. As with $DyAgSb_2$, considerable in-plane anisotropy may be present in these compounds and further study is needed to quantify this. Although these compounds lack the striking step-like behavior observed in $DyAgSb_2$, clear upward curvature is observed in M(H) at 2 K for H applied perpendicular to the c-axis. Since all M(H) measurements were performed at 2 K, the effective temperature increases as the magnetic ordering temperature decreases. Therefore, it is not surprising that any metamagnetic behavior would be thermally broadened in the Nd, Ho, and Er compounds where T_N is less than 5 K. On the other hand, $DyAgSb_2$ and $TbAgSb_2$ have relatively high ordering temperatures (9 and 11 K, respectively). Considering the higher T_N of the Tb compound, it is surprising that the field-induced transition is so smooth at 2 K. Since the dG factor is representative of the exchange energy, it is possible that the stronger exchange in the Tb compound is pushing the metamagnetic transitions out of the field range of our magnetometer.

2.13.4. DeGennes Scaling

Neglecting crystalline electric field effects, the scaling of the ordering temperatures across the $RAgSb_2$ series may be described within the framework of Weiss molecular field theory where the magnetic ordering temperature may be approximated by (Noakes, 1982):

$$T_M = \frac{2}{3} I (g_J - 1)^2 J(J+1),$$

where I is the exchange interaction parameter and $[(g_J\text{-}1)^2 J(J+1)]$ is the de Gennes factor (dG) with J being the total angular momentum of the Hund's rule ground state of the rare earth ion and g_J is the Landé g factor. The overall trend of increasing ordering temperature with increasing dG factor [Fig. 4.28(a)] is consistent with the magnetic interaction between the local moments of the rare earth ions being an indirect exchange via the conduction electrons, the Rudermann-Kittel-Kasuya-Yosida (RKKY) interaction. However, as seen in Fig. 4.28(a), significant deviations from linearity are present, suggesting other factors may be involved.

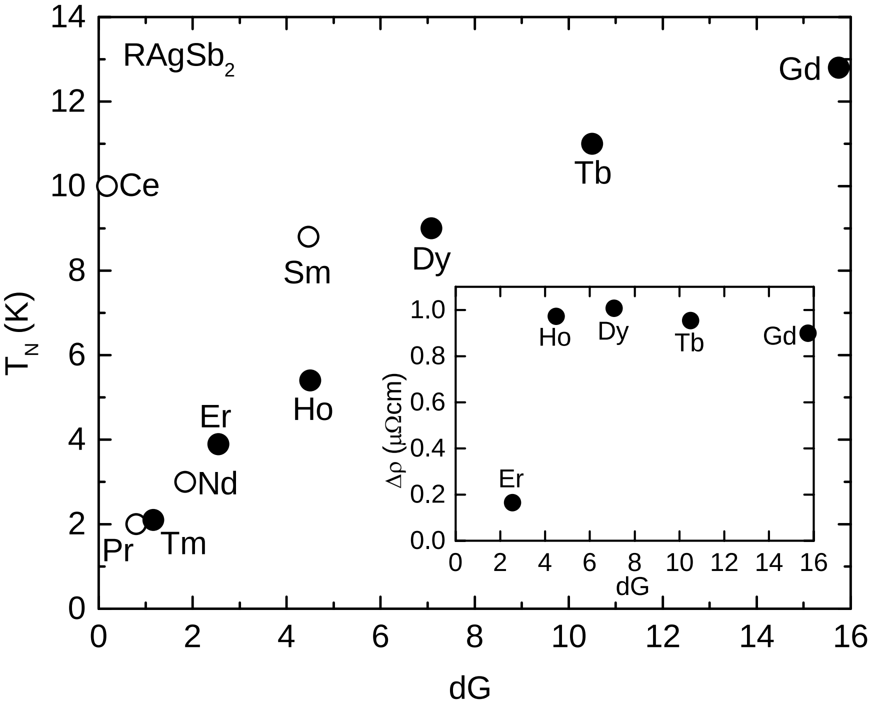

Fig. 4.28 (a) Magnetic ordering temperature (T_N) versus the de Gennes factor [dG = $(g_J-1)^2J(J+1)$]. Inset: loss of spin-disorder scattering as a function of de Gennes factor. (b) dependence of Weiss paramagnetic temperature on the de Gennes factor for H || c (○), H ⊥ c (■) and the polycrystalline average (+).

Deviations from this scaling may occur when a strong CEF constrains the moments to either along the c-axis or within the basal plane. Since for the axial case ($B_2^0 < 0$), the CEF constrains J_z to equal J resulting in an enhancement in the ordering temperature, $T_{M,}$ given by (Noakes, 1982):

$$T_{M,axial} = 2I(g_J - 1)^2 J^2 ,$$

resulting in a higher T_M for R= Er and Tm. Although the strong CEF splitting may be responsible for the higher than expected T_N of $ErAgSb_2$, this still can not account for the lower than expected T_N of $GdAgSb_2$, relative to the compounds with R = Tb, Dy, and Ho. $HoAgSb_2$ and $DyAgSb_2$.

Within the mean field approximation, the Weiss paramagnetic temperature, θ_p, arises from indirect interactions between the local moments. Therefore, θ_p may also be expected to scale with the strength of these interactions, and hence, the de Gennes factor. This may be expressed as (Coqblin, 1977):

$$k_B \theta_P = -\frac{3\pi}{4} \frac{z^2 m^* \Gamma_{eff}^2}{\hbar^2 k_F^2} (g_J - 1)^2 J(J+1),$$

where Γ_{eff} is the effective interaction between the conduction electrons and local moments and also dependent upon both the crystal structure and oscillatory nature of the RKKY interaction. Figure 4.28(b) shows that for the $RAgSb_2$ series of compounds, the paramagnetic temperatures fail to scale with the de Gennes factor. This deviation may simply be the result of CEF anisotropy. More detailed analysis requires the removal of the CEF effects through either a detailed study of the CEF in dilute compounds, such as the previously mentioned $Dy_{0.07}Y_{0.93}AgSb_2$ measurements, or magnetic measurements on polycrystalline samples or powdered single crystals.

2.13.5. Resistivity

Above the magnetic ordering temperatures, the resistivity for the $RAgSb_2$ series of compounds is common to other intermetallic compounds. A positive curvature in the resistivity is observed in most of the compounds below 100 K, consistent with a decrease in the number of phonons at low temperature. At higher temperatures, the resistivity becomes linear with temperature, suggesting the electron-phonon interaction is the dominant scattering mechanism. Up to the maximum temperature of 300 K, no saturation of the resistivity is observed.

2.13.6. Transverse Magnetoresistance

The magnitude of the transverse magnetoresistance at 2 K varies widely in the $RAgSb_2$ with $\Delta\rho(H=55\ kOe)/\rho(0)$ ranging from 0.1 in $ErAgSb_2$ to nearly 65 in $SmAgSb_2$. The existence of de Haas-van Alphen and Shubnikov-de Haas oscillations at relatively low fields and high temperatures, low residual resistivities (typically $< 10^{-6}\ \Omega cm$) and large magnetoresistances suggest that $\omega_c\tau >> 1$ for relatively small fields. Since, as an approximation $\omega_c \approx eH/m^*$, the high value for $\omega_c\tau$ is most likely a consequence of very high sample purity, which increases the time between electron scatterings, τ, and small electron effective mass. Since no saturation is observed in the transverse magnetoresistance, for either $H \parallel c$ or $H \perp c$, it is likely that the $RAgSb_2$ compounds are at least partially compensated, although the existence of open orbits can not be dismissed.

It is clear from the Kohler plots [Figs. 4.29(a) and (b)] that the transverse magnetoresistance of the $RAgSb_2$ series (R=Y, La-Nd, Sm) fails to show a quadratic dependence at all applied fields below 55 kOe, with least squares fits giving power law dependencies of the field ranging from $\Delta\rho/\rho \propto H^{0.94}$ for $LaAgSb_2$ to $\Delta\rho/\rho \propto H^{1.6}$ for $SmAgSb_2$. Furthermore, the slope of the transverse magnetoresistance of each compound in the Kohler plots are similar for H || c and H ⊥ c, which indicates approximately the same power law dependence for both orientations. This deviation from quadratic magnetoresistance is similar to that observed in the RSb_2 compounds, where the exponent for the power law fit of $\Delta\rho/\rho$ varied from 1.0 to 1.3 (Bud'ko, 1998). Although exact knowledge of the Fermi surface is required for any detailed discussion of the transverse magnetoresistance, a thorough review of possible mechanisms for linear magnetoresistance may be found in Bud'ko (1998).

The low temperature rise in the resistivity in the presence of an applied field along the c-axis is a consequence of Kohler's rule: $\Delta\rho(H,T)/\rho(H=0,T) = F(H/\rho_0)$, where $F(H/\rho_0)$ is a function of H/ρ_0 and $\rho_0=\rho(H=0,T)$. This may be rewritten as $\rho(H,T)=\rho_0 F(H/\rho_0)+ \rho_0$. From this, it is clear that as long as the dominant behavior of $F(H/\rho_0)$ goes as $(H/\rho_0)^n$ with $n\geq1$, the resistivity in a given applied field will increase as ρ_0 decreases. It is also evident that the increase in magnetoresistance becomes particularly pronounced when a loss of spin-disorder scattering sharply suppresses ρ_0 for $T<T_N$, as observed in compounds with magnetic rare earths. As an example, consider the transverse magnetoresistance of $SmAgSb_2$ [inset, Fig. 4.14 (b) and Fig. 4.29(a)]. From the 2 K, H || c transverse magnetoresistance data, $F(H/\rho_0) = 4.13\times10^{-3}(H/\rho_0)^{1.6}$, with H expressed in kOe. This expression may then be used to model the temperature dependence of the magnetoresistance, assuming Kohler's rule is valid. The results of this model, with three different values for the applied field, are shown in Fig. 4.30, along with the experimental zero field, 16, 40 and 55 kOe resistivities for $SmAgSb_2$ with

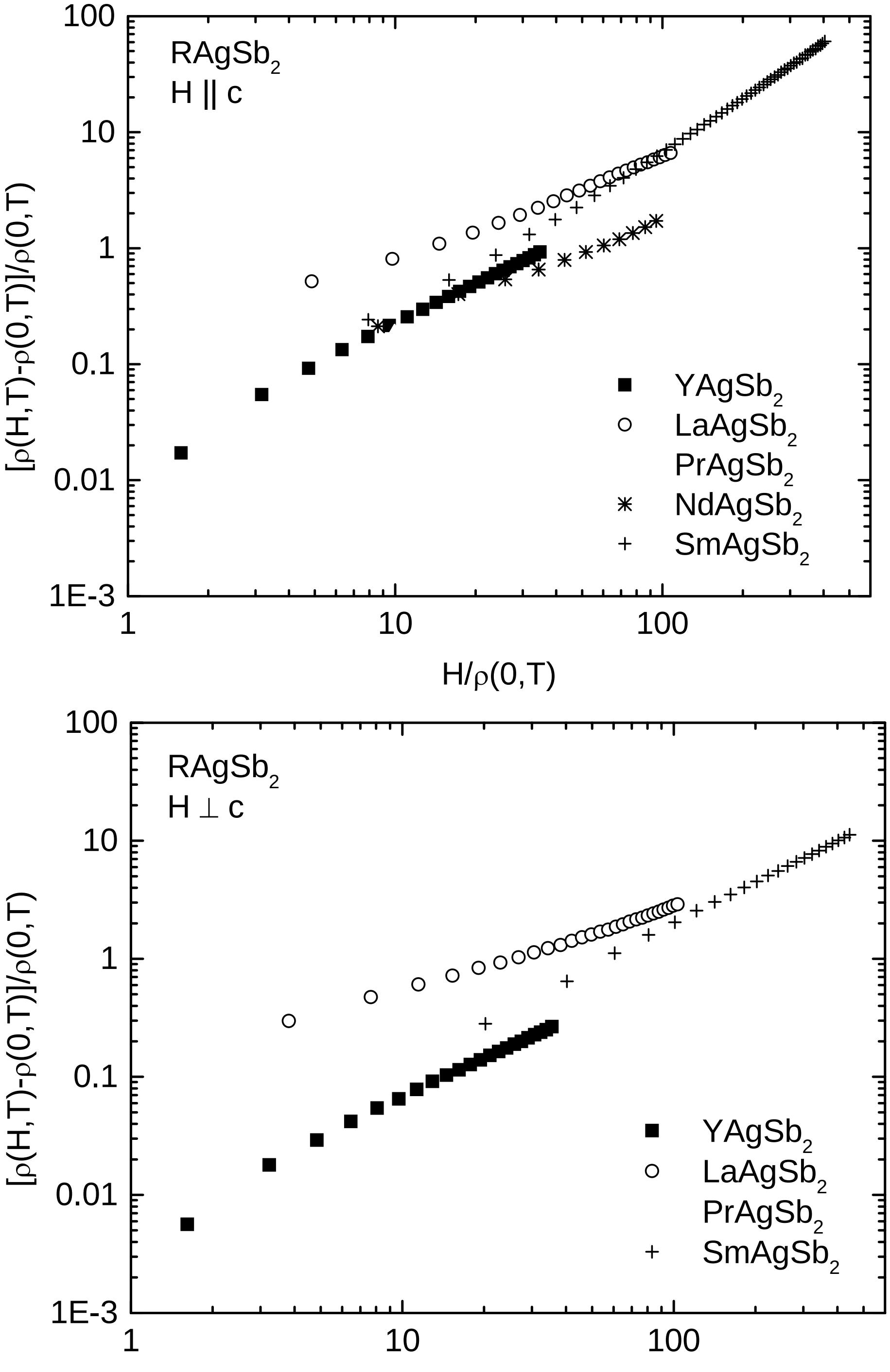

Fig. 4.29 Kohler plot of the transverse magnetoresistance at 2 K for (a) H || c, and (b) H ⊥ c for YAgSb$_2$ (■), LaAgSb$_2$ (○), PrAgSb$_2$ (▲), LaAgSb$_2$ (*), and LaAgSb$_2$ (+)

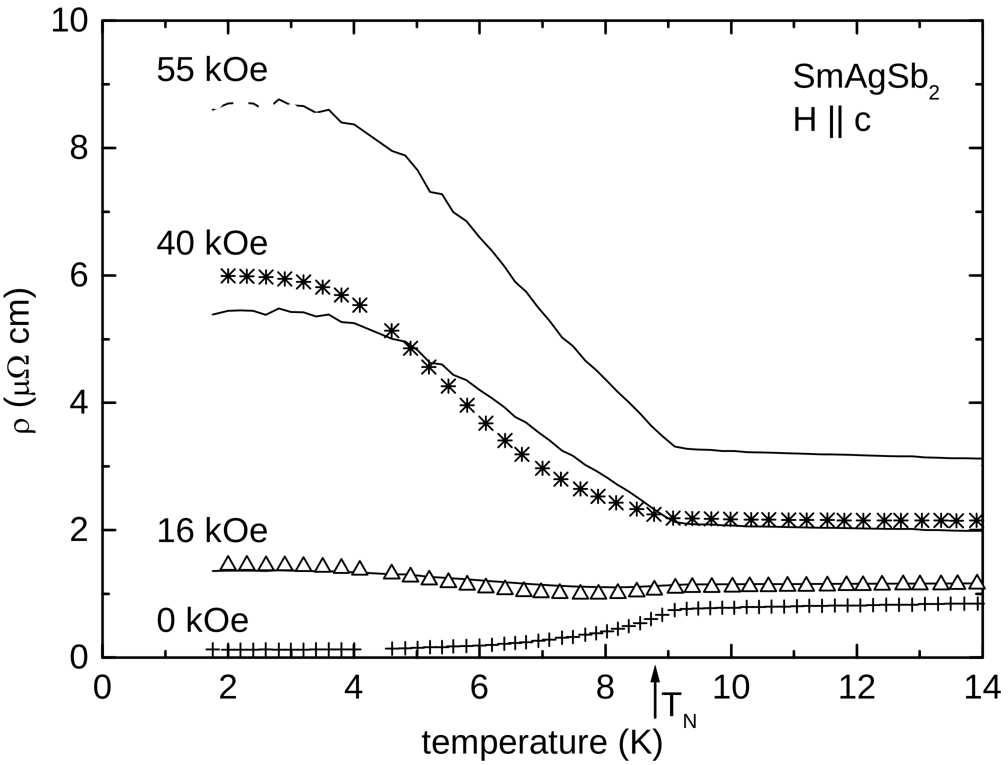

Fig. 4.30 Resistivity (ρ) as a function of temperature for H || c in SmAgSb$_2$ for H =0 (+), 16 kOe (Δ), 40 kOe (*) and 55 kOe (•). The solid lines represent data modeled from Kohler's rule as described in text.

H || c. The modeled data (solid lines) are in agreement with the experimental values of ρ(H,T), indicating that the decrease in magnetoresistance with increasing temperature is a consequence of Kohler's rule. In addition, this model adequately describes the temperature dependence of the magnetoresistance for R = Pr, Nd, Gd-Dy. In each of these cases the magnetoresistance decreases below T_N and then becomes larger as the magnetic contribution to the scattering decreases, similar to the 16 and 40 kOe data in Fig. 4.30, suggesting that the smaller values of ρ(H,T) at low temperatures are consistent with larger amounts of impurity scattering and possible differences in the Fermi surface, modifying $\omega_c\tau$.

2.13.7. Transverse Magnetoresistance and Metamagnetic Transitions

When the magnetic field is applied along the easy axis in compounds containing Dy, Ho, and Er, sharp peaks followed by a decrease in the magnetoresistance are superimposed on the nearly linear and anisotropic response seen the light rare earth compounds. This anomalous behavior coincides with the critical fields of the metamagnetic transitions when the field is applied along the easy axis. No anomalies are present in the magnetoresistance when the field is perpendicular to the easy axis. This behavior is qualitatively consistent with the predictions of Yamada and Takada (1973), although their model assumes the material is metallic, antiferromagnetic orders with the moments constrained along the c-axis, and has a spherical Fermi surface. The magnetic properties of their model include weak axial anisotropy with a first order spin flop transition at H_{C1}, and a second order transition to a saturated paramagnetic state at H_{C2}. Within this framework, the contribution to the magnetoresistance ($\Delta\rho/\rho$) for H || (easy axis) is expected to be positive and proportional to H^2 for $H \ll H_{C1,}$ have a local maximum at H_{C1} and at higher fields become negative and proportional to $\sqrt{H/H_{C1}-1}$. Qualitative agreement is good for both $HoAgSb_2$ and $ErAgSb_2$, where only a single metamagnetic transition is observed. Agreement with this model suffers in $DyAgSb_2$, due to the complicated series of metamagnetic transitions which creates a plateau in the resistance between the first and final critical fields.

2.14. Summary

Anisotropic magnetization and transport measurements have been performed on most of the members of the $RAgSb_2$ series of compounds. Strong anisotropies due to CEF splitting of the Hund's rule ground state multiplet constrain the local moments to the basal plane for the whole series, except for $ErAgSb_2$ and $TmAgSb_2$ which are axial. From the inverse susceptibility at high temperatures, estimates of the leading term in the CEF Hamiltonian may be determined. All of the compounds with magnetic rare earth ions antiferromagnetically order at low temperatures except for $PrAgSb_2$ (which does not order) and $CeAgSb_2$ (which is ferromagnetic.) From the failure of T_N and θ_P to scale linearly with the de Gennes factor, even when CEF effects are considered, it is deduced that the electronic structure varies with the choice of rare earth (Taylor, 1972). This may indicate the existence of small pockets of Fermi surface, which would be particularly sensitive to changes in the lattice constants with varying rare earth ions. Finally, the magnetic isotherms reveal metamagnetic transitions in most of the compounds, with $DyAgSb_2$ being a particularly dramatic example.

The transverse magnetoresistance at 2 K is found to be very large throughout the series, suggesting that the electrons have small effective masses and extraordinarily long relaxation times. This is consistent with the large residual resistivity ratios obtained for most of the members, indicating low impurity and dislocation concentrations. Also appearing in the magnetoresistance are anomalies corresponding to the metamagnetic transitions. Several theories have been proposed to account for these. However, their utility is limited, due to lack of knowledge of the electronic structure and wave vector of the magnetic ordering. Clearly, neutron and magnetic X-ray diffraction would provide more insight into the magnetic and transport properties of these materials.

ANGULAR DEPENDENCE OF METAMAGNETIC TRANSITIONS IN $DyAgSb_2$

2.15. Introduction

Recent studies of $HoNi_2B_2C$ and other RNi_2B_2C compounds have shown that the net distribution of magnetic moments in a metamagnetic system may be determined from the analysis of the angular dependence of the magnetization and transition fields of the metamagnetic states (Canfield 1997a, Canfield 1997b, Kalatsky 1998). Although no information about the wavevector associated with the metamagnetic ordering may be obtained, this approach allows a vast amount of information to be gained about the metamagnetic phases, without requiring neutron or magnetic x-ray diffraction.

In $HoNi_2B_2C$, a strong crystalline electric field (CEF) anisotropy constrains the local moments to the [110] crystallographic axes, leading to four well-defined metamagnetic states with relatively simple angular dependence. This angular dependence suggests that the net distribution of magnetic moments may be described by $\uparrow\downarrow$ for $H < H_{c1}$, $\uparrow\uparrow\downarrow$ for $H_{c1} < H < H_{c2}$, $\uparrow\uparrow\rightarrow$ for $H_{c2} < H < H_{c3}$, and $\uparrow\uparrow\uparrow$ for $H > H_{c3}$, where $\uparrow$ and $\rightarrow$ correspond to the moment directed either along or perpendicular to the [110] axis nearest to the field and H_{ci} are the four angular dependent critical fields. Recent theoretical work (Kalatsky 1998) has analyzed these data within the framework of the “4-position clock model,” where the local moments are restricted to either the <110> or <100> sets of axes by a strong CEF anisotropy.

To further understand this type of planar metamagnetism, we have undertaken a search for other systems that have rare earth ions in locations with tetragonal point symmetry. Although the RSb_2 series with R = Ce, Pr, and Nd is strongly anisotropic and exhibits sharp well-defined metamagnetic states for the field applied within the ab-plane (Bud'ko 1998), the crystal structure is weakly orthorhombic (Hullinger 1979, Wang 1967), which greatly complicates the analysis of the magnetic structure. In contrast to the RSb_2 series of compounds, $RAgSb_2$ crystallizes in the simple tetragonal $ZrCuSi_2$ structure (P4/nmm, # 129) (Brylak 1995, Flandorfer 1996, Sologub 1994) consisting of Sb-RSb-Ag-RSb-Sb layers with the R^{3+} in a location with tetragonal point symmetry (4mm).

Measurements of the magnetization as a function of applied field along high symmetry axes in $DyAgSb_2$ revealed a series of 4 sharp steps in the magnetization for the field applied within the basal plane, making the compound a potential candidate for further study of the angular dependence of metamagnetic states.

In this paper, we present a study of the angular dependence of the metamagnetic transitions of $DyAgSb_2$. After an overview of the experimental techniques used to grow and characterize the samples, results and plausible model of the net distribution of magnetic moments will be presented. Finally, the angular dependencies of the critical fields will be used to deduce the coupling parameters within the framework of the 4-position clock model.

2.16. Experimental Methods

Magnetic measurements were performed in a Quantum Design SQUID magnetometer with a specially modified sample holder to rotate the sample, keeping the c-axis perpendicular to the field. A sample mass below 0.5 mg was used to avoid torque on the rotator due to the extreme magnetic anisotropy. To reduce the effects of weighing errors, M(H) data were collected on a 10.62 mg sample from the same batch, for H || [100] and [110]. The data from the small sample were then normalized to the larger

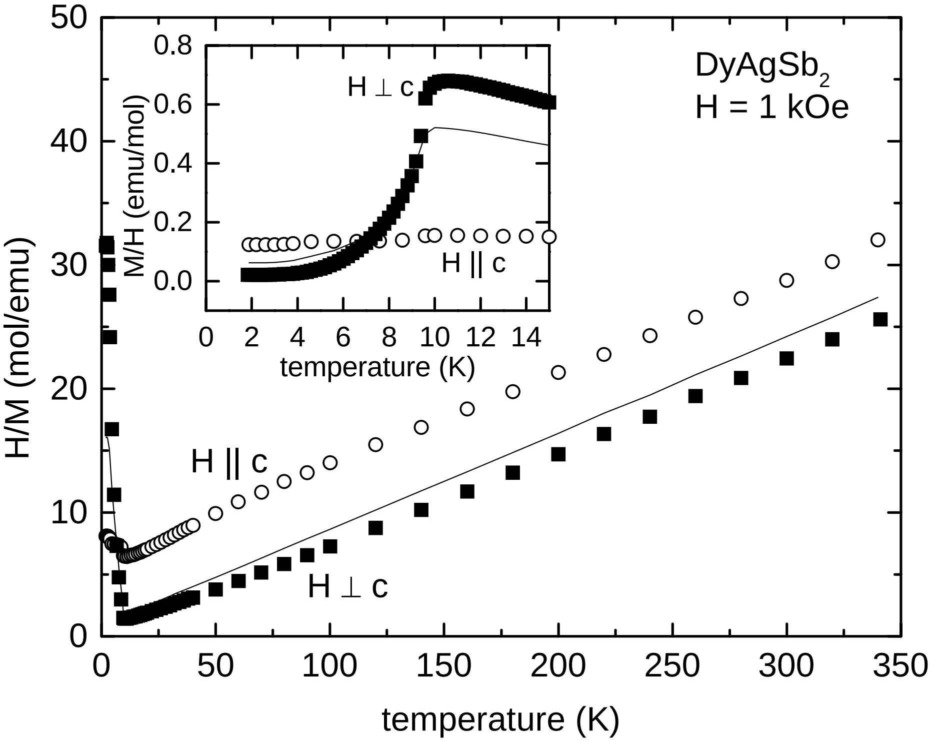

Fig. 5.1 Applied field divided by magnetization (H/M) for H || c (■) H ⊥ c (○) and polycrystalline average (solid line) versus temperature for DyAgSb$_2$. Inset: low temperature behavior of magnetization divided by field for H || c (■) H ⊥ c (○), and polycrystalline average (solid line).

sample data. Angular uncertainty in the rotator is estimated to be less than 1°. Additional uncertainty in the sample orientation could arise from a failure to align the c-axis of the sample exactly perpendicular to the applied field. However, due to the construction of the sample holder, this misalignment should be no more than 10°.

2.17. Experimental Results

2.17.1. Temperature Dependence of the Magnetization

The inverse susceptibility (Fig. 5.1) of DyAgSb$_2$ illustrates the strong anisotropy, with the local Dy moments aligning within the basal plane. Above 100 K, the inverse susceptibilities are linear, allowing fits to the Curie-Weiss law. The polycrystalline average, determined by $(2\chi_{H\perp c}+\chi_{H||c})/3$, yields an effective moment of 10.3 μ_B /Dy and a Weiss temperature of –10.1 K. Anisotropic Weiss temperatures are -86.3 K for H || c and 7.1 K for H ⊥ c. The inset to Fig. 5.1 clearly shows that magnetic ordering is present below 9 K, with the susceptibility for H ⊥ c rapidly decreasing below 9 K.

2.17.2. Applied Field Dependence of the Magnetization and Hysteresis

In order to better understand the nature of the ordering below 9 K, magnetization as a function of applied field was measured at 2 K for H parallel to the c-axis and for H parallel to [100] and [110], shown in figure 5.2. For the applied field along the c-axis, the magnetization is linear, only reaching about 1.6 μ_B/Dy at 55 kOe. However, for the applied field in the basal plane, four well-defined metamagnetic states and the low-field antiferromagnetic state are observed, with the transition fields and the plateau magnetizations varying strongly with the angle of the applied field. At 55 kOe, M for H || [110] is slightly less than 10 μ_B/Dy while for H || [100] M is approximately 7.2 μ_B/Dy. This is consistent with the easy magnetic axis being along the <110> directions. In addition, some of the field-induced magnetic transitions exhibit field up/field down hysteresis. In particular, the higher field knee-like states (M_3 and M_6) persist for a greater range of fields as the magnitude of the applied field is decreased.

2.17.3. The Stability of the Knee-Like States

Although the range of stability of the knee-like states M_1, M_3, M_4 and M_6 is quite small, the fact that they exist in both the field up and field down data leads to the

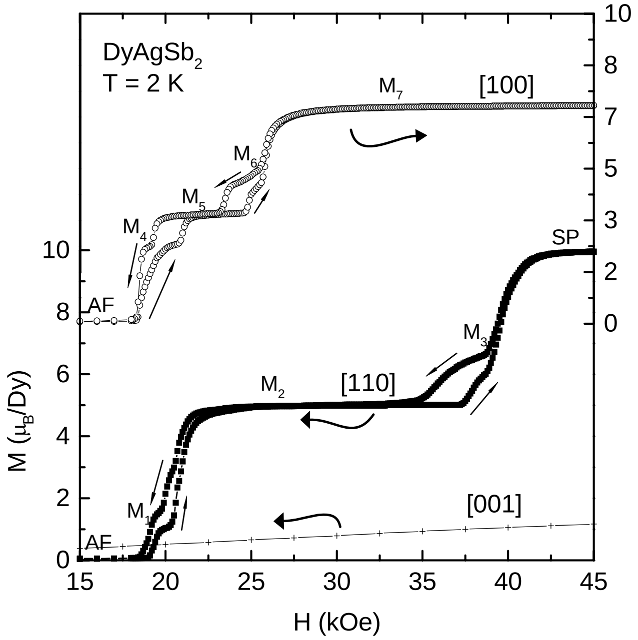

Fig. 5.2 M(H, T= 2 K) for increasing and decreasing field for the field applied along [001] (+, left axis), [110] (■, left axis) and [100] (○, right axis). Note: the offset zero on the right axis.

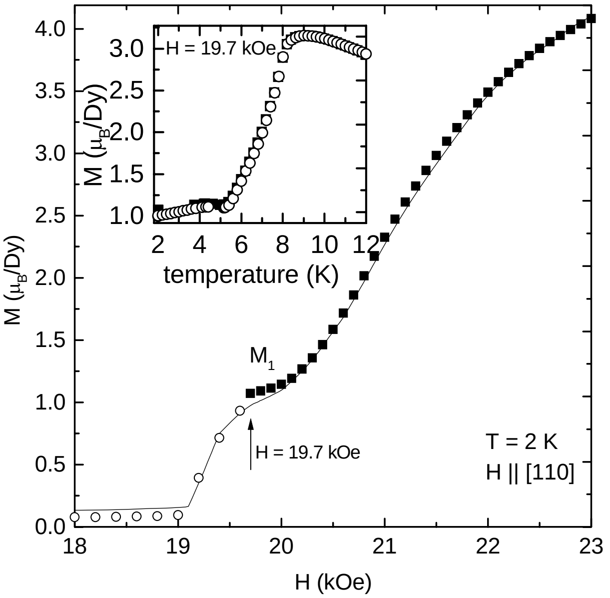

Fig. 5.3 Detail of M(H) for H || [110] for the M_1 state. Solid line is M(H) at 2 K zero-field cooled, Open circles (○) are for zero-field cooled magnetic isotherm up to 19.7 kOe. Squares (■) are magnetic isotherm for the sample cooled to 2 K from 12 K in a 19.7 kOe field. Note: the plateau at 19.7 kOe is stabilized by field cooling. Inset: M(T) in 19.7 kOe for increasing (○) and decreasing temperature (■).

conclusion that they are stable states rather than just metastable, transitional states. As a further test of the stability of these metamagnetic phases, the following experiment was performed. After cooling to 2 K in zero field, M(H) for H || [110] was measured with increasing field up to 19.7 kOe, entering the knee-like M_1 plateau, as shown in Fig. 5.3. Maintaining 19.7 kOe, the temperature was then increased up to 12 K, well above the ordering temperature of 9.5 K, and then decreased back to 2 K (Inset Fig. 5.3) Finally, M(H) was measured for fields greater than 19.7 kOe. These data are consistent with M_1 being thermodynamically stable for this applied field, since the moments would have minimized the energy after the "anneal," by settling into the lowest energy state for the given magnitude and orientation of the magnetic field. By analogy, it is assumed that the M_3, M_4 and M_6 are also stable states.

2.17.4. Temperature-Applied Field Phase Diagrams

Figures 5.4 (a) and (b) show the temperature-applied field phase diagrams for H parallel to [110] and [100], respectively. The points were determined from the local maxima in dM/dH (shown by ○) from M(H) field-increasing scans at selected temperatures and dM/dT (shown by ■) from M(T) scans at selected fields. Both phase diagrams are qualitatively similar at low temperatures, with the knee-like phases M_1, M_3, M_4, and M_6 persisting up to approximately 6 K, and the other metamagnetic states persisting up to about 8 K. However, an additional phase boundary is evident between 9.5 and 11 K in the H || [100] phase diagram, separating the M_7 metamagnetic state and the paramagnetic region. The lack of this upper transition in the H || [110] phase diagram, combined with the fact that M(55 kOe) ≈ $10\mu_B$/Dy, suggests that the high-field, low temperature state may simply be a saturated paramagnet state.

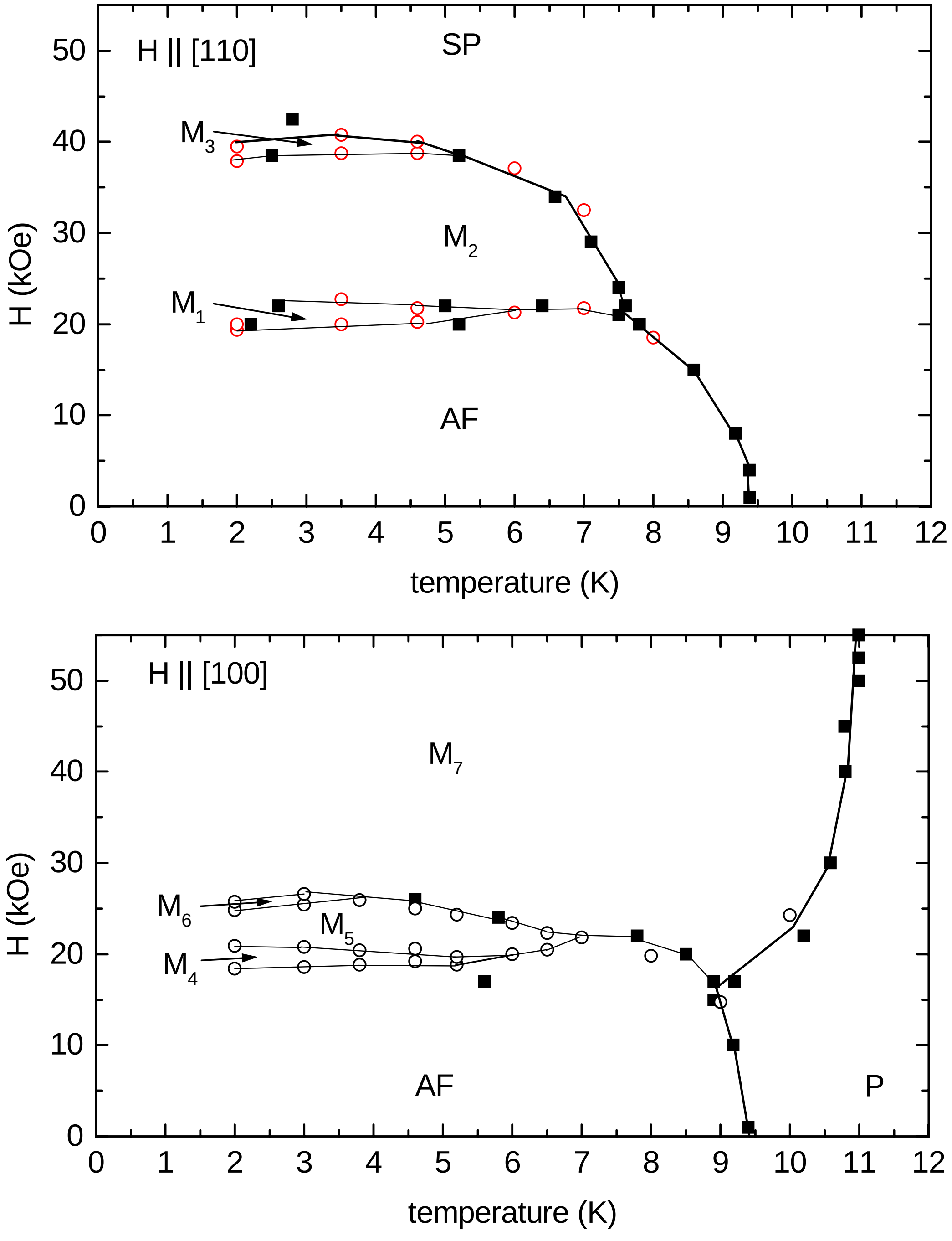

Fig. 5.4 Applied Field-Temperature phase diagrams for (a) H || [110] (b) H || [100]. Points are determined from M(T) (■) and M(H) (○).

2.17.5. Planar Anisotropy and Magnetization Versus Angle

To study the angular dependence of the metamagnetic states, it is important to first determine the single ion anisotropy associated with the CEF splitting of the Hund's rule ground state J-multiplet. To measure this, crystals of $YAgSb_2$ were grown with a small amount of Dy introduced into the melt. From the Curie-Weiss effective moment and the saturated magnetic moment, the crystals were determined to be $Dy_{0.07}Y_{0.93}AgSb_2$. Magnetization versus angle measurements in a 55 kOe field at 2 K for both $DyAgSb_2$ and $Dy_{0.07}Y_{0.93}AgSb_2$ (Fig 5.5) show that the dilute case closely follows a $M \propto \cos(\theta)$ dependence (shown by solid line). Since only the component of the magnetization parallel to

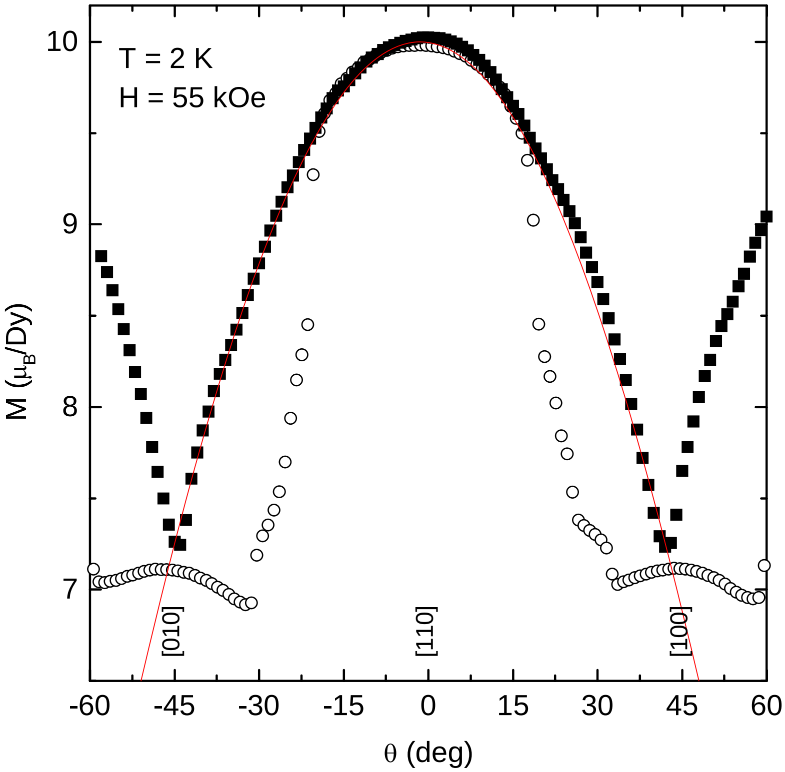

Fig. 5.5 $M(\theta)$ at H=55 kOe for $DyAgSb_2$ (○) and $Dy_{0.07}Y_{0.93}AgSb_2$ (■). Solid line is $M_{sat}=10\mu_B\cos(\theta)$.

the field is measured, this is consistent with the local Dy^{3+} moments being constrained to the nearest easy, [110], axis within the basal plane. Although 4-fold symmetry is also observed in the M(θ) scans of $DyAgSb_2$, large deviations from $M \propto \cos(\theta)$ are readily apparent, where interactions between local moments (deviations from cos(θ)) and hysteresis (asymmetry of M(θ) curves) affect the magnetization. These data are consistent with a number of metamagnetic states crossing 55 kOe at different angles.

2.17.6. Magnetization as a Function of Applied Field and Angle

Magnetization isotherms are shown in Figs. 5.6 (a-c) for a series of angles relative to the easy [110] axis, divided into three angular regions for clarity. In region I ($\theta < 10^\circ$), five different states are observed. Below 19 kOe, the compound orders in the antiferromagnetic state (AF). As the field increases, a small knee-like state (M_1) is followed by a well-defined plateau (M_2) with a saturated moment near 5 μ_B/Dy. Above 38 kOe, another knee-like state (M_3) is followed by a final plateau, corresponding to the

saturated paramagnetic (SP) state with a moment close to the full saturated moment, $g_J J \mu_{B,}$ of the Hund's rule ground state of 10 μ_B/Dy.

For angles between 10° and 25° (Region II), the magnetization isotherms become more complex, with as many as 7 metamagnetic states appearing, depending on the angle of the applied field. Many of these states are present for limited field and angular ranges, sometimes only appearing as inflection points with no clear plateaus in the magnetization. (M_5 and M_7) each preceded by a knee-like step (M_4 and M_6). In this case, however, the

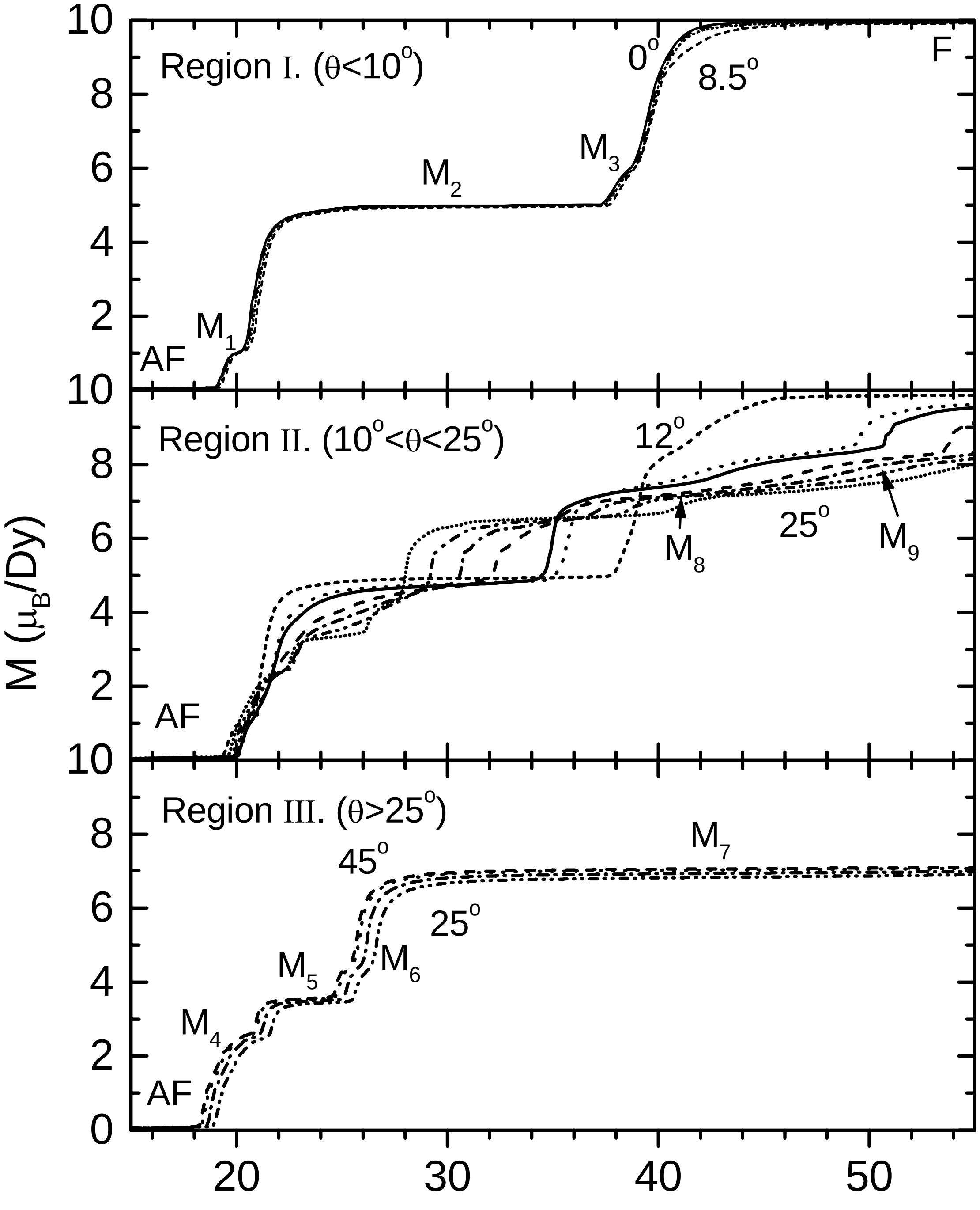

Fig. 5.6 Magnetization (M) versus applied field (H) at 2 K for a variety of angles relative to the easy axis, [110]. (a) angles (θ) less than 10° (b) angles between 10° and 25°, (c) angles between 25° and 45°.

When the angle increases above 25º (Region III), the magnetization isotherms become similar to region I, with the low field antiferromagnetic state (AF) and 2 large steps maximum value for the magnetization in the highest field state (M_7) approaches only about 7.2 μ_B /Dy as seen in Fig. 5.6(c).

From the magnetization isotherms [Figs. 5.6 (a-c)], the critical fields (H_c) and saturation magnetizations (M_{sat}) may be determined for each state as a function of angle, shown in Figs. 5.7(a) and (b), respectively. When possible, the saturated magnetic moment (M_{sat}) was determined by the magnetization, M(H), midway between the bordering transition fields (shown by • in the figure). For the highest field states, M_{sat} was simply determined by the magnetization at the highest field attained (55 kOe).

The critical fields, determined from local maxima in dM/dH, are shown in Fig. 5.7 (b). For transitions at angles between 12º and 25º, the peaks in dM/dH were frequently broad and poorly defined, particularly for the higher field states. Consequently, no meaningful direct fit to an angular function could be made (see below).

From the magnetization isotherms shown in Figs. 5.6(a-c) and the angular dependence of the critical fields and saturated moments [Figs. 5.7(a) and (b)], it is natural to divide the analysis into three regions. Within region I, the critical fields of the four states (2 large steps, and 2 knees) are a minimum at $\theta = 0^o$ and increase slightly as the angle increases. The solid lines in this region are fits to $H_c(\theta) = H_c/\cos(\theta)$ with $H_{cAF,1} = 19.4$, $H_{c1,2} = 20.6$, $H_{c2,3} = 37.8$, and $H_{c3,4} = 39.4$ kOe, where $H_{cAF,1}$ denotes the critical field between the AF and M_1 states. The saturated moments of these states are all a maximum at 0º and decrease

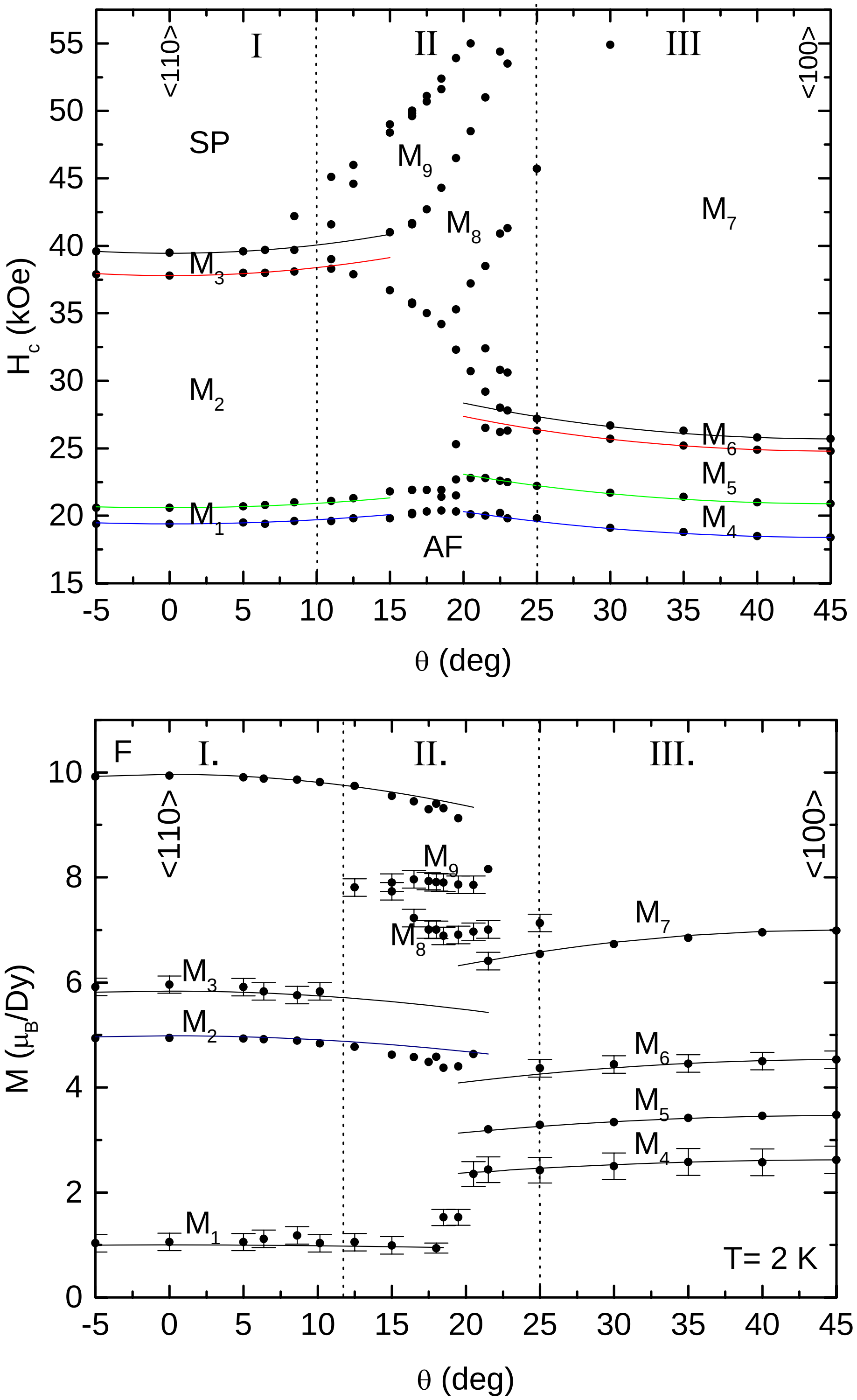

Fig. 5.7 Angular dependence of (a) saturated moment (M_{sat}) and (b) critical field (H_c) using criteria described in text. Solid lines are fits to the data.

as the angle increases. The solid lines in the figure show fits to $M_{sat} = M_{sat}\cos(\theta)$ with M_{sat1} = 1.0, M_{sat2} = 5.0, M_{sat3} = 5.8, and M_{sat4} = 10.0 μ_B/Dy.

In Region III, the critical fields of the 4 transitions are all minimized at 45°. Fits (shown by solid line) show that $H_c(\theta) = H_c/\cos(45^o-\theta)$ with $H_{cAF,4}$ = 18.4, $H_{c4,5}$ = 20.9, $H_{c5,6}$ = 24.8, and $H_{c6,7}$ = 25.7 kOe. Likewise the saturated moments are maximized at 45° and vary as $M_{sat}\cos(45^o-\theta)$ with M_{sat4} = 2.6, M_{sat5} = 3.5, M_{sat6} = 4.5, and M_{sat7} = 7.2μ_B/Dy.

2.18. Experimental Data Analysis

2.18.1. Angular Dependence of Saturated Magnetization

Despite the complexity of the metamagnetism presented in this system, it is possible to create a consistent model of the net distribution of the magnetic moments. To facilitate this, we introduce the 4-position clock model (Kalatsky 1998). This model arises from a strong CEF anisotropy restricting the local moments to lie along one of four crystallographically similar orientations within the basal plane given by ↑, ←, ↓, →, or angles relative to the nearest easy <110> axis (0, 90, 180, or 270°).

Within this model, the net distribution of the local moments may be determined from the angular dependence of the critical fields and saturated moments of the metamagnetic states (Canfield 1997a). Since the magnetometer measures only the projection of the magnetic moment along the applied field, the angular dependence of the magnetization of an arbitrary state is given simply by:

$$M_{Sat}(\theta) = \frac{M}{N}\sum_i \cos(\theta - \phi_i),$$

where θ is a continuous variable expressing the orientation of the applied field and ϕ_i is a discrete variable denoting the orientation of the ith moment relative to the easy axis, free to take values of 0, 90, 180, or 270°. N is the number of moments needed to describe the state, and M is the saturated moment of the free Dy^{3+} ion in the CEF split ground state. Therefore, when $M_{sat}(\theta) \propto \cos(\theta)$, all of the moments are aligned parallel to the closest easy axis or are cancelled out by antiparallel moments (e.g. ↑↑↑↓ or ↑↑↑↑). However, when $M_{sat} \propto \cos(45^{o}-\theta)$, an equal number of moments are directed along the two nearest easy orientations with the rest of the moments canceling each other (e.g. ↑↓↑→, ↑→) since, $\cos(\theta) + \cos(90^{o}-\theta) = \sqrt{2}\cos(45^{o}-\theta)$. It should be noted that it is impossible to determine from magnetic measurements whether canceling antiparallel pairs of moments consist of ↑↓ or ←→. For simplicity, ↑↓ will be used to denote a pair of canceling moments.

Regions of the data in Fig. 5.5 are consistent with the two extremes described above. For the isolated Dy ion in the $Dy_{0.07}Y_{0.93}AgSb_2$ pseudoternary the moment is always along the nearest easy [110] axis. For the concentrated $DyAgSb_2$, in which the Dy moments are ordered at low temperature, for $-15^{o} < \theta < 15^{o}$ the moments have a behavior consistent with the saturated paramagnetic state. On the other hand, for $30^{o} < \theta < 60^{o}$, $M(\theta)$ follows $\cos(\theta-45^{o})$, consistent with an ordered structure with a net distribution of moments ↑→.

2.18.2. Angular Dependence of Critical Fields

An equally simple argument may be used to determine the angular dependence of the critical fields. Since the energy due to a moment in a magnetic field is just H•M, the difference in energy to due to application of magnetic field between two different metamagnetic states (consisting of N_1 moments with orientations ϕ_{i1} and N_2 moments with orientations ϕ_{i2}) is simply:

$$\Delta E_{2,1} = \frac{HM}{N_2}\sum_{i}^{N_2}\left[\cos(\theta-\phi_{i2})\right] - \frac{HM}{N_1}\sum_{i}^{N_1}\left[\cos(\theta-\phi_{i1})\right].$$

If a critical energy (E_{Crit}) exists which must be exceeded to induce the next higher metamagnetic state, then the critical field will be given by:

$$H_{c2,1}(\theta) = \frac{E_{crit}}{\frac{1}{N_2}\sum_{i}^{N_2}\left[\cos(\theta-\phi_{i2})\right] - \frac{1}{N_1}\sum_{i}^{N_1}\left[\cos(\theta-\phi_{i1})\right]}.$$

In principle, E_{Crit} may be taken as a constant for a given transition since it depends only on the differences in the coupling between the two metamagnetic states. Therefore, the angular dependence of the critical fields may be used to gain insight into the net distribution of moments of the metamagnetic phases without a priori knowledge of the details of the ordering. For example, the critical field for a transition from ↑↓ (AF) to ↑↓↑↑ (M_2) (i.e. a flip of one spin from ↓ to ↑) will be proportional to 1/cos(θ) while a transition from ↑↓ (AF) to ↑↓↑→ (M_5) (i.e. a flip of one spin from ↓ to →) will be proportional to 1/cos(45°-θ).

2.18.3. Determination of the Net Distributions of Moments

It is now possible to assign net distribution of moments for each of the metamagnetic states. For the two large plateaus within region I (M_2 and SP), the saturated moment as a function of angle closely follows $M_{sat}\cos(\theta)$, suggesting that all of the moments are either canceled by an antiparallel moment (↑↓) or lie along the nearest axis to the field (↑). Since the magnetization for state SP corresponds to the saturated moment for Dy^{3+}, all of the moments must be parallel giving a net distribution of moments of ↑. The saturated moment of M_2 is near 5 μ_B/Dy, consistent with half of the moments canceling and half aligned parallel to 0° giving ↑↓↑↑. Since the two knee-like states (M_1 an M_3) are stable for a very limited range of fields, an accurate determination of the saturated moment is difficult. However, Fig 5.7(a) shows the angular dependence of M_{sat} for these states is consistent with $M_{sat}\cos(\theta)$ with $M_{sat1} \approx 1.0\ \mu_B/\mathrm{Dy}$ and $M_{sat3} \approx 5.8\ \mu_B/\mathrm{Dy}$. From these estimates, a possible net distribution of moments for M_1 is ↑↑↓↑↓↑↓↑↓, although other distributions with a larger number of moments can not be dismissed. Likewise, the magnetization of M_3 corresponds to ↑↑↑↑↓. The angular dependence of the critical fields within region I is consistent with the net distribution of moments for these four states since for all of the transitions, $H_c(\theta) \propto H_c \cos(\theta)$, which is expected for a moment (or multiple moments) flipping from ↓ to ↑.

In region III, the analysis is similarly straightforward. For all of the states, $M_{sat}(\theta) \propto M_{sat}\cos(45^o-\theta)$ and $H_c(\theta) \propto H_c/\cos(45^o-\theta)$. This behavior is consistent with an equal number of unpaired moments parallel and perpendicular to the nearest easy axis (↑→). Starting with M_7, we see that maximum magnetization is about 7.2 μ_B/Dy, corresponding to ↑→, since 7.2 $\mu_B/\mathrm{Dy} \approx 10\ \mu_B/\mathrm{Dy}\cos(45^o)$. Likewise, the plateau magnetization of M_5 is 3.5 μ_B/Dy, close to half of M_7, indicating that half of the moments cancel, yielding a net distribution of moments of ↑↓↑→. Analysis of the two knee-like states within this region, M_4 and M_6, also show similar angular behavior. From the magnetization of these states, possible net distributions of moments are consistent with ↑↓↑↓↑→ for M_4 and ↑→↑→↑↓ for M_6. The angular dependencies of the critical fields corroborate these assignments, since $H_c(\theta) \propto H_c/\cos(45^o-\theta)$ for a change from ↓ to →.

Now that a plausible model for the states in regions I and III has been presented, we can turn the analysis to region II. Within this region (Fig. 5.7), many states exist for extremely limited range of fields and angles, greatly complicating the analysis. Furthermore, two new states appear at high fields, M_8 and M_9. This situation is simplified if a polar plot of the critical fields is made (Fig 5.8). From the polar plot, it becomes clear that many of the transitions observed in region II arise from the M(H) scan crossing a corner of a larger region of phase space, as shown by the line representing the M(H) scan at 18.5°. In the polar plot, the angular dependencies of all of the transitions becomes clear, particularly critical fields involving the two states existing only in region II. As seen in Fig 5.8, four types of transitions are observed, each possessing linear phase boundaries, but with slopes in the polar plot of either 0, ∞, +1, or -1. Since the general equation of a straight line (with slope m and y-intercept b) on a polar plot is given by $R(\theta)=b/(\sin\theta + m\cos\theta)$, the angular dependence of H_c may easily be deduced from the polar plot. Within the lower right half of the phase diagram, the slopes, angular dependencies, and change in net distribution of moments are given by:

$m = 0$	$H_c(\theta) \propto H_c/\sin\theta$	← to →
$m = \infty$	$H_c(\theta) \propto H_c/\cos\theta$	↓ to ↑
$m = +1$	$H_c(\theta) \propto H_c/\sin(45^\circ-\theta)$	→ to ↑
$m = -1$	$H_c(\theta) \propto H_c/\cos(45^\circ-\theta)$	↓ to →

This is consistent with the transitions previously discussed. Furthermore, since $H_{C7,8}$ (the critical field between states M_7 and M_8), $H_{C8,9}$, and $H_{C9,SP}$ all exhibit slopes of near unity in the polar plot, these transitions correspond to flips of one moment from → to ↑. It should also be noted that deviations from linearity or a slope deviating from the aforementioned ones may indicate more complex transitions.

With the net distributions of moments of M_7 known to be ↑→ and SP known to be ↑, it follows that M_8 and M_9 will then consist only of a number of ↑ moments and a smaller

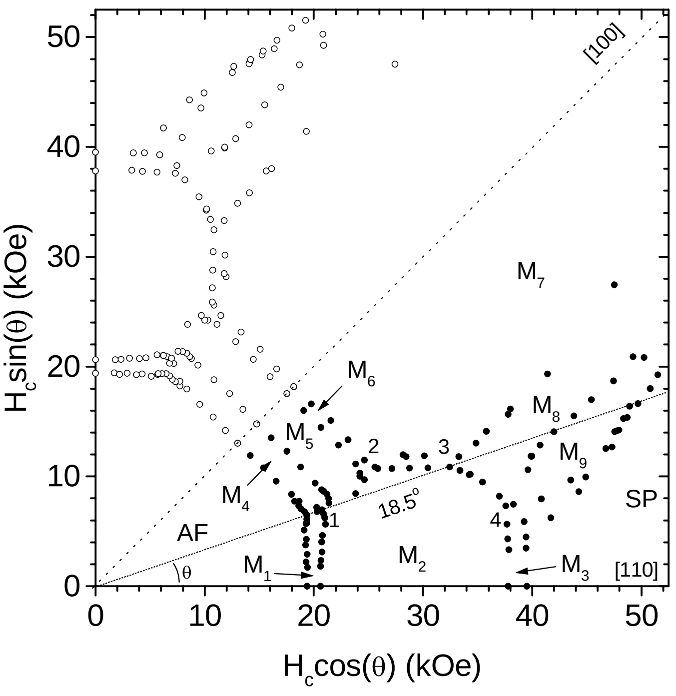

Fig. 5.8 Polar plot of the critical fields (H_c) with the metamagnetic phases labeled. Labels 1-4 represent the critical points used in the determination of the coupling constants as described in text. Note: points in upper left (○) were determined from a reflection of the measured data (●) across the [100] axis.

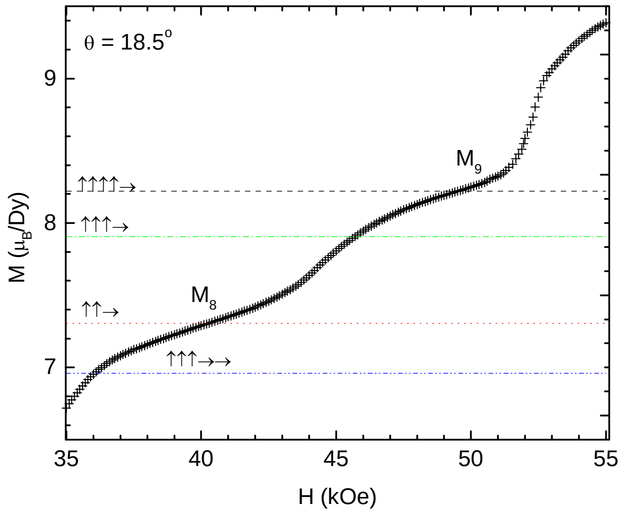

Fig. 5.9 Detail of M(H) for θ = 18.5° showing the magnetization of the M_8 and M_9 states. Lines represent calculated magnetization for the possible net distributions of moments (given by arrows) at 18.5°.

number of → moments. The next step then is to determine this distribution. Unfortunately, considerably larger slopes are present in the magnetizations of the M_8 and M_9 states, making an accurate determination of the saturated moment difficult. Figure 5.9 shows an expansion of a selected M(H) scan in this region with the calculated magnetization of some of the possible distributions of moments. If the midpoint of the magnetization plateau, between the neighboring critical fields, is used, the magnetization suggests that the net distribution of moments of M_8 and M_9 are likely given by ↑↑→ and ↑↑↑↑→, respectively. However, other distributions containing larger numbers of moments can not be ruled out.

2.18.4. Determination of Coupling Constants

A more detailed investigation into the nature of the magnetic order for each of the metamagnetic phases is possible, now that a consistent model for the net distribution of moments for each state has been determined. Within the “4-position clock model,” the Hamiltonian an arbitrary magnetic state, Φ, consisting of moments ϕ_i may be obtained by an extension of the anisotropic next-nearest neighbor Ising (ANNNI) model, to include four possible directions instead of two and interactions with more than next-nearest neighbors. We introduce the general spin-chain Hamiltonian with interactions between all spins:

$$\mathrm{H}\ (\Phi)=\sum_{n=1}^{\infty}\sum_{i=-\infty}^{\infty}\left[K_n\cos(\phi_i-\phi_{i+n})+L_n\cos 2(\phi_i-\phi_{i+n})\right]-h_x\sum_{i=-\infty}^{\infty}\cos\phi_i-h_y\sum_{i=-\infty}^{\infty}\sin\phi_i\ .$$

where K_n and L_n are coupling constants, ϕ_i represents the angular orientation of the moment (constrained to only 0, 90, 180, or 270^{o} by the CEF) of ion i, and h_x and h_y are the x and y-components of the applied field, respectively. As written, the Hamiltonian includes all spins, since the summation on n runs from 1 to infinity. With up to 3rd nearest neighbor interactions, stable phases are calculated with periods up to 6 moments, with Table 2 listing the energies of some of these metamagnetic states. For the transition from metamagnetic state Φ_1 to Φ_2, the critical field may then be given by:

$$H_{c2,1}(\theta,\Phi_1,\Phi_2)=\frac{\sum_{n=1}^{3}\sum_{i=-\infty}^{\infty}\left\{K_n\left[\cos(\phi_{i,2}-\phi_{i+n,2})-\cos(\phi_{i,1}-\phi_{i+n,1})\right]+L_n\left[\cos 2(\phi_{i,2}-\phi_{i+n,2})-\cos 2(\phi_{i,1}-\phi_{i+n,1})\right]\right\}}{\sum_{i=-\infty}^{\infty}\left[\cos(\theta-\phi_{i2})-\cos(\theta-\phi_{i1})\right]},$$

where the numerator is the energy that must be overcome, $E_{crit,}$ to stabilize the new state, as discussed previously.

Once the net distribution of moments for each state is determined, summarized in Table 5.1 it is possible to calculate the coupling coefficients, K_n and L_n, in the Hamiltonian. To do this, it is helpful to return to the polar plot of H_c (Fig. 5.8). Here, the angular dependencies are more readily seen, especially for the intermediate angles (Region II). The following series of equalities and an inequality may also be acquired from the triple points in the phase diagram, labeled 1-4 in the lower right half of the diagram.

$h_{1x} = 2(K_1 - K_2 + K_3) = 20$ kOe $h_{1y} = -4(L_1 + L_2 + L_3) = 7$ kOe
$h_{2x} = 2(K_1 + K_3) + 4L_2 = 24$ kOe $h_{2y} = 2K_2 - 4(L_1 + L_3) = 11$ kOe
$h_{3x} = 2(K_1 + K_3) - 4L_2 = 34$ kOe $h_{3y} = h_{2y}$
$h_{4x} = 2(K_1 + K_2 + K_3) = 38$ kOe $h_{4y} = h_{1y}$

In addition, since the ↑↑↓ state does not appear in the phase diagram, its energy must be greater than that for the ↑↑↑↓ state. Therefore, $(-K_1/3 - K_2/3+K_3 +L_1+L_2 +L_3-h_x/3) > (L_1 + L_2 + L_3 - h_x/2)$, gives $3K_3 > K_1 + K_2 - ½ h_{1x.}$ Finally, since the antiferromagnetic ordering is observed for zero field, K_1 must be positive.

Solving these equations yields the following coupling constants:

$K_1 = 12.25$ kOe $L_1 = -0.5$ kOe
$K_2 = 4.5$ kOe $L_2 = -1.25$ kOe
$K_3 = 2.25$ kOe $L_3 = 0$ kOe

TABLE 5.1. Net distributions of moments for all of the observed metamagnetic states and the measured angular dependence of the saturated moment for each state.

State	Net Moments	$M_{sat}(\theta)$ (μ_B)
AF	↑↓↑↓	0
F	↑↑↑↑	$10.0 \cos(\theta)$
M_1	↑↓↑↓↑↓↑↓↑↓↑	$1.0 \cos(\theta)$
M_2	↑↓↑↑	$5.0 \cos(\theta)$
M_3	↑↓↑↑↑	$5.8 \cos(\theta)$
M_4	↑↓↑↓↑→	$2.6 \cos(\theta\text{-}45^o)$
M_5	↑↓↑→	$3.5 \cos(\theta\text{-}45^o)$
M_6	↑↓↑→↑→	$4.5 \cos(\theta\text{-}45^o)$
M_7	↑→↑→	$7.2 \cos(\theta\text{-}45^o)$
M_8	↑↑↑→	7.0 ± 0.3
M_9	↑↑↑↑→	7.8 ± 0.3

TABLE 5.2. Energies of metamagnetic states.

State	Energy of the state
AF (↑↓)	$-K_1 + K_2 - K_3 + L_1 + L_2 + L_3$
SP (↑)	$K_1 + K_2 + K_3 + L_1 + L_2 + L_3 - h_x$
↑→	$K_2 - L_1 + L_2 - L_3 - ½ (h_x + h_y)$
↑↑↓	$-(K_1 + K_2)/3 + K_3 + L_1 + L_2 + L_3 – h_x/3$
↑↑→	$(K_1 + K_2 + 3K_3 - L_1 - L_2 + 3L_3 - 2h_x - h_y)/3$
↑↑↑↓	$L_1 + L_2 + L_3 - h_x/2$
↑↑↑→	$(K_1 + K_2 + K_3)/2 – (3h_x + h_y)/4$
↑↑↓→	$-K_2/2 – (h_x + h_y)/4$
↑↓↑→	$-(K_1 - K_2 + K_3)/2 – (h_x + h_y)/4$
↑↑↑↑↓	$(K_1 + K_2 + K_3)/5 + L_1 + L_2 + L_3 – 3h_x/5$
↑↑↓↑↓	$-(3K_1 - K_2 - K_3)/5 + L_1 + L_2 + L_3 – h_x/5$
↑↑→↑→	$(K_1 + 3K_2 + 3K_3 – 3L_1 + L_2 + L_3 –3h_x –2h_y)/5$
↑↑↑↑↑↓	$(K_1 + K_2 + K_3)/3 + L_1 + L_2 + L_3 – 2h_x/3$
↑↓↑→←→	$-(2K_1 - K_2 - L_1 + L_2)/3 – L_3 – (h_x + h_y)/6$

2.18.5. Theoretical Phase Diagram

Figure 5.10 shows the main features of the phase diagram calculated with these coupling constants is in good qualitative agreement with the measured phase diagram. However, the longer period phases (M_1, M_3, M_4, M_6, and M_9) are absent. In order to obtain the phases with a period greater than 6 moments, one has to include further (n > 3) interactions in the spin-chain Hamiltonian, greatly complicating the analysis. It may also be possible to use a more realistic Hamiltonian such as in (Pokrovskii, 1982), where coupling between the 2n-1 and 2n neighbors arise in the nth term of the high-temperature expansion of the free energy. In principle, the introduction of this longer-range coupling may significantly

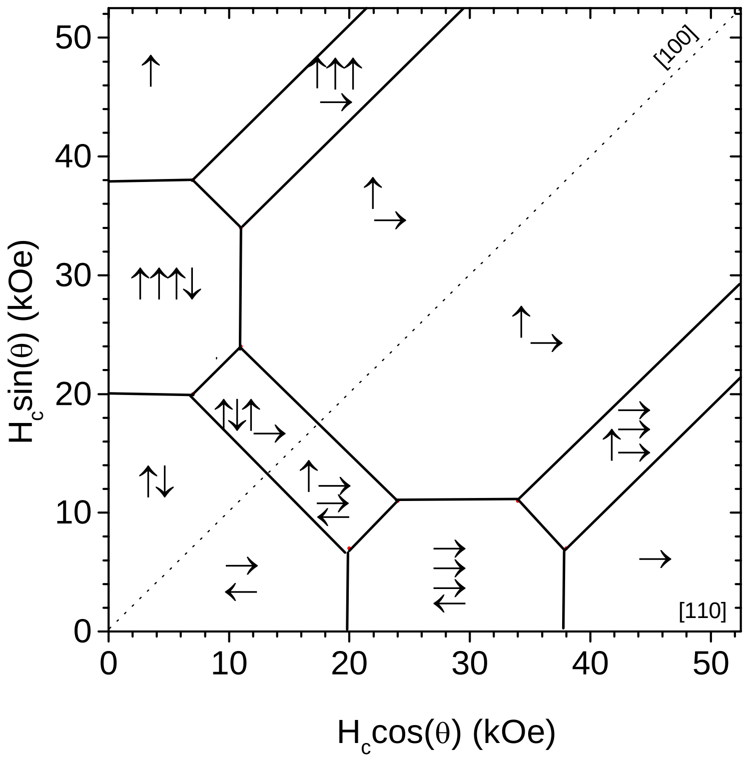

Fig. 5.10 Phase diagram determined from calculated coupling constants. Arrows represent net distributions of moments for each of the metamagnetic states and point in the actual direction of the magnetic moment.

perturb the entire calculated phase diagram, providing the energies are large enough. However, observations of the stability of the calculated phase diagram suggest that the longer-range interactions are quite small. For instance, taking $K_4 = 0.25$ kOe introduces the M_1 phase (↑↓↑↓↑↓↑↓↑↓↑) into the calculated phase diagram, with subsequent shifts of the other coupling constants by the same order of magnitude as K_4. These shifts are an order of magnitude smaller than the original values for the coupling constants, and will only affect the regions in the phase diagram near the present phase boundaries, keeping the main features of the diagram intact. Therefore, for the sake of simplicity we have refrained from considering higher order interactions.

2.19. Conclusion

We have shown that the CEF splitting of the Hund's rule ground state creates a strong anisotropy where the magnetic moment of the Dy^{3+} ions is constrained to one of the <110> orientations within the basal plane. Interactions between the Dy^{3+} ions create a rich system where up to 11 different metamagnetic states become energetically favorable, depending on the magnitude and direction of the applied magnetic field. From the angular dependence of the saturated moments of each state and the critical fields between the states, net distributions of moments may be deduced. Finally, within an extension of the ANNNI model, the "4-position clock model," the coupling constants in the Hamiltonian may be calculated from the triple points in the phase diagram.

Future work including high field magnetic measurements and neutron scattering would be useful to determine the strength of the CEF anisotropy and wave vectors associated with each of the metamagnetic states.

DE HAAS-VAN ALPHEN AND SHUBNIKOV-DE HAAS OSCILLATIONS IN $RAgSb_2$ (R = Y, La, Pr, Nd, Sm)

Introduction

Although the magnetic and transport properties of the tetragonal $RAgSb_2$ compounds have been carefully studied, very little is known of the electronic structure. The observation of quantum oscillations in the magnetization and resistivity allows a first investigation of the Fermi surface. The frequencies of these oscillations reveal the area of extremal cross sections of the Fermi surface. Careful study of the angular dependence of the frequency may be used to determine the shape of the Fermi surface. Finally, the effective masses of the electrons may be determined from the temperature dependence of the amplitudes of the oscillations.

After a brief presentation of the experimental methods specific to the investigation of the quantum oscillations, data will be presented on the frequency spectra of de Haas-van Alphen and Shubnikov-de Haas oscillations in the $RAgSb_2$ series for R=Y, La, Pr, Nd, and Sm. The calculated Fermi surface will be used to discuss the origin of the various observed frequencies and their angular dependence. Finally, the temperature dependence of the oscillations will be used as a probe of the effects of magnetic order on the electronic structure of the compounds.

Experimental Details

The magnetization measurements were performed in a Quantum Design SQUID magnetometer up to 55 kG, with the samples manually aligned. Samples were carefully chosen on the basis of size and geometry and to minimize the effects of any residual flux on the surface. Angular dependent torque measurements were performed in a Quantum Design Physical Property Measurement System (PPMS) up to 90 kG, using the torque magnetometer and horizontal rotator options. Uncertainty in the angular position is estimated to be less than one degree. Due to the larger magnetic moments and strong anisotropies in $NdAgSb_2$ and $PrAgSb_2$ (Chapter 4), these samples were unsuitable for measurements in the PPMS.

Resistivity measurements used the temperature-field environment of the magnetometer, with a Linear Research LR-400 AC resistance bridge. A wire saw was used to cut the crystals into suitable geometry for resistance measurements with typical dimensions of 1 x 1 x 5 mm. Contacts were attached with Epotek-H20E silver epoxy, yielding typical contact resistances of about 1 Ω.

In all cases, the quantum oscillations were separated from the background magnetization or magnetoresistance by subtracting either a power law or a polynomial fit of the M(H), τ(H), or ρ(H) data. Microcal Origin was used to create the Fast Fourier transforms (FFT) of the data, after the background was subtracted. When possible, the data were acquired with varying applied field intervals such that the intervals in H^{-1} were constant. When this is not possible, such as the measurements in the PPMS, an interpolation routine was used to generate constant H^{-1} intervals. The number of points used in interpolation method was adjusted to check for any artifacts appearing in the FFT.

Data and Analysis

$YAgSb_2$

Exceptionally clear oscillations are observed in the applied field-dependent torque of $YAgSb_2$ at 2 K, shown in Figure 6.1. The inset to Fig. 6.1 provides a detailed view of the torque as a function of inverse field between 66.7 and 90 kOe. The two frequencies clearly observed in the torque data correspond to strong peaks in the Fourier spectra [Fig. 6.2 (a)] at 0.86 MG (β) and 10.04 MG (δ). Smaller signals are also present at frequencies of 0.65 MG (α) and 1.82 MG (γ).

The temperature (T) dependence of the amplitudes (A) of these frequencies, shown in the inset of Fig 6.2 (a), may be used to determine the effective mass of the orbits via the Liftshitz-Kosevich (LK) formula, as described in Chapter 3. From the slope of ln(A/T) plotted as a function of temperature, the effective masses were found to be $m_\beta = 0.16 \pm 0.02$ m_0, $m_\gamma = 0.28 \pm 0.02$ m_0, and $m_\delta = 0.46 \pm 0.02$ m_0, where m_0 is the bare electron mass.

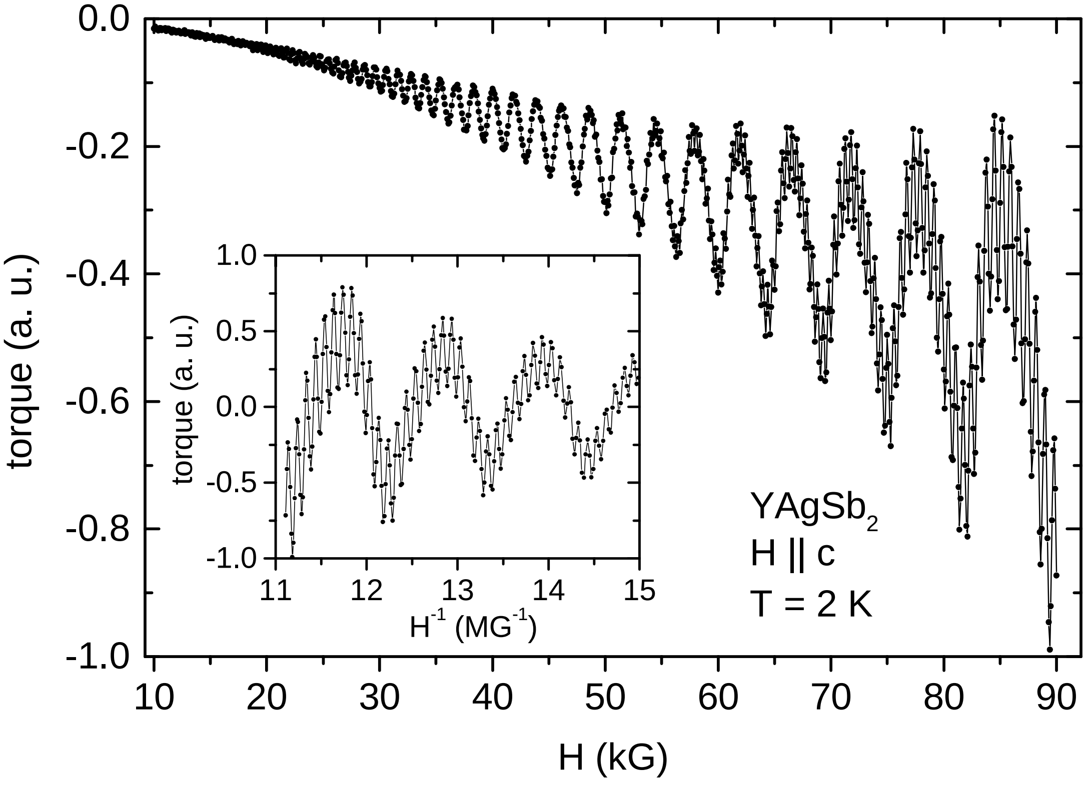

Fig. 6.1 Torque as a function of applied field in $YAgSb_2$ at 2 K for H || c. Inset: detailed view of the torque as a function of H^{-1} between 60 and 90 kG.

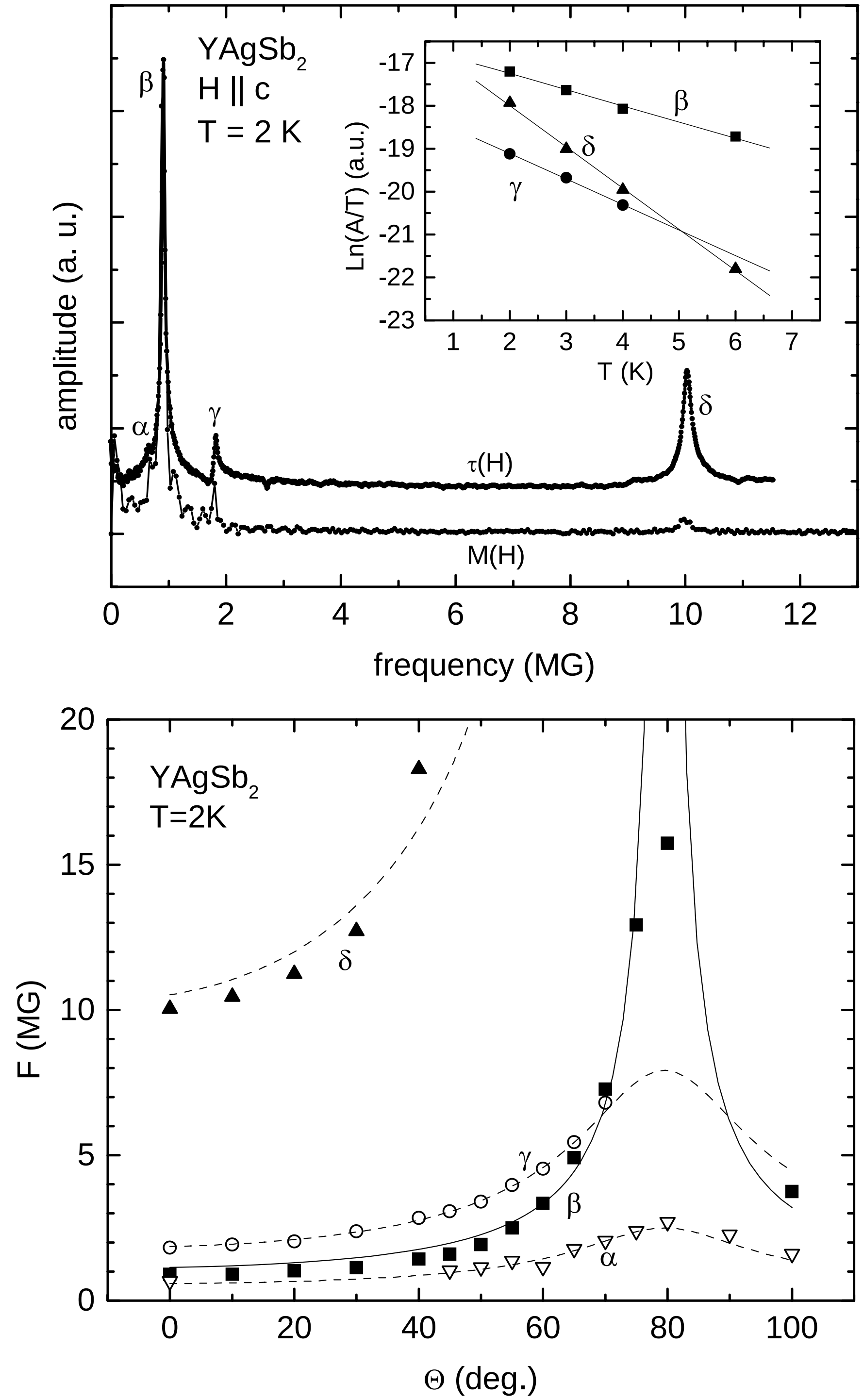

Fig. 6.2 (a) Fourier spectrum of the oscillations in YAgSb$_2$ for H || c at 2 K, Inset: Temperature dependence of the amplitudes of the observed oscillations. (b) angular dependence of the frequencies. θ is relative to the c-axis. The lines are fits to the cross sectional areas of a cylinder (β and δ) and an ellipsoid (α and γ).

An estimate of the topology of the Fermi surface may be obtained from the angular dependence of the frequencies of each quantum oscillation. As seen in Fig.6.2(b), the frequencies of the α and γ orbits do not diverge with increasing angle and may be fit to the angular dependence of the cross section of an ellipsoid. On the other hand, the frequencies of the β and δ orbits appear to diverge with increasing angle and may be fit to the angular dependence of the cross sectional area of a cylinder. In all cases, the frequencies, and hence cross sectional areas, are a minimum when the applied field is parallel to the c-axis of the sample.

$LaAgSb_2$

The torque as a function of applied field of $LaAgSb_2$ at 2 K and H || c is shown in Fig. 6.3 with the a detailed view of the oscillations at high fields, as a function of inverse field, displayed in the inset. Although this plot is more complicated than that observed in $YAgSb_2$, the frequencies of these oscillations are clearly resolved in the FFT [Fig. 6.4(a)]. Large peaks are present in the spectra at 1.64 MG (β), 4.32 MG (γ) and 12.9 MG (δ). In addition, weak peaks in the FFT indicate the presence of oscillations with frequencies of 0.72 MG (α), 3.22 MG (2β), 4.94 MG (3α), and 15.69 MG.

The effective masses, calculated from the temperature dependence of the amplitude of the oscillation [inset Fig. 6.4(a)], are $m_\beta = 0.16 \pm 0.02\ m_0$, $m_{2\beta} = 0.32 \pm 0.02\ m_{0,}$ $m_\gamma = 0.28 \pm 0.02\ m_0$, and $m_\delta = 0.42 \pm 0.02\ m_0$. Since the frequency and effective mass of the 2β orbit are twice that of the β orbit, it is concluded that the 2β is the first harmonic of the β orbit. Likewise, the frequency of the 3β orbit suggests that it is the third harmonic of β.

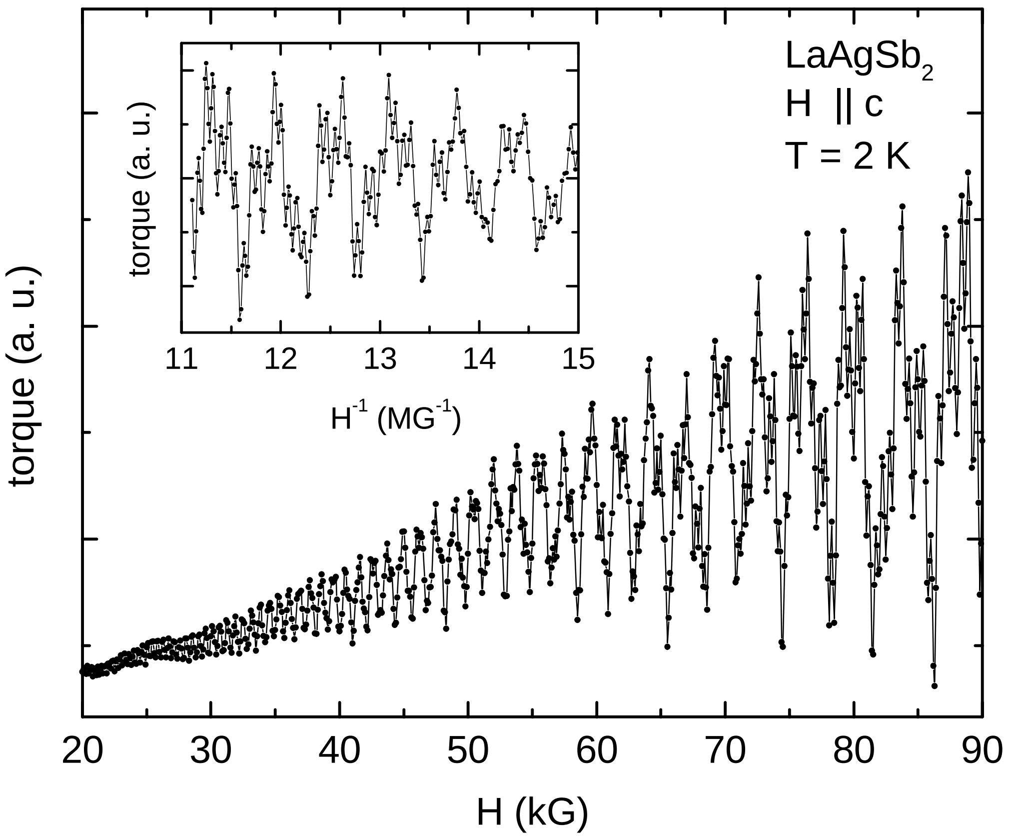

Fig. 6.3 Torque as a function of applied field in LaAgSb$_2$ at 2 K for H || c. Inset: detailed view of the torque as a function of H^{-1} between 60 and 90 kG.

The angular dependence of the frequencies of the oscillations in LaAgSb$_2$ [Fig. 6.4(b)] is similar to that observed in YAgSb$_2$. The frequency corresponding to each of the orbits is minimal for H || c and increases as the angle increases. The angular dependencies of the β and the δ family of orbits suggest the topologies of these parts of the Fermi surface are primarily ellipsoidal with the major axis parallel to the c-axis. The angular dependence of the 2β and 3β orbits is consistent with harmonics of the β orbit. On the other hand, the γ orbit diverges more rapidly as the angle approaches 90º, suggesting a cylindrically shaped section of Fermi surface.

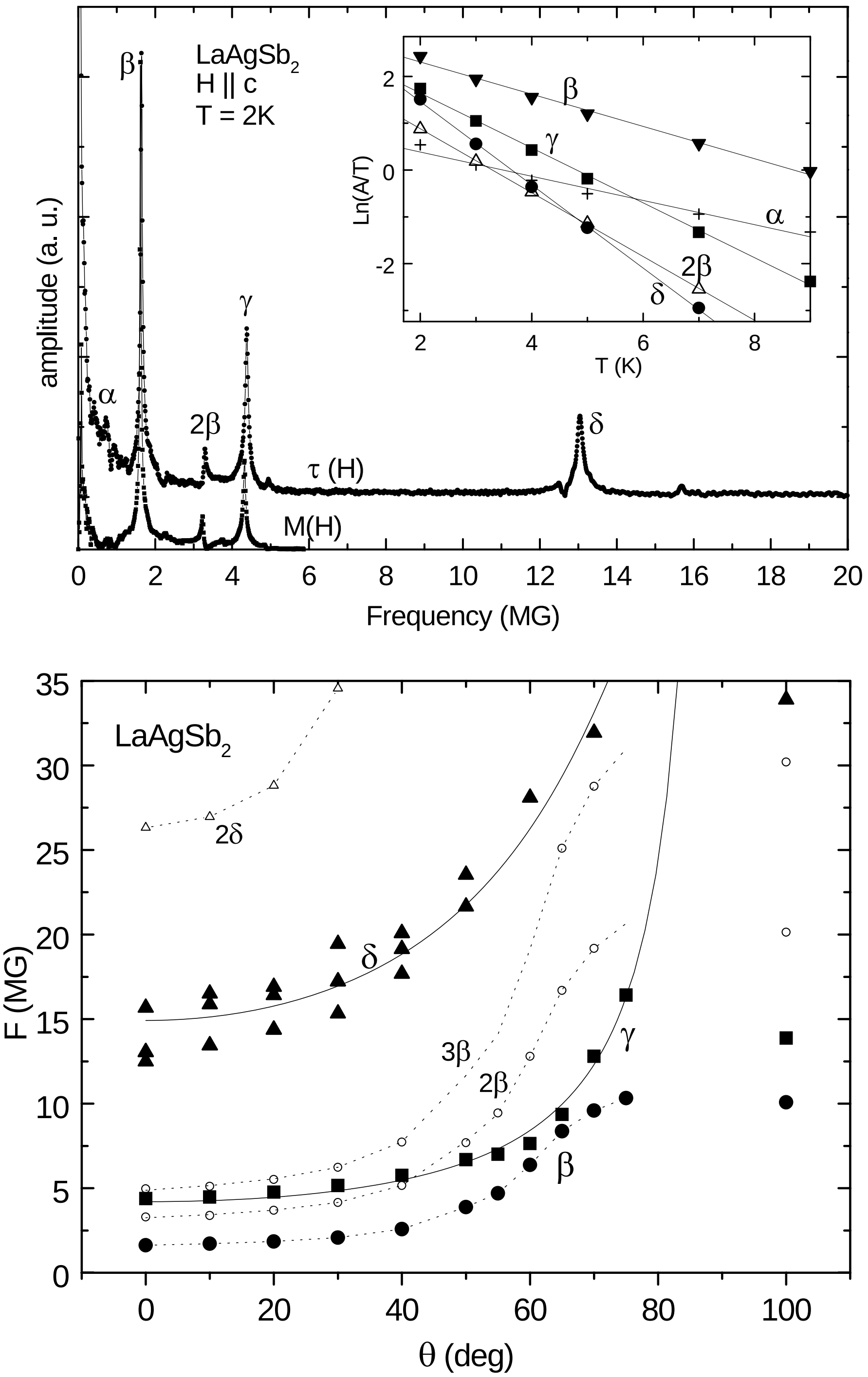

Fig. 6.4 (a) Fourier spectrum of the oscillations in the torque and magnetization of LaAgSb$_2$ for H || c at 2 K, Inset: Temperature dependence of the amplitudes of the observed oscillations. (b) Angular dependence of the frequencies. θ is relative to the c-axis. The solid lines are fits to the cross sectional areas of a cylinder (γ) and an ellipsoid (δ). Dotted lines are guides to the eye.

$PrAgSb_2$

For H || c at 2 K, de-Haas-van Alphen oscillations were observed, superimposed on the nearly linear magnetic background of $PrAgSb_2$. Due to the much larger response of the magnetic moments to the applied field, the signal to noise ratio of the dHvA oscillations suffers in this compound. Despite this significant magnetic background, Fourier analysis of the M(1/H) data (inset, Fig. 6.5) reveals 3 peaks in the spectrum (Fig. 6.5): a strong peak (α) at 0.46 MG, and weak peaks at 0.92 MG (2α) and 1.38 MG (β). The peak in the FFT below the α peak is an artifact of the background subtraction and depends strongly on the method used to remove the contribution from the magnetic sublattice (Fig. 4.10). Since the frequencies of the 2α and β peaks are twice and three times the frequency of the α

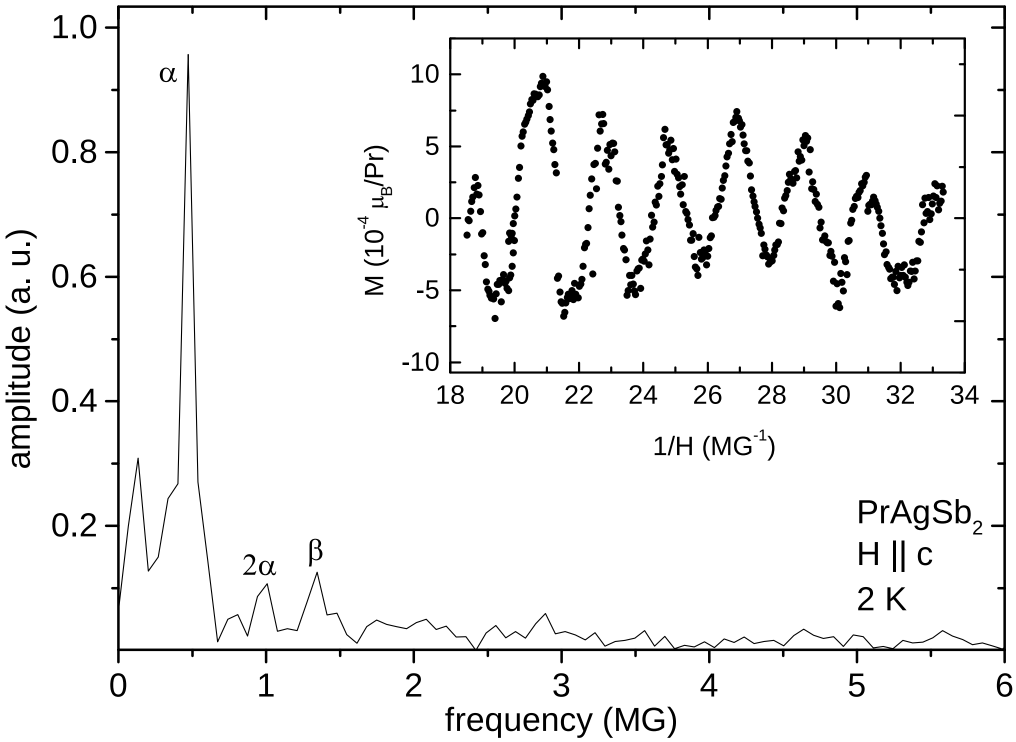

Fig 6.5 Fourier spectrum of de Haas van Alphen oscillations in $PrAgSb_2$. Inset: Magnetization as a function of H^{-1} after the removal of the magnetic background.

oscillation, these are possibly harmonics of α. However the amplitude of β is larger than 2α, indicating this may be due to the observation of a different part of the Fermi surface. Unfortunately, the magnitudes of the oscillations are insufficient for a detailed analysis of the temperature dependence of the amplitudes or the angular dependence of the frequencies. Either of these methods would help to resolve the ambiguity of the β component.

NdAgSb$_2$

The oscillations observed in NdAgSb$_2$ are of the same order of magnitude to those observed in PrAgSb$_2$ with an approximate amplitude of 10^{-3} μ_B per formula unit at fields near 50 kG. However, the background magnetization at 2 K for H || c is only about 20% of that observed in PrAgSb$_2$, creating a more favorable signal to noise ratio. The oscillations are readily observed in M(1/H) (inset Fig. 6.6). Two peaks are visible in the Fourier spectrum (Fig. 6.6) indicating the presence of frequencies at 0.56 MG (α) and 1.13 MG (2α). The

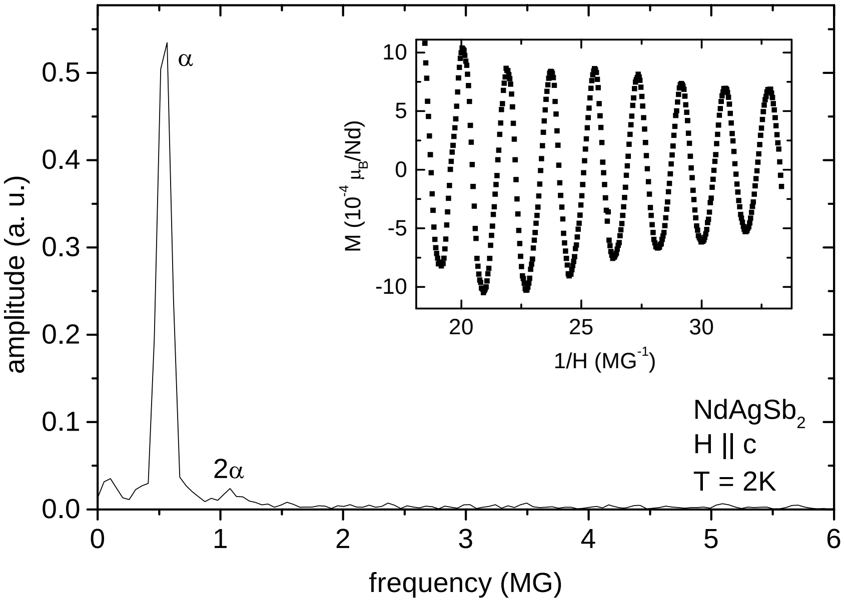

Fig 6.6 Fourier spectrum of de Haas van Alphen oscillations in NdAgSb$_2$. Inset: Magnetization as a function of H^{-1} after the subtraction of the magnetic background.

small maximum in the FFT at very low frequencies changes according to the method of background subtraction and therefore is not likely to originate from a quantum oscillation. The oscillations were of sufficient amplitude to allow an estimation of the effective masses of the electronic bands, through the temperature dependence. Fitting the data to the LK equation yields an effective of the α orbit of 0.07±0.02 $m_{0.}$ The effective mass of the 2α peak was found to be 0.17±0.02 m_0, which is twice the effective mass of α within experimental uncertainty.

SmAgSb$_2$

SmAgSb$_2$ is an ideal compound to study the effects of antiferromagnetic ordering on the Fermi surface. The magnetic ordering temperature is large enough (T_N = 8.8 K) to allow detailed study of the frequencies and their amplitudes in the ordered state. Oscillations are also observed well above T_N, which permits the comparison with the low temperature data. Furthermore, the single crystals of SmAgSb$_2$ have the smallest residual resistivity of the RAgSb$_2$ series, and hence, would be expected to demonstrate quantum oscillations with the largest amplitude. Figure 6.7 (a) shows these oscillations in the magnetization for H || c persisting up to temperatures of 20 K. Oscillations in the resistivity are also clearly resolved after the subtraction of the background, as seen in Fig. 6.7 (b).

The spectrum of oscillations observed in SmAgSb$_2$ for H || c at 2 K [Fig. 6.8(a)] is much more complicated than those observed in the other members of the series. In the torque data up to 90 kG [inset, Fig. 6.8 (a)], strong peaks are present at 0.54 MG (α), 0.87 MG (β), and 2.05 MG (ε). Much weaker peaks in the torque data exist at 0.13MG (θ), 1.62 MG (2β), 2.76 MG (2β), 3.53 MG (4β), 4.14 (2ε), 6.17 MG (ζ), 8.97 (η), and 10.13 MG (δ).

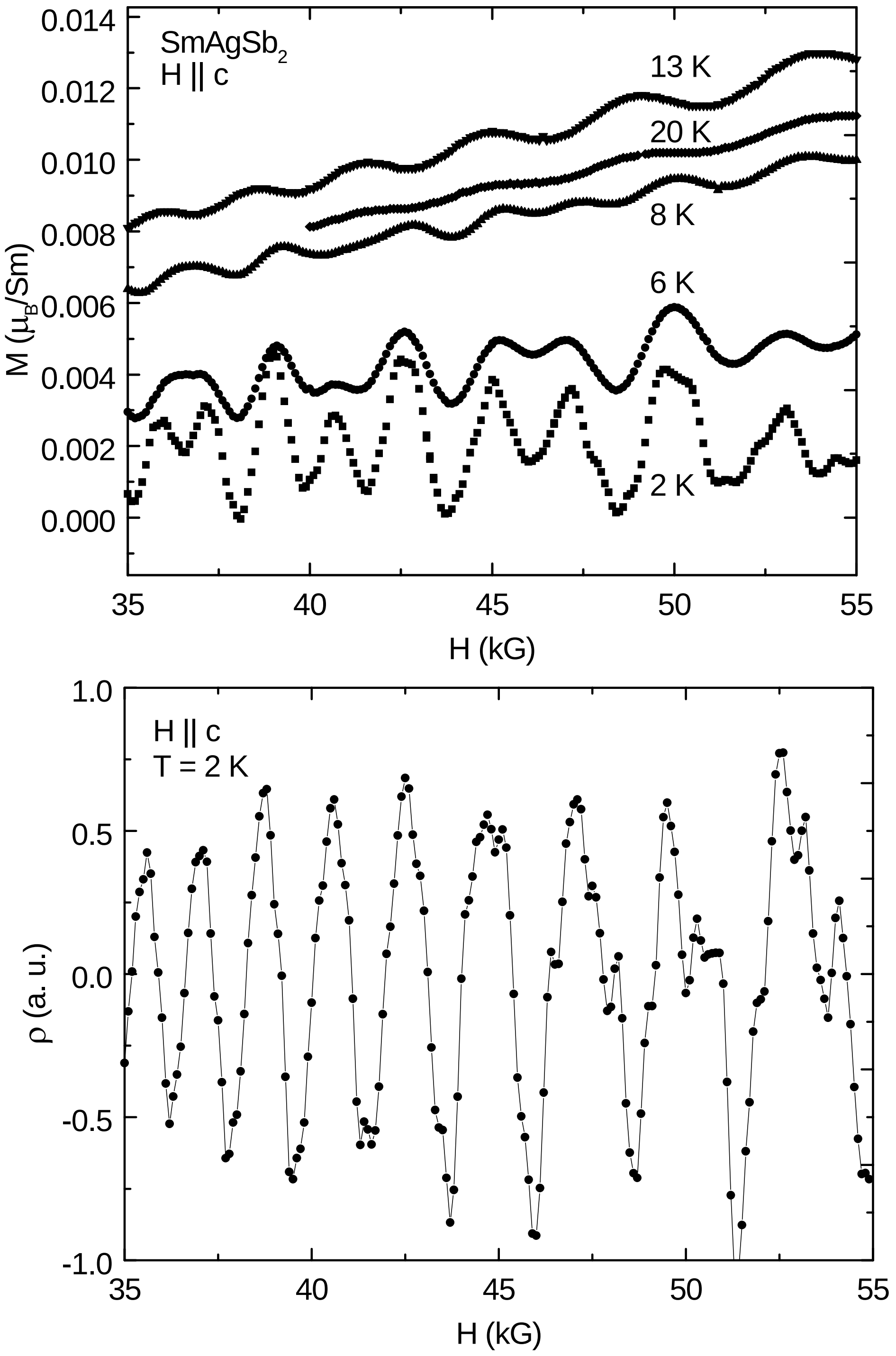

Fig. 6.7 (a) Magnetization as a function of applied field in SmAgSb$_2$ up to 20 K. Note that oscillations are still readily visible at 20 K and the magnetic background is consistent with the temperature dependent magnetization in Fig. 4.14 (a). (b) Resistivity as a function of applied field. Note that the background magnetoresistance has been subtracted.

The Fourier spectra of the magnetization and resistivity data up to 55 kG are similar to the FFT of the torque data. However, the ε oscillation is significantly suppressed relative to the other oscillations, in both M(H) and ρ(H), and the α oscillation is weak in ρ(H). The η and δ orbits are not visible in the FFT of either ρ(H) or M(H), probably due to the lower maximum field attainable in the MPMS.

The observation of additional oscillations in $SmAgSb_2$ may be the result of two different factors. First, the residual resistivity in $SmAgSb_2$ is significantly lower than in the other members of the series. This allows the higher frequency oscillations to be observed at much lower fields, via a reduction in the Dingle temperature. Second, $SmAgSb_2$ orders antiferromagnetically at 8.8K, as determined by the temperature dependent susceptibility and resistivity [Fig 4.14(a)]. The new periodicity due to the wavevector of antiferromagnetic ordering may significantly perturb the Fermi surface and create new extremal orbits. Unfortunately, the exact nature of the ordered state, such as the wave vector is not known, which prevents an accurate determination of the electronic band structure in the ordered state.

The angular dependence of the observed frequencies [Fig. 6.8(b)] is also more complex than any of the other compounds studied here. The frequencies of the α, β, and θ oscillations are minimal at H || c and increase with increasing angle. None of these frequencies diverge with increasing angle, suggesting the presence of ellipsoidally shaped sections of Fermi surface. Fitting these data to the cross section of an ellipse gives c/a ratios of 4.3, 4.0 and 10.8 for the α, β, and θ oscillations, respectively. The ε, λ, and κ frequencies also appear to be predominately ellipsoidal at low angles. However, these orbits are not observed at large enough angles to accurately determine the topologies of the Fermi surface.

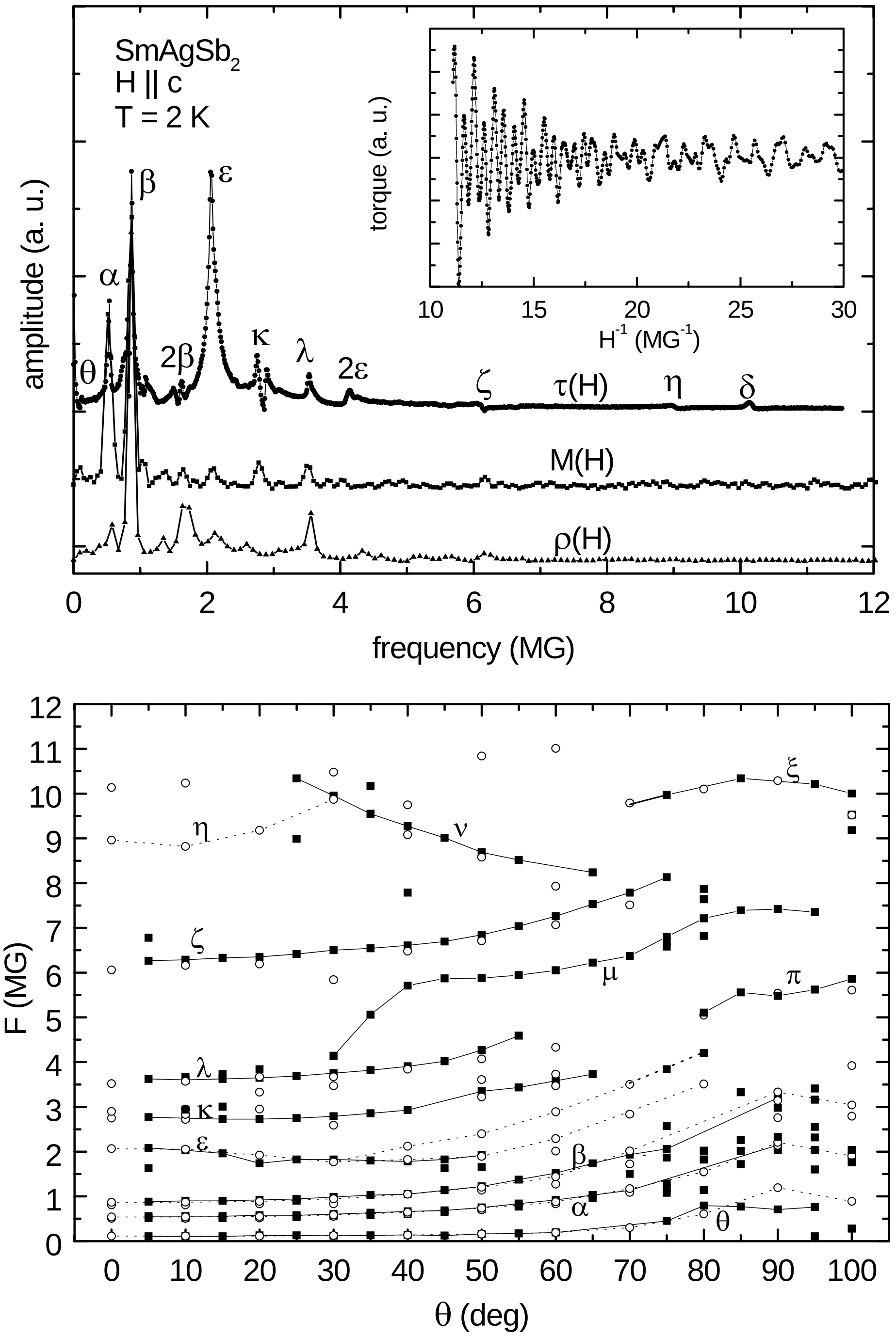

Fig. 6.8 (a) Fourier spectrum of the oscillations in the torque and magnetization of SmAgSb$_2$ for H || c at 2 K, Inset: Temperature dependence of the amplitudes of the observed oscillations. (b) Angular dependence of the frequencies measured by torque magnetometry (○) and magnetization (■). θ is relative to the c-axis. The solid and dotted lines connect the frequencies observed in the torque and magnetization data, respectively.

The frequency of the ζ oscillation is nearly constant with increasing angle, which indicates the existence of a nearly spherical section of Fermi surface. Finally, additional frequencies, denoted μ, ν, ξ, and π, appear at intermediate angles. The origins of these frequencies are currently unknown and are the subject of continuing investigation.

The effect of the magnetic phase transition is particularly evident in the temperature dependence of the amplitude of the oscillations. As seen in Fig.6.9, the temperature dependence of the dHvA oscillations for H || c significantly deviates from the expected Lifshitz-Kosevitch (LK) behavior, with an anomalous suppression of the dHvA amplitudes near T_N. Specifically, the amplitude of the α orbit decreases sharply as the temperature approaches T_N. Above T_N, the amplitude partial recovers, and may easily be fit to the LK

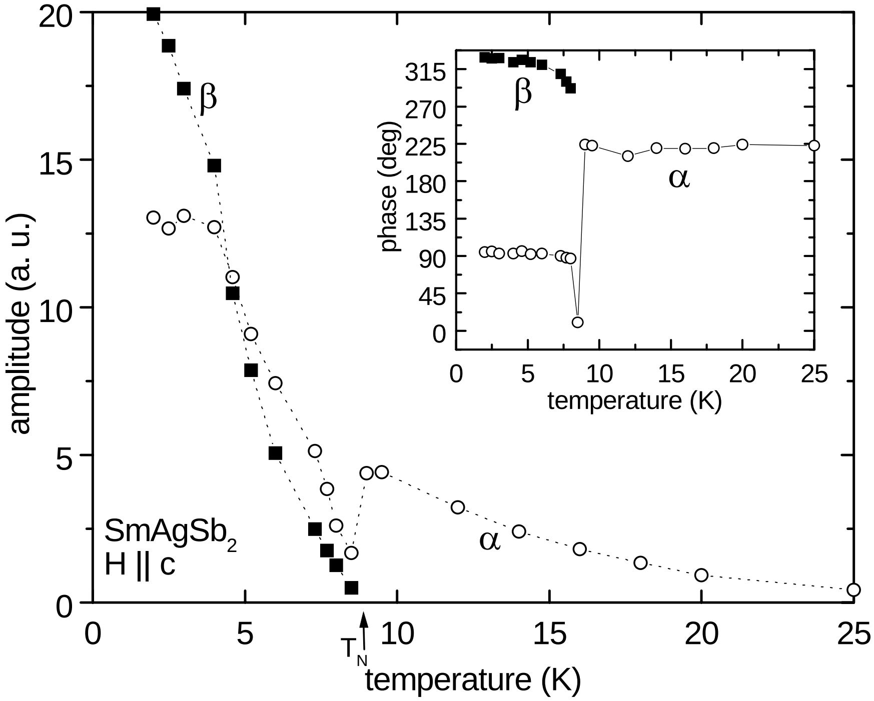

Fig. 6.9 Temperature dependence of the amplitudes of the α and β oscillations in $SmAgSb_2$. Inset: temperature dependence of the relative phase of the oscillations. Note the suppression of the α amplitude and discontinuity in the phase at T_N=8.8 K.

equation. Fitting this data above T_N yields an effective mass of the α orbit of $0.06\pm0.01\ m_0$, consistent with the rest of the $RAgSb_2$ series. Likewise, the amplitude of β orbit (0.87 MG) decreases as the temperature approaches T_N with no observation of this signal above T_N. Below T_N, the fit of the temperature dependence to the LK equation is poor, suggesting that the magnetic ordering is influencing the amplitude. Although the β orbit is only observed below T_N, it is currently impossible to determine whether this is due to a new section of Fermi surface below T_N or increased scattering and broadening of the Fermi surface with increasing temperature.

As seen in Fig. 4.14 (b), the resistivity of $SmAgSb_2$ increases near T_N, due to the introduction of spin-disorder scattering in the paramagnetic state. It is possible that the additional scattering in the paramagnetic state increases the Dingle temperature, and hence, suppresses the amplitude. However, if the deviation from the LK behavior were due entirely to the increased scattering from the addition of a magnetic component, it is unlikely that the amplitude of the α oscillation would actually increase between T_N and 10 K.

When the magnetic sublattice in a compound becomes antiferromagnetically ordered, new periodicity is introduced into the lattice with the wavevector of the magnetic ordering. This extra periodicity may significantly perturb the Fermi surface by rearranging the sections of the Fermi surface and introducing superzone gaps (Miwa, 1963; Elliot (1963). These effects may be responsible for the appearance of new frequencies below T_N, and the phase change and the anomalous behavior in the amplitude of the α oscillation. However, without explicit knowledge of the ordering wavevector and the band structure of the ordered state, a quantitative analysis of these effects is difficult.

The perturbation of the Fermi surface may account for the temperature dependence of the amplitude in several ways. First, the magnetization M is proportional to $(A'')^{-(1/2)}$, within the LK expression (Eq. 3.52), where A" is the second derivative of the cross sectional area with respect to the wave vector in the direction of the applied field. Increasing this curvature, while keeping the extremal cross sectional area constant, will diminish the amplitude of the measured oscillation. Second, electron-electron scattering may increase in the magnetically ordered state. Although electron-electron scattering does not generally affect the resistivity, it may be much more important in studies of dHvA effect through the scattering of carriers out of the observed band due to the close proximity of perturbed sections of Fermi surface. Since no changes in frequency are readily observable for the α oscillation, most likely another, not observed, band is affected by the antiferromagnetic ordering. This band, in turn, may be mapped into a different part of the Brillouin zone, and hence, indirectly affect the carrier-carrier scattering. This effect would decrease at lower temperatures (Eq. 3.39) due to the decrease in thermal broadening of the Fermi surface.

The effect of magnetic ordering may also be seen in a shift in the relative phase of the α oscillation above and below T_N as seen in the M(1/H) data (inset Fig 6.9). Since the frequency of the oscillation is constant, within experimental resolution, above and below the transition, this phase shift may result from the perturbation of the Fermi surface due to a new periodicity arising from the magnetic ordering. The section of Fermi surface would have to altered in such a way that the cross sectional area remains constant, but the extremal orbit changes from being a minimum to a maximum, or vice versa. This effect may be seen within the LK expression (Eq. 3.52), where the relative phase difference between a maximal and minimal orbit is 90º, which is approximately the phase shift observed in the data.

Analysis

Band Structure of $LaAgSb_2$ and $YAgSb_2$

Ab initio local density approximation (LDA) electronic bands of $YAgSb_2$ and $LaAgSb_2$ were calculated using the tight-binding, linear muffin tin orbital (TB-LMTO) method within the atomic spheres approximation (ASA) developed by O. K. Andersen (1985). Interstitial spheres were added to fill empty parts of the cell. The 4f electrons in Pr, Nd, and Sm are not expected to significantly contribute to the electronic structure since these electrons are strongly localized and well screened. Therefore, these electrons may be considered part of the electronic core. This implies that the Fermi surfaces of the rest of the $RAgSb_2$ series are expected to be closely similar to those obtained for $YAgSb_2$ and $LaAgSb_2$.

Figure 6.10 shows the electronic structure of $YAgSb_2$ and $LaAgSb_2$ along several high symmetry directions. Relevant features of these plots include two bands crossing E_F near the Γ point and the two bands crossing E_F near the X point. In addition, another band crosses E_F between Γ and Z. This band is particularly important since it possesses very little curvature, and hence may lead to dramatic changes of the topology of the Fermi surface with small changes in lattice parameters or Fermi energy. Figure 6.11 shows the Fermi surface in the $k_z= 0$ plane of the four bands the cross the Fermi energy with the Brillouin zone of a primitive tetragonal lattice displayed in the inset.

Three dimensional plots of the calculated Fermi surface of $LaAgSb_2$ are shown in Fig. 6.12 (a-d). Band 1 is centered at the Γ point and is nearly spherical, with a cross sectional area in the basal plane corresponding to a frequency of approximately 4.7 MG for $H \parallel c$. The γ orbit, observed in $SmAgSb_2$ and $LaAgSb_2$ has a frequency of approximately 4.3 MG.

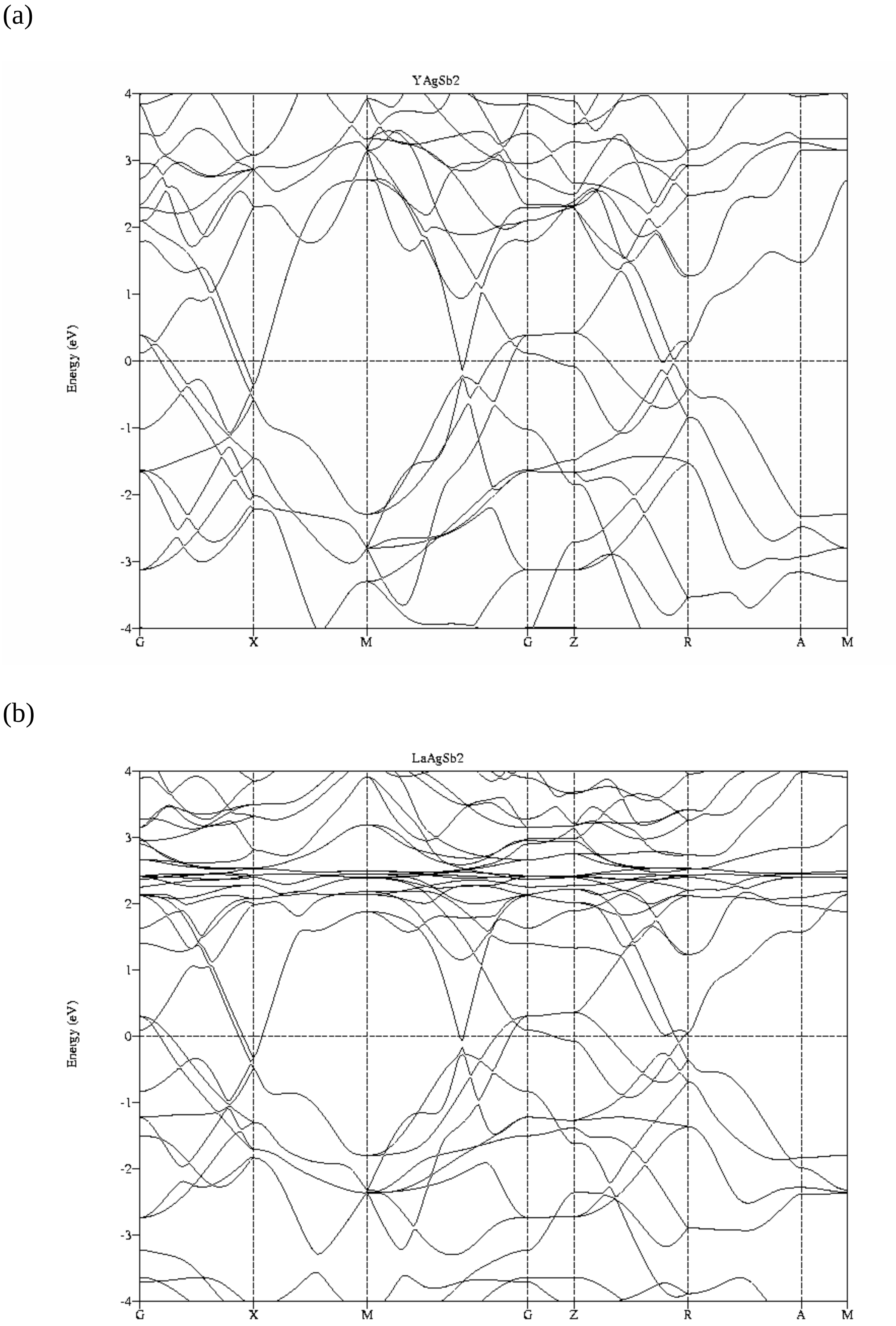

Fig. 6.10 Band Stucture of (a) $YAgSb_2$ and (b) $LaAgSb_2$ calculated from tight binding linear muffin tin orbital calculations within the atomic spheres approximation.

In $LaAgSb_2$, the angular dependence of this frequency is nearly constant for low angles, relative to H || c, which is consistent with the calculated band. However, at higher angles, the frequency appears to diverge, indicating non-spherical behavior. Figure 6.13(a), shows constant energy surfaces of this band in the k_x- k_z plane, centered at the Γ point. If the Fermi energy is increased by approximately 50 meV, the topology of this band changes dramatically with the appearance of thin necks connecting this band to the next Brillouin zone. This modified band is now much more consistent with the observed angular dependence of the γ frequencies. Although the cross sectional area for H || c does not depend strongly on the E_F, this band may also be the origin of the ζ oscillation (6.2 MG) in $SmAgSb_2$ which is nearly spherical. Furthermore, the necks may also help to account for the extremely

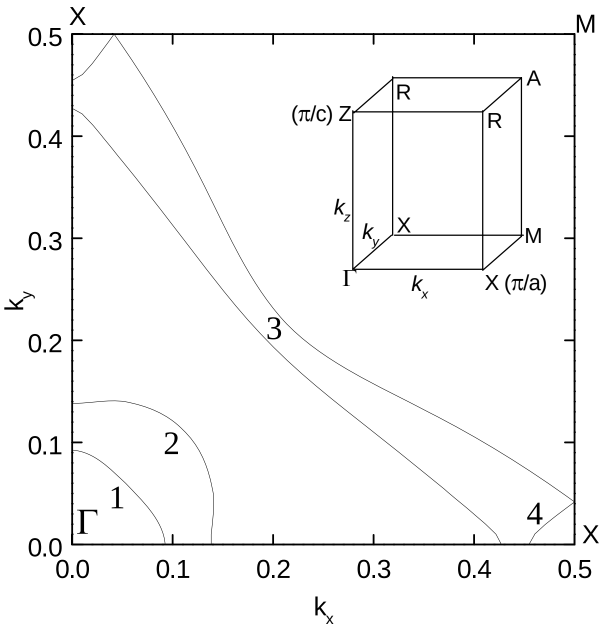

Fig. 6.11 The Fermi surface of $LaAgSb_2$ in the $k_z = 0$ plane, calculated as described in the text. The four bands crossing E_F are labeled 1-4. Inset: the Brillouin zone of a primitive tetragonal lattice with the high symmetry points labeled.

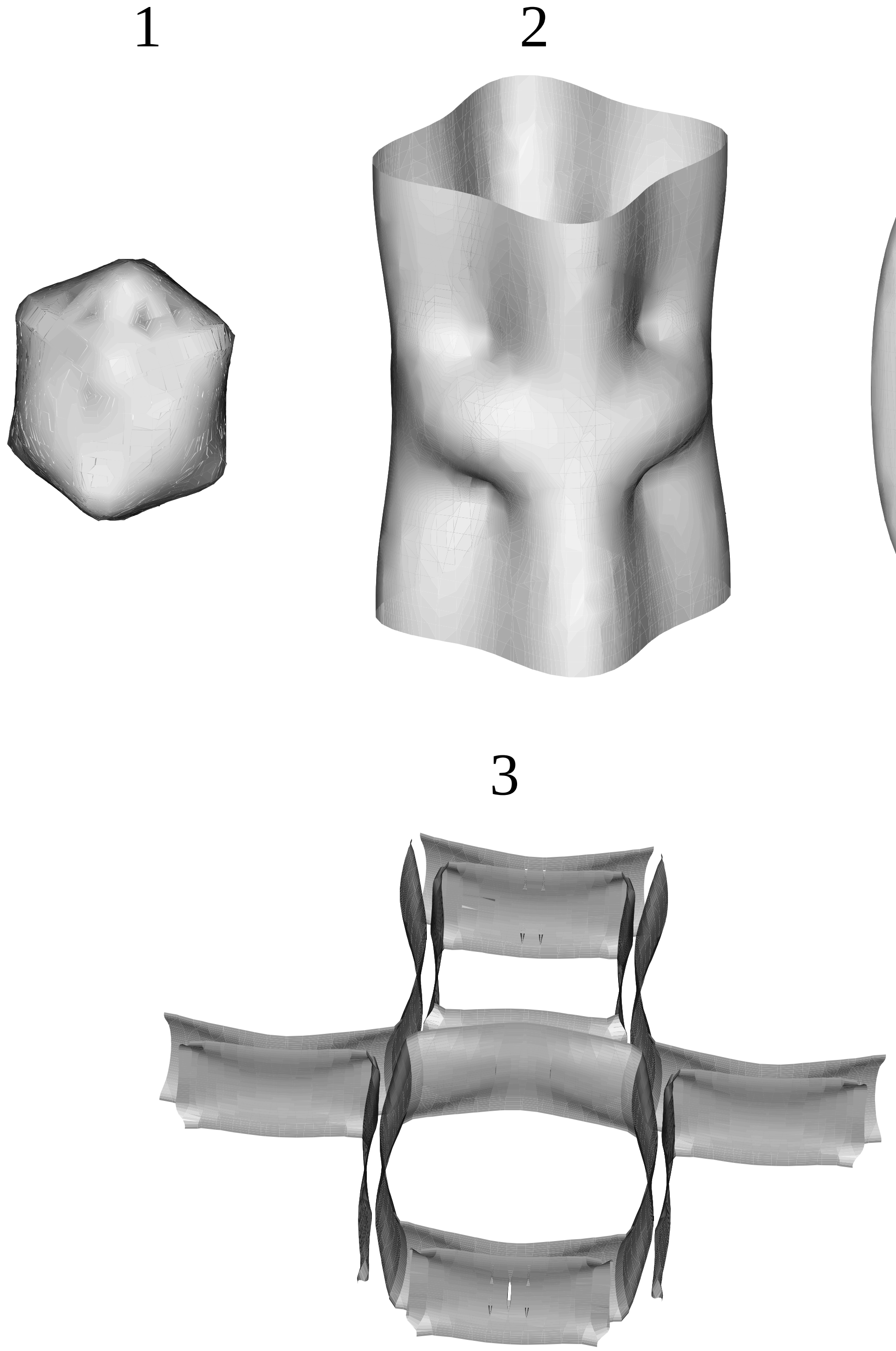

Fig. 6.12 3-dimensional plots of the 4 bands crossing the Fermi surface. Bands 1 and 2 are centered at Γ. Band 4 is centered at X. Band 3 extends throughout the zone. In this figure the Γ point is at the center of the lower square. The vertices of the squares are at the X points.

approximately corresponds to the α orbits (0.55 MG) the angular dependence is not is good agreement, since the α orbits appear to be ellipsoidal. Better agreement is found in the sectional area of the necks for H || c θ orbit of $SmAgSb_2$ which has a frequency of 0.13 MG and a shape corresponding to either a cylinder or an elongated ellipsoid with a c/a ratio near 10.

Band 2 is also centered at Γ, but is mostly cylindrical with an axis along k_z, This energy band possesses a nearly circular cross section at $k_z = 0$ and a somewhat square cross section at $k_z = \pi/c$. Maximal cross sectional areas for H || c correspond to frequencies of 13.2 and 11.5 MG for k_z =0 and π/c, respectively. A minimal area is also observed for $k_z \approx 0.4 \pi/c$ with a frequency of 9.7 MG. These frequencies are approximately equal to the δ frequencies observed in some of the compounds. ($F \approx 10.1$ MG for $SmAgSb_2$, 10.04 MG in $YAgSb_2$, and 12.5 MG, 12.9 MG and 15.7 MG in $LaAgSb_2$). In $SmAgSb_2$ and $YAgSb_2$, the frequency of the δ orbit diverges with small frequencies observed for H || c in a most of the compounds. Although the cross increasing angle away from H || c. However, the angular dependence of δ family of orbits in $LaAgSb_2$ is more closely ellipsoidal than cylindrical, possibly due to significant changes in the Fermi surface corresponding to the resistivity anomaly at 210 K (Fig. 4.3a). Taken together, the topology and cross sectional areas for H || c suggest that this band is the origin of the δ orbits observed in the magnetization and torque data. The effective masses of each of the observed frequencies for H || c are approximately 0.46 m_0 in $YAgSb_2$ and 0.42 m_0 in $LaAgSb_2$.

Band 3 consists of adjacent square cylinders with vertices near each of the X points.

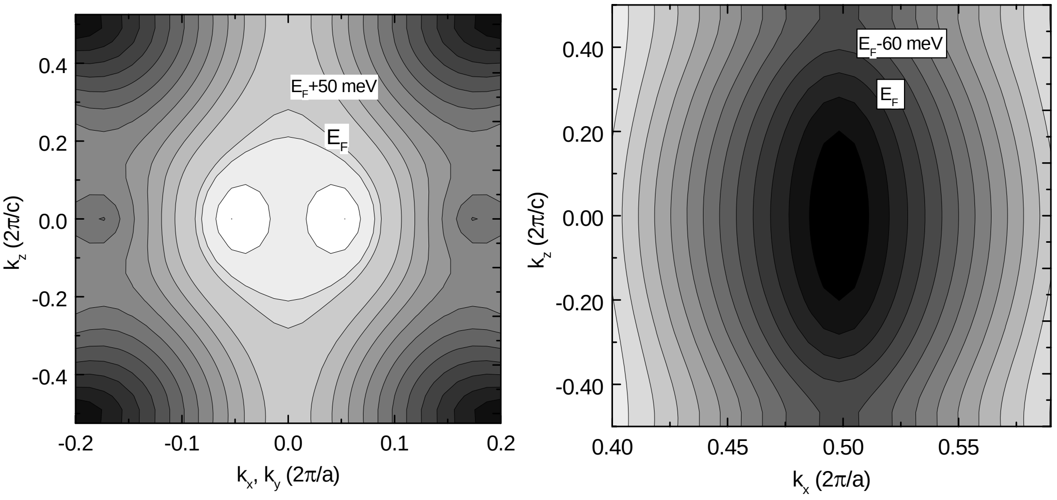

Fig. 6.13 Constant energy contours in the k_x-k_z plane for bands 1 (a) and 4 (b). The difference in energy of the contours is 50 meV..

One square cylinder is centered at Γ, and the other is centered the M point. Due to the extremely large cross sectional areas, it is not expected that any of the features of this band would be visible in the relatively low fields currently accessible. However, it should be noted that at very high fields, the close proximity of these surfaces may result in magnetic breakdown.

An ellipsoidal hole pocket centered at the X point in the Brillouin zone is created by band 4. The cross sectional area of this band for $H \parallel c$ is maximal at $k_z=0$ and predicts the presence of a frequency of 0.9 MG. For $H \perp c$, the maximal cross sectional area of this orbit is approximately 3.7 MG, indicating a c/a ratio of about 4. The β frequency is observed in all of the compounds and ranges from 0.86 in $SmAgSb_2$ to 1.64 in $LaAgSb_2$. In each case, the effective masses calculated from the temperature dependence of the amplitudes of the oscillation are approximately 0.17 m_0. The angular dependence of the measured frequencies suggests ellipsoidal topology in $SmAgSb_2$ and $LaAgSb_2$ with a c/a ratio of 4.0. These frequencies and angular dependencies in these compounds are consistent with the calculated dimensions of this energy band centered at the X point. However, in $YAgSb_2$, the frequency of the orbit tends to diverge as the angle increases away from $H \parallel c$, indicating a more cylindrical topology. Further analysis indicates that by shifting the energy of this band downward by 50 meV, the orbit becomes more cylindrical and connected by a thin neck to the next Brillouin zone [Fig. 6.13 (b)].

Conclusion

The $RAgSb_2$ series of compounds is an ideal system for the study of changes in the Fermi surface due to different rare earth ions and magnetic order. The excellent quality of the crystals allows the measurement of de Haas-van Alphen and Shubnikov-de Haas oscillations at relatively low applied fields and exceptionally high temperatures. The persistence of the oscillations in $SmAgSb_2$ up to temperatures as high as 25 K permits the study of changes in the Fermi surface above and below the ordering temperature. Clearly, significant changes in the Fermi surface of $SmAgSb_2$ result from additional periodicity introduced by magnetic order. Overall, the agreement between the calculated Fermi surface and measured quantum oscillations is good. Although the smaller frequencies are not accounted for in the calculated Fermi surface, the magnitude of many of the frequencies and their angular dependence correlate with the ab initio Fermi surface.

Neutron or magnetic X-ray diffraction would be useful to determine the microscopic nature of the magnetic ordering in the materials with magnetic rare earth ions. This knowledge would allow the precise determination of the Fermi surface in the antiferromagnetically ordered states of $SmAgSb_2$. The study of the de Haas-van Alphen or

Shubnikov-de Haas effects at higher fields would help resolve larger sections of Fermi surface, not observed in the relatively low fields currently accessible. Angle resolved photoemission, cyclotron resonance or studies of the anomalous skin effect would be useful to further resolve and verify the Fermi surface of these compounds.

3. CONCLUSIONS

This study of the $RAgSb_2$ series of compounds arose as part of an investigation of rare earth intermetallic compounds containing antimony with the rare earth in a position with tetragonal point symmetry. Materials with the rare earth in a position with tetragonal point symmetry frequently manifest strong anistropies and rich complexity in the magnetic properties, and yet are simple enough to analyze. Antimony containing intermetallic compounds commonly possess low carrier densities and have only recently been the subject of study.

Large single grain crystals were grown of the $RAgSb_2$ (R=Y, La-Nd, Sm, Gd-Tm) series of compounds out of a high temperature solution. This method of crystal growth, commonly known as *flux growth* is a versatile method which takes advantage of the decreasing solubility of the target compound with decreasing temperature. Overall, the results of the crystal growth were impressive with the synthesis of single crystals of $LaAgSb_2$ approaching one gram. However, the sample yield diminishes as the rare earth elements become smaller and heavier. Consequently, no crystals could be grown with R= Yb or Lu. Furthermore, $EuAgSb_2$ could not be synthesized, likely due to the divalency of the Eu ion.

For most of the $RAgSb_2$ compounds, strong magnetic anisotropies are created by the crystal electric field splitting of the Hund’s rule ground state. This splitting confines the local moments to lie in the basal plane (easy plane) for the majority of the members of the series. Exceptions to this include $ErAgSb_2$ and $TmAgSb_2$, which have moments along the c-axis (easy axis) and $CeAgSb_2$, which at intermediate temperatures has an easy plane, but exchange coupling at low temperatures is anisotropic with an easy axis. Additional anisotropy is also observed within the basal plane of $DyAgSb_2$, where the moments are restricted to align along one of the <110> axes.

Most of the $RAgSb_2$ compounds containing magnetic rare earths, antiferromagnetically order at low temperatures. The ordering temperatures of these compounds are approximately proportional to the de Gennes factor, which suggests that the RKKY interaction is the dominant exchange interaction between local moments.

Although metamagnetic transitions were observed in many members of the series, the series of sharp step-like transitions in $DyAgSb_2$ are impressive. In this compound, up to 11 different magnetic states are stable depending on the magnitude and direction of the applied field. The saturated magnetization of these states and the critical fields needed to induce a phase transition vary with the direction of the applied field. Through detailed study of the angular dependence of the magnetization and critical fields, the net distribution of magnetic moments was determined for most of the metamagnetic states. In $DyAgSb_2$, the crystal electric field (CEF) splitting of the Hund's rule ground state creates a strong anisotropy where the local Dy^{3+} magnetic moments are constrained to one of the equivalent <110> directions within the basal plane. The "four position clock model" was introduced to account for this rich metamagnetic system. Within this model, the magnetic moments are constrained to one of four equivalent orientations within the basal plane and interactions are calculated for up third nearest neighbors. The theoretical phase diagram, generated from the coupling constants is in excellent agreement with the experimental phase diagram. Further investigation of this compound using magnetic X-ray or neutron diffraction would be extremely useful to verify the net distributions of moments and determine the wave vectors of each of the ordered states.

The resistivity of the $RAgSb_2$ series of compounds is typical of rare earth intermetallic compounds. At high temperatures the resistivity is linear, and shows no signs of saturation. At low temperatures, the resistivity of the compounds with magnetic rare earths decreases dramatically due to a loss of spin disorder scattering in the magnetically ordered states. The resistivity of the samples is typically about 30 $\mu\Omega$ cm, which is also typical of rare earth intermetallic compounds. The residual resistivity ratio, which provides a measure of sample purity is generally better than 50 in the series but ranges from near 200 in $SmAgSb_2$ to as low as 5 in $ErAgSb_2$.

The temperature dependent resistivity also suggests that $CeAgSb_2$ manifests behavior typical of a dense Kondo lattice with low temperature magnetic order. The interaction between ferromagnetism and Kondo lattice behavior, observed in this compound is the subject of continuing investigation. This study consists of measurements of the resistivity, magnetoresistance, specific heat, and magnetization of the series of diluted compounds ($Ce_xLa_{1-x}AgSb_2$). Detailed understanding of the Kondo effect in these dilute compounds should help determine the Kondo temperature, clarify the interaction between the ferromagnetic order and the Kondo effect, and address the crossover between single impurity and Kondo lattice behavior.

Due to the small residual resistivities and effective masses, the magnetoresistance in the $RAgSb_2$ series of compounds is positive and very large at low temperatures. In $SmAgSb_2$, for example, $\Delta\rho(H)/\rho$ approaches 60 at 55 kOe. At a constant field of 55 kOe, the resistivity decreases with increasing temperature. This effect is particularly dramatic in the compounds that magnetically order and is attributed to Kohler's rule, through the increasing of scattering at higher temperatures or in the paramagnetic state.

The electronic structure of the $RAgSb_2$ series of compounds with R=Y, La, Pr, Nd and Sm was investigated via the analysis of de Haas-van Alphen and Shubnikov-de Haas effects. For R= Y, La, and Sm, these quantum oscillations were clearly visible in the magnetization isotherms at 2 K. In particular, the oscillations in $YAgSb_2$ are exceptionally clear for H || c, since the only two orbits with large amplitudes have frequencies separated by an order of magnetude. For R= Nd and Pr, the oscillations in the magnetization were weaker and obscured by a stronger magnetic background. In $SmAgSb_2$, the oscillations were clearly visible in applied fields below 55 kOe, up to 20 K.

The angular dependence of the observed frequencies was carefully studied for R=Y, La, and Sm. The frequencies of all of the orbits in $YAgSb_2$ and $LaAgSb_2$ were minimal for the magnetic field applied along the c-axis. In most cases, the angular dependence of these orbits were successfully fit to the angular dependence of the cross sectional area of either a cylinder or an ellipsoid. The angular dependence of the oscillations of $SmAgSb_2$ is much more complex, possibly due to a perturbation of the band structure in the magnetically ordered state.

Since $SmAgSb_2$ is antiferromagnetically ordered below T_N = 8.8 K, this compound provides a rare opportunity to study the perturbation of the electronic band structure due to antiferromagnetic ordering. The effects of the ordering are seen in the suppression of the amplitudes in the vicinity of T_N, as well as a shift in the relative phase of the oscillations. An exact determination of the microscopic nature of the antiferromagnetically ordered state is essential for further study of the effects of magnetic ordering on the Fermi surface. This information, acquired via magnetic X-ray or neutron diffraction, would permit the calculation of the band structure in the ordered state which would clarify the effects of magnetic order on the Fermi surface. Measurements of either the de Haas-van Alphen or Shubnikov-de Haas effects in higher fields and lower temperatures should permit the observation of sections of Fermi Surface with larger cross sectional areas and identify the existence of magnetic breakdown. The study of the quantum oscillations under pressure would also help to clarify the electronic structure. Finally, other probes of the Fermi surface, such as angle resolved photoemmision and cyclotron resonance would be useful to help verify the first principles band structure calculations presented here.

Further work should also include the determination of the origin of the transition observed near 210 K in $LaAgSb_2$. Although the behavior of the resistivity near this transition is typical of either a charge or spin density wave, preliminary attempts to verify this have been inconclusive. High resolution X-ray diffraction should provide the necessary precision needed to identify the physics of this transition.

4. REFERENCES

Albering, J. H., and W. Jeitschko, Z. Naturforsch. Teil B, **51** 257 (1996).

Andersen, O. K., O. Jepsen, and D. Glötzel, Canonical Description of Band Structures of Metals, in F. Bassani, F. Fumi, and M. P. Tosi, editors, Highlights of Condensed-Matter Theory, 59-176 (Italian Physical Society, 1985).

Ashcroft, N. W., and N. D. Mermin, *Solid State Physics*, (W. B. Saunders, Philadelphia, 1976).

Bak, P., Rep. Prog. Phys., **45**, 587 (1982).

Boutron, P., Phys. Rev. B, **7,** 3226 (1973).

Brylak, M., M. Möller, W. Jeitschko, J. Solid State Chem. **115**, 305 (1995).

Bud'ko, S. L., P. C. Canfield, C. H. Mielke, A. H. Lacerda, Phys. Rev. B, **57**, 13624 (1998).

Canfield , P. C., P. L. Gammel, D. J. Bishop, Phys. Today, Oct., 40 (1998).

Canfield, P. C. and Z. Fisk, Phil. Mag., **65,** 1117 (1992).

Canfield, P. C., S. L. Bud'ko, B. K. Cho, A. Lacerda, D. Farrell, E. Johnston-Halperin, V. A Kalatsky, V. L. Pokrovsky, Phys. Rev. B, **55**, 970 (1997).

Canfield, P. C., S. L. Bud'ko, J. Alloys Comp., **262-263**, 169 (1997).

Chen, C., Z. Li, and W. Xu, J. Phys. Condens. Matter, **5**, 95, (1993).

Chevalier, B., J. Etourneau, J. E. Greedan, J. M. D. Coey, A Maaroufi, J. Less-Common. Met. **111**. 171 (1985).

Coqblin, B., *The Electronic Structure of Rare-Earth Metals and Alloys: the Magnetic Heavy Rare-Earths*, (Academic Press, London, 1977).

Cordier, G., H. Schafer, P. Woll, Z. Naturforsch. Teil B, **40,** 1097 (1985).

Elliot, R. J. And F. A. Wedgewood, Proc. Phys. Soc. London, **81**, 846 (1963).

Elliot, R. J., *Magnetic Properties of Rare Earth Ions*, Plenum Press, London 1972).

Elwell, D. and H. J. Scheel, *Crystal Growth from High-Temperature Solutions*, (Academic Press, London 1975).

Ferguson, M. J., R. W. Hushagen, A. Mar, J. Alloys Compd. **249**, 191 (1997).

Fierz, Ch., D. Jaccard, J. Sierro, J. Flouquet, J. Appl. Phys. 63 3899 (1988).

Fisher, I. R., A. Thebe, and P. C. Canfield, Ames Tribune, vol 131 no. 29, p. C8, (Aug. 3, 1998).

Fisher, M. E., Phil. Mag. **7,** 1731 (1962).

Flandorfer, H., O. Sologub, C Godart, K. Hiebl, A. Leithe-Jasper, P. Rogl, H. Noël, Solid State Comm., **97**, 561 (1996).

Flouquet, J., P. Haen, F. Lapierre, C. Fierz, A. Amato, D. Jaccard, J. Magn. Magn. Mater, 76&77 285 (1988).

Fuji, H. T. Shigeoka, J. Magn. Magn. Mater. **90 & 91**, 115 (1990).

Houshiar, M., D. T. Adroja, B. D. Rainford, J. Magn. Magn. Mater., **140-144**, 1231, (1995).

Hulliger, F., in *Handbook of Physics and Chemistry of Rare Earths*, edited by K. A. Gschneidner and L. Eyring (North Holland, Amsterdam, Vol. 4. p. 153 1979).

Islam, Z. C. Detlefs, A. I. Goldman, S. L. Bud’ko, P. C. Canfield, J. P. Hill, D. Gibbs, T. Vogt, A. Zheludev, Phys. Rev. B. **58,** 8522 (1998).

Jensen, J, and A. R. Mackintosh, *Rare Earth Magnetism*, (Clarendon, Oxford, 1991).

Kalatsky, V. A., V. L. Pokrovsky, Phys. Rev. B., **57,** 5485 (1998).

Kawakami, N., A. Okiji, J. Phys. Soc. Japn. **55**, 2114 (1986).

Kasaya, M., H. Suzuki, K. Katoh, M. Inoue, and T. Yamaguchi, Japn. J. Appl. Phys, 8, 223 (1993).

Lea, K. R., M. J. M. Leask, and W. P. Wolf, J. Phys. Chem. Solids, 23, 1381 (1962).

Lakshimi, K. V., L. Menon, A. K. Nigam, A. Das, S. K. Malik, Physica B, **223&224**, 289 (1996).

Leithe-Jasper, A., and P. Rogl, J. Alloys Compd., **203,** 133 (1994).

MacKeown, P. K. And Newman, D. J. Computational Techniques in Physics, (Adam Hilger, Bristol, 1987).

Massalski, T. B., H. Okamoto, P. R. Subramanian, and L. Kacprzak, *Binary Alloy Phase Diagrams*, (ASM International, Materials Park, OH, 1992).

Miwa, H. Prog. Theor. Phys. **29**, 477 (1963).

Muro, Y., N. Takeda, M. Ishikawa, J. Alloys Comp., **257** 23, (1997).

Myers, K. D. dHvA (Unpublished).

Myers, K. D., P. C. Canfield, V. A. Kalatsky, V. L. Pokrovsky, (Unpublished).

Noakes, D. R., G. K. Shenoy, Phys. Lett., **91A**, 35 (1982).

Pamplin, Brian R. *Crystal Growth*, (Pergammon Press Ltd,. Oxford, 1975).

Pierre, J., K. Kaczmarska, R. V. Skolozdra, A. Slebarski, J. Magn. Magn. Mater., **140-144**, 891, (1994).

Pinto, H. M. Melamud, M. Kuznietz, H. Shaked, Phys. Rev. B, **31**, 508 (1985).

Pippard, A. B., *Magnetoresistance in Metals*, (Cambridge University Press, Cambridge 1989).

Pippard, A. B. *The Dynamics of Conduction Electrons*, (Gordon and Breach, New York, 1965).

Pokrovskii, V. L. and G.V.Uimin, Zh. Eksp. Teor. Fiz. **82**, 1640-1662 (1982)
(translated to English: Sov.Phys. JETP 55(5) (1982)).

Prather, J. L. U. S. National Bureau of Standards Monograph No. 19 (1961).

Shigeoka, T. H, Fuji, M. Nishi, Y. Uwatoko, T. Takabatake, I. Oguro, K. Motoya, N. Iwata, Y. Ito, J. Phys. Soc. Japan, **61**, 4559 (1992).

Shoenberg, D. *Magnetic Oscillations in Metals*, (Cambridge University Press, Cambridge 1984).

Skolozdra, R. V., Ja. F. Mikhalski, K. Kaczmarska, J. Pierre, J. Alloys Comp., **206**, 141 (1994).

Sologub, O., K. Hiebl, P. Rogl, H. Noël, O. Bodak, J. Alloys Comp., **210,** 153, (1994).

Stevens, K. W. H.. Proc Phys. Soc., **A65**, 209 (1952).

Swanson, H., R. K. Fuyat, G. M. Ugrinic, Natl. Bur. Stand. (U. S.), Circ 539, **3**, 14 (1954).

Taylor, K. N. R.and M. I. Darby, *Physics of Rare Earth Solids,* (Chapman and Hall, London, 1972).

Thornton, M. J., J. G. M. Armitage, G. J. Tomka, P. C. Riedi, R. H. Mitchel, M. Houshiar, D. T. Adroja, B. D. Rainford, and D. Fort, J. Phys.: Condens. Matter **10,** 9485 (1998).

Wallace, W. E., *Rare Earth Intermetallics,* (Academic Press, New York, 1973).

Wang, R. and H. Steinfink, Inorg. Chem., **6**, 1685 (1967).

Wang, Y., Phys. Lett., **35A,** 383 (1971).

Wollesen, P., W. Jeitschko, M. Brylak, L. Dietrich, J. Alloys Comp., **245,** L5 (1996).

Yamada, H., S. Takada, Prog. Theor. Phys., **48,** 1828 (1972).

Yamada, H., S. Takada, Prog. Theor. Phys., **49**, 1401 (1973).

Ziman, J. M. *Electrons and Phonons,* (Oxford University Press, Oxford 1967).

ACKNOWLEDGEMENTS

I would like to express my sincere appreciation to my advisor, Paul Canfield, for his encouragement, guidance, and strong desire to share his knowledge. His enthusiasm for physics is infectious, as well as his sense of humor.

I am thankful to Sergey Bud'ko, who has shared much knowledge and insightful discussions with me. His help with the torque magnetometry, specific heat, and high field studies has added greatly to this work.

I would like to acknowledge Ian R. Fisher for the initial determination of concentrations and temperature profiles for the first attempts to grow the $RAgSb_2$ compounds. His help and critical review of this work were invaluable.

I am grateful to Bruce Harmon and Vladimir Antropov, for their help with the band structure calculations and valuable discussions.

I am indebted to Zahirul Islam and Changyong Song for their help with the X-ray diffraction, Valery Pokrovsky and Valery Kalatsky, for their work with the metamagnetism in $DyAgSb_2$, Holger Kleinke, for the single crystal X-ray diffraction in the $RAgSb_2$ and RCu_xSb_2 series, and Alex Lacerda for the high field work at the National High Field Laboratory, Los Alamos Facility.

I would also like to thank Alex Panchula, Timothy Wiener, and Jason Schissel, for their help cutting metal, arcmelting, filling cryogens, and performing other important tasks.

I am deeply appreciative of the support and encouragement I received from my mother and stepfather. I would especially like to thank my wife, Amy, and son, Benjamin.

These are the two most important people in my life and without their patience and understanding this project would not have been possible.

Ames Laboratory is operated for the U.S. Department of Energy by Iowa State University under Contract No. W-7405-Eng-82. This work was supported by the Director for Energy Research, Office of Basic Energy Sciences.

Work at the NHFML-Los Alamos Facility was performed under the auspices of the National Science Foundation and the Department of Energy.